Continuous separation of microparticles in aqueous medium by means of dielectrophoresis

Dem Fachbereich Produktionstechnik

der

UNIVERSITÄT BREMEN

zur Erlangung des Grades
Doktor-Ingenieur
genehmigte

Dissertation

von

M.sc. Yan Wang

Gutachter: Prof. Dr.-Ing. Jorg Thöming

Prof. Dr.-Ing. Kurosch Rezwan

Tag der mündlichen Prüfung: 11. November 2016

Declaration/Erklärung

I hereby declare that I have produced this thesis without the prohibited assistance of third parties and without making use of aids other than those specified; notions taken over directly or indirectly from other sources have been identified as such. This work has not previously been presented in identical or similar form to any other German or foreign examination board.

Ich erkläre hiermit an Eides statt, dass ich die vorliegende Dissertationsschrift selbständig und ohne unerlaubte Hilfe angefertigt habe, andere als die angegebenen Quellen und Hilfsmittel nicht benutzt und die den benutzten Quellen wörtlich oder inhaltlich entnommenen Stellen als solche kenntlich gemacht habe. Weiterhin versichere ich, dass die Arbeit in gleicher oder ähnlicher Form noch keiner Prüfungsbehörde vorgelegt wurde.

Bremen, 20 06, 2016

The PhD work was conducted from November 21, 2012 to June 20, 2016, under the supervision of Prof. Dr.-Ing. Jorg Thöming at the University of Bremen.

Zusammenfassung

Es gibt einen großen Bedarf an Trennverfahren für in flüssigen Medien suspendierte Mikropartikel, sowohl für den analytischen wie auch für den industriellen Einsatz in der Pharmazeutik, Medizin- und Chemietechnik oder Biologie. Es wurden bereits vielfältige Methoden zur effektiven Abtrennung von Mikropartikeln entwickelt, einige Herausforderungen bleiben allerdings. Dielektrophorese (DEP) ist eine Technik zur Beeinflussung von Bewegungsbahnen von suspendierten Partikeln. Wegen der, im Vergleich zu konventionellen Trennverfahren, bereits bewiesenen hohen Selektivität, Sensitivität und Kontrollierbarkeit und der markierungsfreien Natur hat DEP enormes Potential um schwierige Partikel-Partikel-Separationsprobleme zu lösen. Ein Großteil der DEP-Anwendungen ist bisher allerdings auf Mikrokanäle und Lab-On-A-Chip-Geräte und damit auf Volumenströme im $\mu L \cdot min^{-1}$ Maßstab limitiert. Diese Volumenstromlimitierung beschränkt den Einsatz von DEP-basierten Trennverfahren auf das analytische Level.

Ein vielversprechender Ansatz ist das Hochskalieren von DEP-Systemen um so DEP-Trennverfahren mit hohem Durchsatz auf klinischem oder industriellen Level zu ermöglichen. Hierfür wurde ein neues interdigitales Elektrodendesign (IDE) vorgeschlagen um dem Bedarf nach einem hohen elektrischen Feld beim Hochskalieren von DEP-Systemen gerecht zu werden. Numerische Simulationen mit *OpenFOAM* zeigen, dass sich das dielektrophoretische Kraftfeld, repräsentiert durch den Gradienten des Quadrats des elektrischen Feldes, durch den Austausch von konventionellen Platten-IDE durch zylindrische IDE (cIDE) in Mikrokanalsystemen, verstärkt und homogener über dem Elektrodenarray verteilt. Die daraus resultierenden DEP-Geschwindigkeiten der Partikel waren ebenso höher bei cIDE-Systemen. Simulationen die durch Experimente bestätigt wurden, erlauben weitere Vorhersagen über die Partikelbewegung in vergrößerten cIDE-DEP-Systemen.

Das Verständnis darüber, wie das Zusammenspiel zwischen Kanalgeometrie und Elektrodenkonzept die Partikelgeschwindigkeit beeinflusst, ist kritisch für die Entwicklung eines DEP-Trennverfahrens mit Durchfluss im *präparativen* Maßstab. Das Ziel von maßgeschneidertem Elektrodendesign ist die Kontrolle der Partikeltrajektorien vorwiegend durch Dielektrophorese bei gleichzeitiger Minimierung der elektrothermischen Beeinflussung in Form von durch Temperaturgradienten induzierte Konvektion verursacht durch Stromwärme. Eine Lösung des Stromwärmeproblems in großskaligen DEP-Systemen ist ein Maßschneidern der Verhältnisse aus Elektrodendurchmesser, Elektrodenabstand und Kanalhöhe. Modellrechnungen erlauben eine Vorhersage über die Beeinflussung der

Partikeltrajektorien sowohl durch DEP als auch durch die Widerstandskraft die durch stromwärmeverursachte thermische Konvektion entsteht in Kanälen mit rechteckigem Querschnitt und einem Array aus cIDEs am Boden. Das Modell wurde erfolgreich durch experimentelle Messungen und quantitative Geschwindigkeitsanalysen von polyelektrolytischen Harzpartikeln in demineralisiertem Wasser verifiziert. Dies erlaubt eine qualitative Sensitivitätsanalyse des Einflusses von angelegter Spannung, Partikelgröße und Eigenschaften des Mediums auf kritische Auslegungsparameter. Ausgehend hiervon werden Auslegungsparameter des cIDE-DEP-Systems abgeleitet, sodass der Einfluss der Stromwärme minimiert wird. Die Ergebnisse zeigen, dass, selbst wenn hohe Spannungen angelegt werden, Stromwärmeprobleme in hochskalierten DEP Systemen erfolgreich unterdrückt werden können.

Es gibt bestehenden Bedarf an Methoden zur kontinuierlichen und berührungslosen Abtrennung von Mikropartikeln bei hohem Durchsatz. Um dies zu erreichen wurde ein dielektrophoretischer Feldflussfraktionierer basierend auf dem Mantelstromprinzip mit einer maßgeschneiderten cIDE-Elektrodenanordnung entwickelt. In diesem Separator wurden größenabhängige Partikeltrajektorien beobachtet. Durch das Prinzip der negativen Dielektrophorese wurden bei einer Eingangsspannung von 200 V_{eff} und einer Frequenz von 200 kHz Polystyrolpartikel (45, 25 und 11 µm im Durchmesser) auf verschiedene Schwebehöhen gebracht. Die experimentellen Beobachtungen stimmen sehr gut mit den Ergebnissen der Simulation eines modifizierten Lagrange-Partikeltrackingalgorithmus in Kombination mit der Laplacegleichung und den Navier-Stokes-Gleichungen überein. Durch Ausnutzung der größenabhängigen Schwebehöhe kann die Zielpartikelfraktion bei einer spezifischen Kanallänge abgezogen werden. Die benötigte Kanallänge des vorgeschlagenen Trennsystems erhöht sich dabei mit abnehmender Partikelgröße. Die theoretische Fraktionierungsqualität, quantifiziert durch die Auflösung, erhöht sich stark mit abnehmender Kollektorbreite, abnehmendem Volumenstrom und erhöhtem Spannungseintrag. Die Sensitivität dieser Abhängigkeiten erhöht sich mit abnehmendem Partikeldurchmesser. Durch ein Abwägen zwischen Auslegungs- und Betriebsparametern wurde ein theoretisch möglicher Volumenstrom von bis zu 47 $mL \cdot min^{-1}$ für eine berührungslose Fraktionierung von sensitiven Mikropartikeln mit vernachlässigbarer Scherbeansprachung berechnet.

Für eine weitere Hochskalierung des cIDE-DEP-Trennapparats wurde ein neues Trennsystem mit konzentrisch angeordneten zirkularen Interdigitalelektroden vorgeschlagen. Die Fraktionierung basiert hierbei auf der Größenabhängigkeit der radialen Verschiebung in der Separationskammer, in welcher eine bewegliche Probenröhre das Abziehen der Partikel bei

verschiedenen Höhen ermöglicht. Die Machbarkeit wurde durch numerisch vorhergesagte Mikropartikeltrajektorien im Separator demonstriert. Die Simulationen zeigen eine bemerkenswerte Zunahme des möglichen Durchflusses mit dem konzentrischen cIDE-Separator im Vergleich zum herkömmlichen cIDE-Separator unter gleichen Bedingungen. Aus einer Beurteilung des Einflusses der Betriebsparameter auf die Partikelverschiebung kann abgeleitet werden, dass eine Fraktionierung selbst bei Volumenströmen von hunderten $mL \cdot min^{-1}$ möglich ist. Diese theoretischen Ergebnisse legen den Grundstein für die kontinuierliche DEP-basierte Mikropartikelabtrennung im industriellen Maßstab.

Abstract

There is a widespread need to separate microparticles suspended in liquid media, for both analytical and industrial applications in pharmaceutical, medical, chemical and biological fields. A variety of techniques aimed at effective microparticle separation have been developed over the decades, but challenges still remain. Dielectrophoresis (DEP), a technique for manipulating the motion trajectories of suspended particles, has enormous potential for solving difficult particle-particle separation problems, owing to its demonstrated high sensitivity, selectivity and controllability as well as label-free nature, compared to conventional separation means. Nevertheless, the great majority of DEP applications have been limited so far to microchannels and lab-on-a-chip devices, with throughput typically in the $\mu L \cdot min^{-1}$ range. This limitation of throughput acts as a barrier restricting DEP-based separation to the purely analytical level.

A promising, alternative solution to this problem is anticipated by upscaling DEP systems to enable high-throughput DEP separation on a clinical or industrial scale. To achieve this, a novel interdigitated electrode (IDE) design is proposed to meet the need for a high electric field when upscaling a DEP system. Numerical simulation using *OpenFOAM* demonstrated that, when replacing conventional plate IDE by cylindrical IDE (cIDE) in microchannel systems, the dielectrophoretic force field, represented by the gradient of the squared electric field, becomes stronger and more homogeneously distributed along the electrode array. The resulting particle DEP velocities were also higher for the cIDE. Simulations confirmed by experiments allow further predictions of particle motion in enlarged cIDE-DEP systems.

Understanding how the interplay of channel geometry and electrode concept affects induced particle velocity is crucial when designing DEP separators having sufficiently high throughput to reach preparative scale. The objective of tailored design is to control particle motion trajectories predominantly by DEP while avoiding electrothermal interference in the form of fluid convection induced by a temperature gradient in the liquid phase due to Joule heating. One solution to this Joule heating problem in large-scale DEP systems is to tailor the ratios of electrode diameter, electrode distance and channel height. Based on model calculations, the influence on particle trajectories of both DEP force and drag force due to thermal convection was predicted for a case study involving a channel with rectangular cross section and an array of cIDEs at the bottom. The models were successfully verified by experimentally measuring and quantitatively analysing velocities of polyelectrolytic resin microparticles located at the subsurface of demineralized water. This allowed a qualitative sensitivity analysis of the impact

of voltage input, particle size and medium properties on critical design parameters. From this, design criteria were deduced for the cIDE-DEP system that allow the influence of Joule heating to be minimised. The findings demonstrate that, even when high voltages are applied, Joule heating problems can be effectively suppressed in DEP system scale-up.

There is still a need for continuous, contact-free fractionation of microparticles at high throughput. To achieve this, a sheath-flow-assisted dielectrophoretic continuous field-flow separator with a tailored arrangement of cIDE was developed, and size-dependent trajectories of dispersed particles were observed. Using a voltage input of 200 V_{eff} at a frequency of 200 kHz, polystyrene particles (45, 25, and 11 µm in diameter) were levitated to different heights due to a negative DEP force. Experimental observations agree well with simulated particle trajectories that were obtained from by a modified Lagrangian particle tracking model in combination with Laplace's and Navier-Stokes equations. By exploiting the size-dependent levitation height difference, the desired particle size fraction can be collected at a specific channel length. The required channel length of the proposed cIDE separator increases with decreasing particle size to be separated. The quality of theoretical fractionation, which is quantified by resolution, improves strongly with reduced collector width, reduced volume flow rate and increased voltage input. The sensitivity of these dependencies increases with decreasing particle size. A theoretically calculated system throughput of up to 47 $mL \cdot min^{-1}$ was found to be possible by trading off design and operation parameters, enabling contact-free fractionation of sensitive microparticles with negligible shear stress.

For further upscaling of the cIDE-DEP separation system, a new separation device with concentrically arranged cIDE configuration was proposed. Fractionation is based on size-dependent differences of particles' dielectrophoretic radial displacements in the separation chamber, in which a movable sampling tube is installed along the central line of the separator to collect desired particle sizes at certain heights. Proof-of-concept is demonstrated by numerically predicting microparticle motion trajectories within the separator. Simulations show that a remarkable increment of suspension throughput can be achieved by the concentric cIDE separator compared to the cIDE separator under the same circumstances. From an evaluation of the impact of operating parameters on particle displacement, it can be deduced that continuous fractionation is possible even at system throughputs in the of hundreds of $mL \cdot min^{-1}$ range by using the concentric cIDE separator. These theoretical findings lay the foundation for continuous DEP-based microparticle separation on an industrial scale.

Acknowledgements

First and foremost, I would like to express my sincere gratitude to my supervisor Prof. Dr. Jorg Thöming for giving me the opportunity to study in University of Bremen; for the continuous support of my PhD research and living in Bremen; for his patience, motivation, and immense knowledge. His guidance helped me in all the time of research and writing of this thesis.

I am heartily thankful to Dr. Michael Baune and Dr. Fei Du for providing enthusiastic guidance and supervision. Their insightful instruction and invaluable assistance always pointing me in the right direction. Without their precious support it would not be possible to finish my PhD work.

I would like to thank Georg R. Pesch for his scientific advice and knowledge. He has provided many insightful discussions and suggestions about the research.

For nice advice and help, I am grateful to all my colleagues (in alphabetical order): Andrea Böschen, Steve Bemowsky, Detlef Bobenhausen, Ulrike Bottin-Weber, Sonja Faetsch, Karoline Gajda, Dietmar Grotheer, Dr. Jan Köser, Lars Kiewidt, Malte Lorenz, Dr. Marta Markiewicz, Antje Mathews, Dr. Jennifer Neumann, Anne-katrin Nienstedt, Alica Rother, Dr. Stefan Stolte, Jürgen Ulpts, Dr. Thomas Veltzke, Wiebke Veltzke and Yaqi Zhang.

This thesis would not have been possible without the infrastructure of the University of Bremen and the Center for Environmental Research and Sustainable Technology (UFT). I gratefully acknowledge the China Scholarship Committee (CSC) for financially supporting (CSC [2011] 3005) my stay in Germany. My work was also supported by German Research Foundation (DFG) with project number TH 893/9-1.

I would like to thank my parents and parents in law for all their love and encouragement. A special thanks to my beloved wife Jing who spent sleepless nights with me and supported me spiritually throughout writing this thesis and my life in general.

Lastly, many thanks to all of those who supported me in any respect during the completion of the PhD work.

Contents

List of Figures

List of Tables

List of Publications

Scientific articles

1. Y. Wang, F. Du, G.R. Pesch, J Köser, M. Baune, J. Thöming (2016) Microparticle trajectories in a high-throughput channel for contact-free fractionation by dielectrophoresis, *Chem. Eng. Sci.* 153: 34-44.

2. Y. Wang, F. Du, M. Baune, J. Thöming (2015) Predicting and eliminating Joule heating constraints in large dielectrophoretic IDE separators, *Chem. Eng. Sci.* 137: 235-242.

3. Y. Wang, F. Du, M. Baune, J. Thöming (2014) Dielectrophoresis in aqueous suspension: impact of electrode configuration, *Microfluid Nanofluidics* 17: 499-507.

4. F. Du, P. Ciaciuch, S. Bohlen, Y. Wang, M. Baune, J. Thöming (2013) Intensification of cross-flow membrane filtration using dielectrophoresis with a novel electrode configuration. *Journal of Membrane Science* 448: 256-261.

Conferences

1. Y. Wang, G. Pesch, F. Du, M. Baune, J. Thöming. Study of structure parameter for optimized design of electrode configuration. *Dielectrophoresis 2014*, *14-16 July 2014, London, UK* (oral presentation).

Glossary

symbol	Description/Value	Unit
	Roman	
A	Cross sectional area	m^2
C_D	Drag coefficient	-
C_E	Capacitance of the electrode with insulation film	F
C_m	Capacitance of the medium	F
D	Diffusion coefficient of the particle	$m^2 \cdot s^{-1}$
D_e	Diffusion coefficient of excess free charge in diffuse layer	$m^2 \cdot s^{-1}$
$\boldsymbol{E}$	Electrode field intensity	$V \cdot m^{-1}$
$\boldsymbol{E}^*$	Complex conjugate of the electric field	$V \cdot m^{-1}$
$(\boldsymbol{E} \cdot \nabla)\boldsymbol{E}$	Electric field factor	$V^2 \cdot m^{-3}$
$\nabla \lvert \boldsymbol{E} \rvert^2$	Gradient of square of the electric field	$V^2 \cdot m^{-3}$
F	Faraday constant, F = 96485.33	$C \cdot mol^{-1}$
$\boldsymbol{F}_{DEP}$	Dielectrophoretic force	N
$\boldsymbol{F}_{drag}$	Hydrodynamic drag force	N
$\boldsymbol{F}_{EP}$	Electrophoretic force	N
$\boldsymbol{F}_g$	Gravitational force	N
H	Height of the cIDE separation channel	m
H^+	Hydrogen ion	-
H_c	Height of the concentric cIDE separation channel	m
$\boldsymbol{J}$	Electric current density	$A \cdot m^{-2}$
$\tilde{K}$	Clausius-Mossotti factor	-
K_{Diff}	Diffuse layer conductance	S
$K_{Diff,eo}$	Electroosmosis induced diffuse layer conductance	S
$K_{Diff,m}$	Charge movement induced diffuse layer conductance	S
K_S	Surface conductance of the particle	S
K_{Stern}	Stern layer conductance	S
L_{opt}	optimal length of the separation channel	m
M	Dimensionless factor	-
P	Electric power	W
Pe	Pelect number	-

Q	Volume flow rate of the system	$m^3 \cdot s^{-1}$
Q_{tot}	Total charge on the particle	C
R	Resolution of fractionation	-
R_{cyto}	Cytoplasmic resistance	Ω
$Re[\tilde{K}]$	Real part of the Clausius-Mossotti factor	-
Re_p	Reynolds number of particle	-
R_g	Gas constant, $R_g = 8.314$	$J \cdot mol^{-1} \cdot K^{-1}$
R_i	Inner radius of the concentric cIDE cross section channel	m
R_m	Electrical resistance of the medium	Ω
R_s	Electrical resistance of the system	Ω
Stk	Stokes number	-
T	Absolute Temperature	K
ΔT	Temperature difference	K
U	Applied voltage	V
U_0	Voltage across the power	V
U_m	Voltage across the medium	V_{eff}
U_{rms}	Root mean square of the applied voltage	V_{eff}
V	Volume of the medium	m^3
V_p	Volume of the particle	m^3
W	Width of the single collector channel	m
Z	Electrical impedance	Ω
a	Radius of the spherical particle	m
c	Electrolyte concentration	$mol \cdot m^{-3}$
c_m	Specific capacitance of the cell membrane	$F \cdot m^{-2}$
c_p	Specific heat capacity of the fluid	$J \cdot kg^{-1} \cdot K^{-1}$
d	Electrode diameter	m
d_p^*	Specific particle diameter	m
d_{p1}^*	Smallest particle size entering the collector	m
d_{p2}^*	Biggest particle size entering the collector	m
Δd_p	Particles size difference	m
d_r	radial distance from center of co-planar electrodes	m
f	Electric field frequency	Hz
$\boldsymbol{f}_B$	Buoyancy body force	$N \cdot m^{-3}$
$\boldsymbol{f}_E$	Electrothermal body force	$N \cdot m^{-3}$

f_{MW}	Maxwell-Wagner relaxation frequency	Hz
f_s	Stokes' drag coefficient	$N \cdot s \cdot m^{-1}$
$\boldsymbol{f}_{tot}$	Total applied body force	$N \cdot m^{-3}$
$\boldsymbol{g}$	Gravitational acceleration, $\boldsymbol{g}$ = 9.81	$m \cdot s^{-2}$
g_m	Specific conductance of the cell membrane	$\Omega^{-1} \cdot m^{-2}$
h	Height of the cIDE-DEP system/Position in height direction	m
h_c	Critical height of IDE-DEP channel	m
j	Imaginary unit	$\sqrt{-1}$
k	Thermal conductivity of the fluid	$W \cdot m^{-1} \cdot K^{-1}$
k_b	Boltzmann's constant, $k_b = 1.38 \times 10^{-23}$	$J \cdot K^{-1}$
L	Space between electrodes	m
L_c	Character length of the system	m
m	Contribution of ion flux to the diffuse layer conductance	-
$\boldsymbol{p}$	Effective dipole moment	C·m
p	Pressure	Pa
$\boldsymbol{p}_{av}$	Average dipole moment	C·m
q	Charge on the electron	C
q_{gen}	Heat generation in the system	$W \cdot m^{-3}$
r	Position in radial direction	m
Δr	Radial displacement of particle	m
$\Delta \boldsymbol{s}_x$	Particle motion distance in x direction	m
t	Time of particle distribution following Gaussian profile	s
Δt	Particle motion time	s
$\boldsymbol{u}_m$	Velocity of the particle	$m \cdot s^{-1}$
$u_{\max}$	Maximum flow velocity	$m \cdot s^{-1}$
$\boldsymbol{u}_p$	Velocity of the medium	$m \cdot s^{-1}$
$\boldsymbol{v}_{DEP}$	Dielectrophoretic velocity	$m \cdot s^{-1}$
$\boldsymbol{v}_{EP}$	Electrophoretic velocity	$m \cdot s^{-1}$
v_{ETE}	Electrothermal velocity	$m \cdot s^{-1}$
v_x	Particle velocity in x direction	$m \cdot s^{-1}$
x	Position in horizontal direction	m
Δx	Root mean square of the displacement in one dimension	m
$\boldsymbol{z}$	Position in axial direction	m
z_i	Valence of the counterion	-

Greek

α	Polarizability	$C \cdot m^2 \cdot V^{-1}$
$\tilde{\alpha}$	Complex effective polarizability	$C \cdot m^2 \cdot V^{-1}$
α_v	Volumetric thermal expansion coefficient	K^{-1}
β	Refer to the polar coordinates	degree
$\tilde{\boldsymbol{\varepsilon}}$	Complex relative permittivity	-
ε_0	The permittivity of free space, $\varepsilon_0 = 8.854 \times 10^{-12}$	$F \cdot m^{-1}$
ε_m	Relative permittivity of the medium	-
ε_p	Relative permittivity of the particle	-
ϕ	Electric potential	V
ϕ_0	surface potential	V
ϕ_d	Stern layer potential	V
κ	Debye length	m
λ_0	Wavelength of the laser	m
μ_E	Electrophoretic mobility	$m^2 \cdot V^{-1} \cdot s^{-1}$
μ_m	Dynamic viscosity of the medium	Pa·s
μ_p	Dynamic viscosity of the particle	Pa·s
μ_{Stern}	Ion mobility in the Stern layer	$m^2 \cdot V^{-1} \cdot s^{-1}$
θ	angle measured from one planar electrode	rad
ρ	Volume charge density	$C \cdot m^{-3}$
ρ_m	Mass density of the medium	$kg \cdot m^{-3}$
ρ_p	Mass density of the particle	$kg \cdot m^{-3}$
$\rho_{q,Stern}$	Surface charge density in the Stern layer	$C \cdot m^{-2}$
σ	Electrical conductivity	$S \cdot m^{-1}$
σ_m	Electrical conductivity of the medium	$S \cdot m^{-1}$
σ_p	Electrical conductivity of the particle	$S \cdot m^{-1}$
$\sigma_{p,bulk}$	Bulk conductivity of the particle	$S \cdot m^{-1}$
$\sigma_{p,surface}$	Surface conductivity of the particle	$S \cdot m^{-1}$
τ	Time constant	s
τ_{MW}	Maxwell-Wagner relaxation time	s
τ_m	Characteristic time of the medium	s
τ_p	Particle relaxation time	s
ω	Angular frequency	Hz
ζ	Zeta potential	V

Abbreviations

AC	Alternative current
AR	Aspect ratio
CCD	Charge-coupled device
CFD	Computational fluid dynamics
cIDE	Cylindrical interdigitated electrode
DC	Direct current
DEP	Dielectrophoresis
EP	Electrophoresis
ETE	Electrothermal
FFF	Field flow fractionation
IDE	Interdigitated electrode
MW	Maxwell-Wagner
NTC	Negative Temperature Coefficient
n-DEP	Negative dielectrophoresis
PDE	partial differential equation
PFF	Pinched flow fractionation
PS	Polystyrene
p-DEP	Positive dielectrophoresis
Re	Real part
RIP	Region of particle initial position
rms	Root mean square
s.d.	Standard deviation

1 Introduction

1.1 Separation technology - state of the art

Nowadays, with the growth of nanotechnology, a variety of approaches to the separation of nano-sized particles have become well established. Nevertheless, the number of methods developed for separating microparticles is comparatively small, despite their great importance for solving numerous practical problems (Katasonova and Fedotov, 2009). Typically, microparticles are objects ranging from 0.1 to hundreds of micrometers in size, including cells and biological particles, metals and metallic oxides, colloids and polymer beads, ceramic microspheres, etc. In some circumstances, suspended microparticles are liable to be formed as mixtures. Effective separation of these mixed microparticles in liquid medium is needed on a broad scale for chemical and biological production systems, as well as diagnostic and clinical applications in which separated and purified particles are studied (Çetin and Li, 2011; Jin et al., 2014; Lenshof and Laurell, 2010; Yamada et al., 2004); the generation of several fractions is even required in many cases (Fedotov et al., 2011; Messaud et al., 2009). In fact, microparticle separation is a necessary preparation step in most biological assays and is common in chemical processing (Kersaudy-Kerhoas et al., 2008). In many agrochemical, cosmetics and pharmaceutical companies, the solid microparticle products of chemical reactions have to be separated for post-treatment.

Techniques aimed at achieving accurate and sensitive microparticle separation have been developed over the years, yet challenges remain. Conventional macro-scale separation techniques, such as sedimentation, mechanical filtration, centrifugation, membrane filtration, etc., have been widely used in industrial applications for preliminary and coarse separation, as they allow products to be processed on a large scale (Carlo et al., 2008). However, the systems for these separation techniques are bulky, expensive and labor-intensive (Zhang et al., 2014), and may risk damaging sensitive biological samples due to the substantial mechanical stresses that are involved (Bhagat et al., 2011). Likewise, with recent advances in microfabrication technology (Auroux et al., 2002; Reyes et al., 2002), a variety of micro-scale separation techniques, such as field-flow fractionation, chromatography, capillary electrophoresis, etc., are now well established, especially in analytical separation. Compared to macro-scale separation techniques, micro-scale techniques in a microfluidic environment can bring several benefits, including potential portability and ease of use, greater accuracy of particle control without the interference of turbulence due to creeping flow at low Reynolds

numbers (typically Re < 1), and larger surface-to-volume ratio, which allows greater separation efficiency as well as more rapid heat dissipation as long as the additional external field is applied (Beebe et al., 2002). While a major disadvantage of these micro-scale separation techniques, unfortunately, is that scaling down separation systems limits the throughputs that can be achieved with these techniques. Most micro-scale separation techniques also involve complex and time-consuming separation procedures and batch operation (Pamme, 2007) and may dominate total production costs if large dispersion volumes are to be processed. Some microsystem separation techniques are designed as miniaturized versions of conventional macro-scale approaches, but with the additional advantage of favorable scale effects; whereas others are only possible on the micro-scale with a number of limitations.

A critical review of all the microparticle separation techniques is certainly beyond the scope of this work; nevertheless, some of the representative methods are of fundamental importance in the field of separation science and will thus be discussed in more detail.

Centrifugation is the most common macro-scale technique used for separating particles from liquid media or for separating mixtures of particles of different size/density into separate fractions of the supernatant. Centrifugation uses centrifugal force to promote accelerated settling of particles in a solid-liquid mixture and employs centrifuges which achieve particle separation by rapid rotation. While undergoing centrifugation, samples are often exposed to strong acceleration over a long period, which may affect their structures and even cause damage to sensitive products (Zhang et al., 2014). Centrifugation is also labor-intensive and requires multi-step sample preparation, which may introduce undesired artifacts or the loss of target samples (Bhagat et al., 2011; Xie et al., 2010).

Membrane filtration, including microfiltration and ultrafiltration, are pressure-driven membrane transport processes used to separate microorganisms, macromolecules and solid particles (Fedotov et al., 2011). In membrane filtration processes, samples are pumped through a series of membranes with gradually decreasing pore size to achieve separation or even fractionation. Compared to micro-scale separation methods, membrane filtration has the potential to process large sample volumes simultaneously. However, this technique often suffers from the problem of membrane fouling. Fouling is the formation of a solid or gel layer on the filter surface, which hampers further fractionation (Guo et al., 2012). If the fouling layer is not removed, its permeability decreases over time, and this occurs even more rapidly at higher particle concentrations (Seminario et al., 2002). Despite many significant improvements that have already been developed, crucial questions still remain unanswered (Drews, 2010). Furthermore, the membrane filtration approach can seriously underestimate a particular

fraction (Gimbert et al., 2005) in analytical separation, and particles of similar size, although differing in nature, may fall into the same fraction when membrane filtration is applied.

Field-flow fractionation, a family of analytical techniques developed specifically for separating and characterizing colloids, macromolecules and microparticles, was first introduced by Giddings (1966) as an elution-based method similar to chromatography. Field-flow fractionation exploits the combined effect of an external field perpendicular to the direction of carrier liquid flow and the velocity gradient of a hydrodynamic flow profile to achieve particle separation (Giddings, 1993). A variety of external fields have been implemented in field-flow fractionation, including gravitational, centrifugal, thermal gradient, electric, magnetic, acoustic, optical, etc. Particles of many different types and sizes can be separated by field-flow fractionation with minimum interaction between the sample mixtures and the channel walls (Katasonova and Fedotov, 2009). However, field-flow fractionation requires a ribbon-like channel having rigorously defined dimensions in order to create a parabolic flow profile, allowing extremely short relaxation time for particles to reach their equilibrium positions above the electrodes and only adequate retention time differences between particles for effective elution (Messaud et al., 2009). In addition, the lack of an effective external force mechanism for controlling the particles' equilibrium position throughout the flow profile results in field-flow fractionation having limited sensitivity and selectivity (Huang et al., 1997).

Capillary electrophoresis, also known as capillary zone electrophoresis, is a well-established analytical technique that is widely applied to separate and characterize solid microparticles, colloids, macroions, and especially biological cells according to their nature and size (Glynn et al., 1998; Radko and Chrambach, 1999; Radko and Chrambach, 2002). In capillary electrophoresis, the samples are driven through the capillary by electroosmotic flow, separated according to their electrophoretic mobility, which depends on surface charge and size, and detected at the end of the capillary. Capillary electrophoresis is characterized by its high efficiency, rapidity and low consumption of samples and reagents (Han et al., 2015), thus conforming to the requirements of green chemistry. Nevertheless, since capillary electrophoresis depends on differences in particles' electrophoretic mobility, it is therefore limited to charged particles. If both positively and negatively charged particles are to migrate toward their countercharged electrodes, the required electric field must be produced by a direct current (*DC*) potential difference. Using a capillary as separation channel also confines the system to a low throughput of 1 $\mu L \cdot min^{-1}$ at most, which makes it suitable solely for sample analysis and detection (Katasonova and Fedotov, 2009).

In recent years, more and more attention has been concentrated on developing continuous flow separation techniques in microfluidic systems, due to the limitations of batch processes which require single and precise injection with extremely small amounts of samples in a separation chamber, i.e., in which the permissible weight of the test sample is less than 1mg in field-flow fractionation and the volume of the test sample is lower than 1nL in capillary electrophoresis, respectively (Katasonova and Fedotov, 2009), and due to their relatively long separation times. Continuous flow separation methods are characterized by continuous sample introduction, real-time monitoring, minimum residence time under harmful conditions for separated particles, as well as continuous collection of the desired product, which makes them ideal in combination with upstream and downstream applications (Pamme, 2007). Representative techniques, including pinched flow fractionation (Khashei et al., 2015; Takagi et al., 2005), hydrophoresis (Choi and Park, 2007), split-flow thin fractionation (Ratier and Hoyos, 2010), magnetophoresis (Pamme and Wilhelm, 2006) and inertial microfluidics (Bhagat et al., 2011; Kuntaegowdanahalli et al., 2009), have been applied for continuous fractionation of microparticles in microfluidic systems. Despite having definite advantages, these separation techniques also have some potential drawbacks which may limit the efficiency of separation. Yamada et al. (2004) proposed a pinched flow fractionation (PFF) method, which made use of both the laminar flow profile and geometrical expansion to achieve continuous fractionation of microparticles based on size. Separation of 15 and 35 μm polymer microbeads using this method was shown to be feasible. However, separation performance was considered low, since it is impossible to adjust the channel width in the pinched region according to the particle size fraction, so separation according to particle size cannot be precise enough in a PFF device (HeonáLee et al., 2011). Particle clogging problems should also be taken into account at the extremely narrow pinched region. Choi and Park (2007) reported a microfluidic separation method for continuously separating and sorting microparticles by using hydrophoresis. Hydrophoretic separation of 9 μm and 12 μm polystyrene microbeads was demonstrated by exploiting slanted obstacles in a microchannel to generate a lateral pressure gradient so that particles can be deflected to different positions, thus achieving separation. The separation device is relatively easy to make, and the performance of separation is independent of the applied volume flow rate in a specific range. Nevertheless, the fact that separation efficiency is determined by the geometry of obstacles imposes limitations on the range of particle sizes to be separated. Ratier and Hoyos (2010) used a split-flow lateral-transport thin fractionation channel in combination with acoustic force and gravitational field in order to separate 5 μm and 10 μm latex particles. Experimental

separation was achieved with throughput highly improved by one order of magnitude compared to conventional split fractionation. However, only binary separation is possible in each separation step when the split technique is used, while multistep procedures are needed to separate a number of different fractions. Most recently, Zhang et al. (2014) have reported an inertia-based particle separation approach that employs a serpentine channel for continuous separation of particles based on size (Stokes number), at flow rates up to 0.7 $mL \cdot min^{-1}$. However, it was not possible to determine the specific particle size threshold, as the forces that act on particles could not be adjusted.

1.2 Dielectrophoretic particle separation

Although great progress has been made in separation technologies, a versatile technique which meets the need for continuous, label-free and contact-free separation of microparticles with high efficiency and high resolution as well as low energy consumption has still to be found. Among various separation approaches, one promising technique exploits the dielectrophoretic (DEP) force exerted on different particle populations. The resultant differences in particles' dielectrophoretic motion behavior manifest themselves as variations in DEP force magnitude and/or direction, thus producing separation. This is referred to as dielectrophoretic particle separation. The basic theories of dielectrophoresis and dielectrophoretic force are discussed in greater detail in Chapter 2. Indeed, DEP force is a very versatile force that can be used to manipulate, discriminate and separate between different particle types in fluid suspensions. Dielectrophoretic separation enables proper separation of different particle populations which are characterized by differences in their size (Chuang et al., 2014; Cui et al., 2009; Han et al., 2009; Kim et al., 2008; Kralj et al., 2006; Park and Jung, 2009; Pommer et al., 2008) and/or electric properties (Doh and Cho, 2005; Huang et al., 1997; Li et al., 2007; Wang et al., 1998), since these properties play a dominant role in a particle's dielectrophoretic behavior. Given its demonstrated simplicity, high sensitivity and selectivity, as well as label-free nature (Gossett et al., 2010; Pethig, 2010; Voldman, 2006), dielectrophoresis is considered to be a very effective approach for microparticle separation (Hughes, 2002).

The first attempt to achieve dielectrophoretic particle separation was made by Herbert A. Pohl and his co-workers in the 1960s. Pohl and Plymale (1960) designed an isomotive cell geometry to produce a local, non-uniform electric field for separating several groups of mineral particle mixtures. Mixtures of zircon and rutile, which cannot be separated by conventional density or magnetic methods, proved to have rapid separability under dielectrophoretic conditions. In order to better understand particles' dielectrophoretic behavior, a simplified

theory for the electrical forces exerted on the particles, in combination with gravitational and non-uniform electric fields, was also given. In addition to mineral microparticles, dielectrophoresis can also be used to discriminate noninvasively between cells based on their dielectric makeup, i.e., to achieve separation of cells on the basis of physical phenomena occurring inside the cell. Crane and Pohl (1968) demonstrated dielectrophoretic separability between living and dead yeast cells. The results showed that living cells can be rapidly distinguished from dead ones, and collected separately, using dielectrophhoresis. A comparative study was conducted for a range of parameters to improve separation yield. The results of dielectrophoretic cell separation were later verified by Mason and Townsley (1971), who also achieved dielectrophoretic separation of two nutritional types of yeast cells which are characterized by their different sizes.

In recent years, new ideas have been developed for demonstrating the use of dielectrophoresis or dielectrophoretic methods to achieve greater versatility in microparticle separation, i.e., either by binary separation of particles into two separate groups, or for fractionation of many populations, even in a continuous manner. One of the breakthroughs has been the coupling of hydrodynamic forces into dielectrophoresis to produce continuous particle separation. In this case, the interdigitated electrode array is often used to produce a DEP force that levitates particles to different heights or deflects them to different lateral positions depending on their size or dielectric properties. The combination of hydrodynamic flow with a well-defined parabolic flow profile can be used to drive particles at different velocities. Particles experience both effects, thus allowing better discrimination between them. Kralj et al. (2006) developed a continuous dielectrophoretic flow separation channel with embedded slanted, planar interdigitated electrodes to separate polystyrene (PS) microparticle mixtures. Size-based differences in the dielectrophoretic deflection of microparticle enable the 4 μm and 6 μm PS particles to be continuously separated in the proposed microfluidic device. Yang et al. (2000) reported the use of dielectrophoresis-based field-flow fractionation (DEP-FFF) to fractionate mixtures of the major human leukocyte subpopulations (T- and B-lymphocytes, monocytes, and granulocytes). This technique exploits an array of interdigitated electrodes to produce local inhomogenous electric fields, and the resultant negative DEP forces levitate leukocytes above the electrodes based on differences in their dielectric properties. The high purity and good performance thus achieved allow fractionation to be tailored to many clinical and research applications. Han et al. (2009) introduced a lateral dielectrophoretic flow separator that exploits the size-based differences in lateral displacement of particles passing over a planar interdigitated electrode array to enable continuous

fractionation. The admixture of polystyrene microbeads with 3 μm, 5 μm and 10 μm in diameter were continuously and simultaneously separated out with nearly perfect separation efficiency. Chuang et al. (2014) presented a compact and tunable dielectrophoretic flow microchip to enable size-based microparticle fractionation using negative dielectrophoresis. Polystyrene particles 1 μm, 2.5 μm and 4.8 μm in size were successfully fractionated into three distinct streams based on dielectrophoretic deflection after passing through the planar interdigitated electrode array and collected in different outlet channels.

All the above efforts make dielectrophoretic separation a promising alternative to conventional microparticle separation techniques.

1.3 Problems

Dielectrophoresis was first introduced in the 1950s as a term for describing the motion of particles in non-uniform electric fields (Pohl, 1951; Pohl, 1958). Over several decades, dielectrophoresis has attracted a variety of research interest with regard to sorting (Srivastava et al., 2011; Vahey and Voldman, 2008), trapping (Müller et al., 1999), concentrating (Chen and Du, 2010), manipulating (Das et al., 2014) and especially separating (Markx and Pethig, 1995) cells and microparticles, due to its proven versatility, flexibility and controllability. Nevertheless, reliable application of DEP has been concentrated until now on lab-on-a-chip scale setups, with throughputs typically being in the $\mu L \cdot min^{-1}$ range (Bisceglia et al., 2015; Cheng et al., 2009; Li et al., 2010; Ling et al., 2012; Tsukahara et al., 2001). DEP separation of particles or cells with relatively high throughput, enabling separation on a clinical or industrial scale, has rarely been reported (Sano et al., 2012).

Çetin and Li (2011) pointed out that research on throughput improvement is needed to make DEP-based systems competitive with conventional separators. However, the term 'high-throughput' has not yet been clearly defined for the case of continuous separation of particles from suspensions or dispersions using DEP (Wang et al., 2015). Čemažar et al. (2016) designed a high-throughput contactless DEP device that uses cell-size pillars to isolate and enrich rare cell samples. The proposed device has the capability of separating cells with a high flow rate of 37 $\mu L \cdot min^{-1}$ and throughput of a few million cells per hour while maintaining high cell viability. Gadish and Voldman (2006) proposed a dielectrophoretic microfluidic device for concentrating particles with a high throughput of up to 100 $\mu L \cdot min^{-1}$, which serves as an interface between preparative sample collectors and microscale detectors. Moon et al. (2011) reported a novel method for continuous separation of circulating tumor cells from blood cells by combining multi-orifice flow fractionation and DEP. They achieved high separation

efficiency at a flow rate of 162 μL·min^{-1}, indicating the possibility of high-throughput application for clinical cell sorting. Markx et al. (1994) used AC DEP to separate viable and non-viable yeast cells with a volumetric flow rate of 500 μL·min^{-1}. Wang et al. (1998) introduced dielectrophoretic field-flow fractionation for separating two types of polystyrene beads with different surface functionalization. The degree of separation, which is characterized by the ratio of the elution peak times of two populations, was not compromised even at the high flow rate of 1000 μL·min^{-1}. Pesch et al. (2014) presented a novel method of recovering submicron particles by using high-throughput dielectrophoretically switchable filtration. Good separation and recovery efficiencies of nanocapsules were achieved in semi-continuous operation at flow rates of 1 mL·min^{-1}. In order to increase throughput, Kang et al. (2009) identified the trade-off between high throughput and high separation efficiency in continuous operation and proposed a microfluidic device using embedded electrodes and an insulating obstacle for continuous dielectrophoretic separation of 5 μm and 10 μm particles. Sano et al. (2012) proposed a dielectrophoretic particle separator using three-dimensional mesh-stacked electrodes to separate tungsten carbide particles from a mixture with diatomite. The way to raise throughput per unit is to increase the width of the channel. This is obviously the lower-cost option compared to massively parallelized numbering-up of single units, but may be associated with manufacturing challenges. Some other researchers have also made progress on increasing the throughput/flow rate of DEP-based microfluidic devices in various ways (Ahn et al., 2006; Čemažar et al., 2016; Cheng et al., 2009; Fatoyinbo et al., 2005; Park and Madou, 2005; Yan et al., 2014), but the low throughput of dielectophoresis-based particle separation remains an ongoing problem.

Although dielectrophoresis offers some advantages that make it a suitable separation technology in lab-on-a-chip systems, such as versatility of design, ease of device fabrication and the low operating voltage required for a given desired DEP force, the extremely low throughputs in such systems are a barrier which has seriously hampered the development of dielectrophoretic separation.

An alternative way to improve throughput is to scale up the characteristic dimension of the DEP separator. The first attempts aimed at scaling up DEP systems began with Thöming's research group (Thoeming et al., 2006). Baune et al. (2008) experimentally investigated DEP systems with electrode distances in millimeter-scale, which presented the prospect of applying scaled-up DEP in separation technology. Later, Du et al. (2008) followed the same approach by developing a DEP particle separator for fractionating gold particles from an aqueous suspension of heavy minerals with a high throughput of 141 mL·min^{-1}. To the best of our

knowledge, this throughput is the highest to be reported in the literature so far, with flow rates two orders of magnitude above the previous state of the art and the only one showing potential for DEP application on a production scale. However, it has been limited so far to discontinuous operation, due to local Joule heating. It has been assumed that said problem is attributable to the low volumetric surface of the DEP channel.

A major problem when scaling up a DEP system is the conflict between the dimensions of the electrode configuration, the suspension flow rate and the voltage input for efficient particle movement. For example, to improve the suspension flow rate for a given DEP force acting on a particle, an increase in both characteristic length (i.e., the distance between electrodes) and voltage is required to maintain the same efficiency. On the one hand, a DEP system with low voltage input requires a very small characteristic length to generate sufficient electric fields that could hardly be realized in the case of high flow rates. On the other hand, a DEP system based on a high voltage and a large characteristic length inevitably requires accordingly high energy input, which in turn causes relatively large resistive loss of energy and undesired side effects, such as Joule heating (Castellanos et al., 2003; Du et al., 2013; Wang et al., 2014; Wang et al., 2015; Wood et al., 2013). Joule heating arises due to a high local electric current, and the induced electrothermal effect causes convection of the fluid medium disturbing the particle's dielectrophoretic motion, which is a general DEP problem. This problem becomes significant when scaling up DEP and acts as a constraint on DEP-based particle separation processes aimed at reaching higher throughputs.

The aforementioned problems will be discussed in greater detail in the following chapters.

1.4 Aim of the thesis

Continuous, contact-free separation of sensitive microparticles is still a challenge. As a very promising technique, dielectrophoresis has shown enormous potential for controllable and selectable separation that is almost non-destructive to samples. However, the use of lab-on-the-chip devices with electrode distances in the micrometer range confines the great majority of DEP applications to the analytic scale, with extremely low throughput. In addressing this issue, the first aim of the thesis is to develop a scale-bridging approach, i.e., to scale up both the electrodes and the space between electrodes from the micrometer to the millimeter range, thus enabling large-scale dielectrophoretic microparticle separation to be performed with expected high throughput. To achieve this, a deep understanding of the interplay of DEP channel geometry and electrode concept with respect to induced particle motion is required in order to resolve the aforementioned conflict in DEP scale-up.

The side effect, namely the electrothermal effect induced by Joule heating, arises when the electric potential and the conductivity of the medium are high. This causes natural convection in the medium, thus perturbing the particle's DEP motion. This interference becomes more prominent in enlarged DEP channels, because high voltages are used for effectively manipulating particles. Hence, the second aim of the thesis is to develop a theoretical model for predicting the electrothermal effect and, more importantly, to demonstrate the possibility of reducing or even eliminating Joule heating disturbances in enlarged DEP systems.

For continuous dielectrophoretic binary separation or fractionation of microparticles into different populations, a continuous-flow separation platform is thus required to enable DEP system scale-up. In addition, accurate prediction of a particle's dielectrophoretic behavior helps us to design customized separators achieving separation of a given particle population. Hence, the third aim of the thesis is to develop and optimally design large dielectrophoresis-based separators. By modeling particles' dielectrophoretic motion trajectories within the proposed separators, it is possible to achieve controllable and accurate fractionation at higher throughput.

1.5 Thesis outline

The PhD thesis starts with an overview of representative microparticle separation techniques with regard to their strengths and limitations. The concept of dielectrophoretic separation is introduced as a promising alternative, and the current problems of DEP-based applications are listed. The aims of the thesis as well as the thesis structure are stated.

Chapter 2 describes the detailed theoretical mechanisms of dielectrophoresis and dielectrophoretic force. Apart from DEP force, there are various other forces operating in electrokinetic systems, which act either on particles directly or on the suspending fluid and in turn influence the motion of particles. These forces and force-induced motions are summarized in this chapter as well.

In Chapter 3, the cylindrical interdigitated electrode (cIDE) configuration is selected from among several electrode configurations whose designs meet the requirements of DEP channel scale-up. Both simulation and experimental work are conducted to test the performance of such an electrode array. The undesired electrothermal effect is observed during the experiment, and a model is established for predicting the DEP motion of particles under the interference of the electrothermal flow in a batch dielectrophretic system.

In Chapter 4, the structure of the proposed cIDE electrode configuration as well as the channel geometry are design tailored for controlling particle motion predominantly by DEP while

avoiding electrothermal interference. The model developed in Chapter 3 is employed again for describing particle motion. This model is also evaluated experimentally in a DEP cell with different electrode structure parameters.

A continuous flow-through system is required for high-throughput dielectrophoretic particle separation. Based on the results given by the previous chapters, Chapter 5 presents a tailor-designed dielectrophoretic separator for continuous size-based microparticle fractionation. A single particle tracking model is developed and validated that enables us to estimate particle motion trajectories in continuous-flow systems. The experimental validation is subsequently done by measuring particle motion positions in the separator. Fractionation resolution is also introduced and numerically studied with respect to both design and operation parameters for evaluating the quality of fractionation.

In Chapter 6, a conceptual high-throughput separator with concentrically arranged cIDE electrodes and tuneable sampling tubes is proposed for continuous fractionation of microparticles into different fractions. A Lagrangian particle tracking model is again used to predict microparticle motion trajectories in the separation chamber. The impact of system parameters on particle displacement is numerically studied. The proposed concentric cIDE separator are also compared to the cIDE separator developed in Chapter 5.

In Chapter 7, all the conclusions in the thesis are summarized and an outlook on further work is given.

2 Forces and motions in electrokinetic systems

In electrokinetic systems, a variety of forces acting on particles cause particle motion. Electrical forces arise from the interaction of the applied electric field with the particles and the suspending fluid. A force that occurs in homogenous electric fields is referred to as electrophoretic force; a force that arises in inhomogenous electric fields is referred to as dielectrophoretic force. The latter plays an important role in microparticle separation, especially in *AC* electrokinetic systems, and will be discussed in greater detail in this chapter. Other forces, such as gravitational force or hydrodynamic force, are not dependent on electric field, but play important roles, especially when particles are suspended in a viscous fluid. Besides the forces that act directly on particles, there are also forces which act on the fluid medium and cause fluid motion. This induced fluid motion can be translated into particle motion due to viscous drag. An investigation of these forces and the various kinds of motion they induce is essential for effective and controllable separation of microparticles in electrokinetic systems.

2.1 Dielectrophoresis

Dielectrophoresis (DEP), a translational motion of suspended particles induced by dielectric polarization in an inhomogenous electric field, was firstly defined by Pohl (1951). In contrast to electrophoresis (EP), which is the motion of particles with free net charge produced by the Coulomb force (Kang and Li, 2009), dielectrophoresis requires polarization of the particle and therefore is not confined to charged particles (Pethig, 1996).

2.1.1 Dielectrics and polarization

Dielectrics are dielectric materials (e.g. solid particles) containing charges which can be polarized under the influence of an external electric field. Polarization is related to charge distribution around dielectrics in an electric field. For example, the polarization of a charged spherical particle with free charges on its interface presents a deformation of the double layer of free charges when the external electric field is applied (Fig. 1.1a), whereas neutral particles are polarized by moving charges bound within the dielectric at short distances (Fig. 1.1b). The induced dipoles are formed when negative and positive charges move in opposite directions to produce a dipole moment across the particle. The average dipole moment $\boldsymbol{p}_{av}$, which is proportional to the local electric field $\boldsymbol{E}$, can be described as (Griffiths and College, 1999):

$$\boldsymbol{p}_{av} = \alpha \boldsymbol{E} \tag{2.1}$$

where α is polarizability, which can be considered as a measure of the ablilty of a material to respond to the electric field, and also a measure of the ability of a material to produce charge at interfaces (Morgan and Green, 2003). Generally, there are three basic polarization mechanisms: electronic polarization, atomic polarization and orientational polarization.

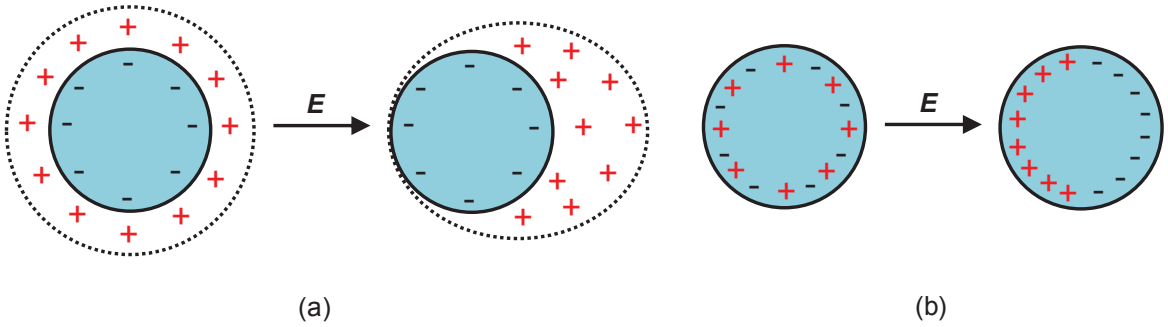

Figure 2.1: A comparison of two different particle polarization mechanisms: charged particle (a) and neutral particle (b) polarized in an electric field. The Figure above is taken from Baune et al. (2008).

2.1.2 Interfacial polarization and surface conductance

In addition to the three polarization mechanisms mentioned above, there is another form of long-range polarization with respect to the accumulation of surface charge at interfaces between different dielectrics due to differences in electrical properties, which is referred to as interfacial polarization (Morgan and Green, 2003).

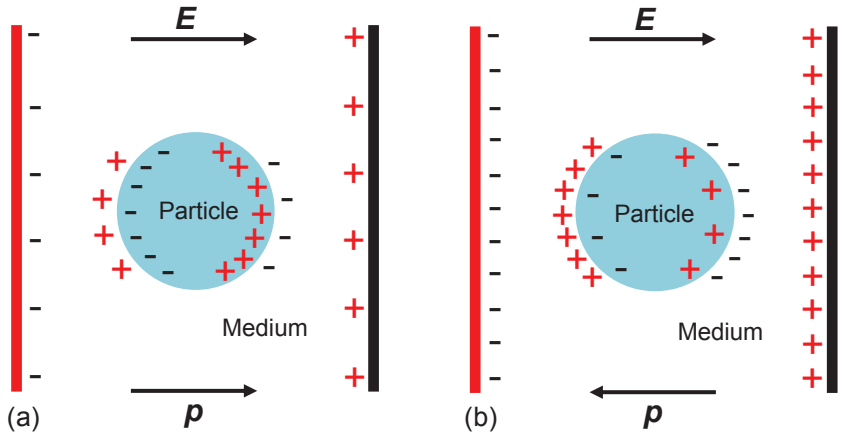

Figure 2.2: Schematic diagram of interfacial polarization of two different dielectrics: (a) the polarizability of the dielectric particle is higher than that of the suspending dielectric medium and (b) the polarizability of the dielectric particle is lower than that of the suspending medium. The Figure above is taken from

Morgan and Green (2003) and slightly modified.

When a dielectric particle is suspended in a dielectric medium and placed in an electric field, the charges inside both the particle and the medium will be redistributed at the particle-medium interface depending on the polarizabilities of both the particle and the medium. If the polarizability of the particle is higher than that of the medium, then more charge will accumulate on the particle side, inducing a net dipole $\boldsymbol{p}$ which is parallel to the applied field (Fig. 2.2a); if the polarizability of the particle is lower than that of the medium, then more charge will accumulate on the medium side, inducing a net dipole which points the opposite direction of the electric field (Fig. 2.2b).

The redistribution of charge means a difference in the charge density on either side of the particle, which gives rise to an induced dipole across the particle and aligned with the applied electric field. This induced or effective dipole moment depends upon the properties of both the particle and the suspending medium, as well as the frequency of the applied field (Morgan and Green, 2003). For a spherical particle of radius a suspended in a medium, the effective dipole moment can be described as (Morgan and Green, 2003):

$$\boldsymbol{p} = \frac{4}{3}\pi a^3 \tilde{\alpha} \boldsymbol{E} \tag{2.2}$$

In Eq. (1.3), $\tilde{\alpha}$ is the complex effective polarizability, which is (Morgan and Green, 2003):

$$\tilde{\alpha} = 3\varepsilon_0 \varepsilon_m \left(\frac{\tilde{\varepsilon}_p - \tilde{\varepsilon}_m}{\tilde{\varepsilon}_p + 2\tilde{\varepsilon}_m} \right) \tag{2.3a}$$

and

$$\tilde{\varepsilon} = \varepsilon_0 \varepsilon - \frac{j\sigma}{\omega} \tag{2.3b}$$

where ε_0 = 8.854×10^{-12} F·m^{-1} is the permittivity of free space, and subscripts p and m represent the particle and the medium, respectively. $\tilde{\varepsilon}$ is the complex permittivity, σ is the conductivity, ω is the angular frequency with $\omega = 2\pi f$, where f is the electric field frequency. j is the imaginary unit with $j = \sqrt{-1}$. As described in Eq. (2.2) and (2.3), the magnitude of the effective polarizability and therefore the effective dipole moment is frequency dependent. This frequency dependence is referred to as the Clausius-Mossotti factor $\tilde{K}$ (Pohl, 1978):

$$\tilde{K} = \frac{\tilde{\varepsilon}_p - \tilde{\varepsilon}_m}{\tilde{\varepsilon}_p + 2\tilde{\varepsilon}_m} \tag{2.4}$$

The Clausius-Mossotti factor $\tilde{K}$, which was extrapolated by Lorrain et al. (2001) for solving the electric potential (Laplace equation) inside and outside the dielectric sphere with boundary conditions based on Gauss's law and the charge conversation equation, describes the relaxation in effective permittivity or polarizability of the particle with the relaxation time τ_{MW} (Morgan and Green, 2003):

$$\tau_{MW} = \frac{\varepsilon_0\varepsilon_p + 2\varepsilon_0\varepsilon_m}{\sigma_p + 2\sigma_m} \tag{2.5}$$

and angular frequency ω_{MW}:

$$\omega_{MW} = 2\pi f_{MW} = \frac{1}{\tau_{MW}} \tag{2.6}$$

The angular frequency ω_{MW} is referred to as the Maxwell-Wagner relaxation frequency, since the dispersion in the dipole moment is caused by interfacial polarization. The Maxwell-Wagner interfacial polarization mechanism is thus a frequency-dependent polarization process that arises from the motion of charges at the interface between particle and suspending electrolyte (Morgan and Green, 2003).

Since the Maxwell-Wagner relaxation frequency is both dependent on both conductivity and permittivity (Eq. (2.5)), said frequency can be easily determined in certain circumstances by acquiring the dielectric properties of both the particle and the suspending medium. However, dielectric measurements show that, for charged particles, the Maxwell-Wagner relaxation frequency is higher than is expected from theory, indicating that the actual particle conductivity is higher than expected. This can be explained by the inclusion of surface conductance in the derivation of the particle's dipole moment and by the surface conductance effect dominating the dielectric properties of these particles in the Maxwell-Wagner relaxation frequency regime (O'Konski, 1960). For the conductivity of a solid homogeneous spherical particle σ_p, O'Konski (1960) proposed an expression which is given by the sum of the bulk conductivity of a particle $\sigma_{p,bulk}$ and a surface conductivity term $\sigma_{p,surface}$,as:

$$\sigma_p = \sigma_{p,bulk} + \sigma_{p,surface} \tag{2.7}$$

The surface conductivity of the particle is given by:

$$\sigma_{p,surface} = \frac{2K_S}{a} \tag{2.8}$$

where K_S is the surface conductance. This expression has been used to model the frequency dependent dielectric and dielectrophoretic behavior of particles larger than 1 μm.

However, it was considered to be inaccurate for describing the surface properties of small particles (Ermolina and Morgan, 2005).

In general, the surface of a small particle (e.g. submicroparticle or nanoparticle) is more liable to carry net charge (either positive or negative charge) produced either by dissociation of the chemical groups or by adsorption of ions from the solution. This surface charge generates an electrostatic surface potential. When the surface is exposed to an electrolyte, the surface potential attracts counterions and repels co-ions, thus forming the electric double layer (Fig. 2.3). The region near the interface with a higher density of counterions and a lower density of co-ions than the bulk is referred to as the diffuse layer. The region between the surface and the diffuse layer with tightly associated counterions is referred to as the Stern layer. The potential in the Stern layer region is assumed to fall linearly from the surface potential ϕ_0 to the Stern layer potential ϕ_d, before decaying exponentially across the diffuse layer to a potential of ζ, which is referred to as the zeta potential (Fig. 2.3).

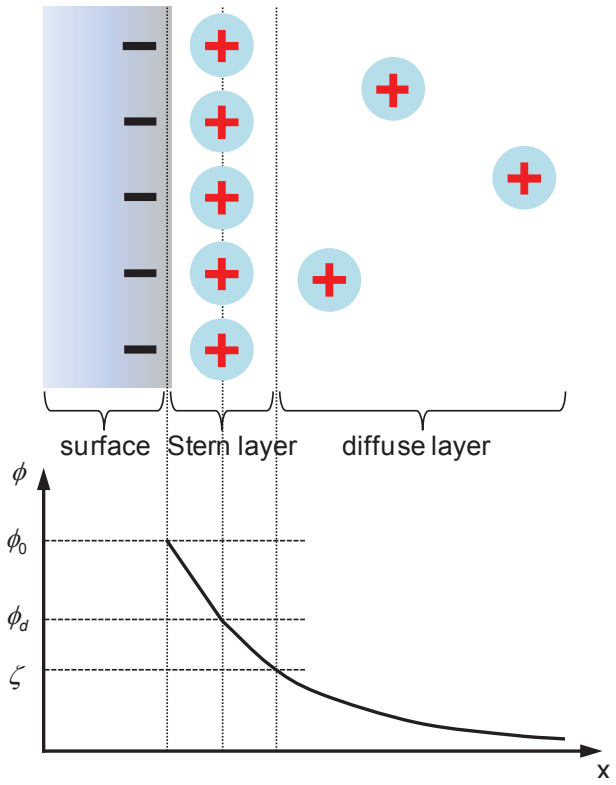

Figure 2.3: Schematic diagram of double layer formation. The potential varies with distance x from the surface to the bulk. The Figure above is taken form Morgan and Green (2003) and slightly modified.

Due to the potential differences between the diffuse layer and the Stern layer, the total surface conductance can thus be divided into two distinct components, one being the conduction K_{Diff}

in the diffuse part of the double layer and the other being the conduction K_{Stern} behind the slip plane in the Stern layer, and expressed as (Dukhin and Deriaguine, 1974; Lyklema, 2005):

$$K_S = K_{Stern} + K_{Diff} \tag{2.9}$$

Eq. (2.7) then becomes:

$$\sigma_p = \sigma_{p,bulk} + 2\frac{K_{Stern}}{a} + 2\frac{K_{Diff}}{a} \tag{2.10}$$

The Stern layer conductance is given by (Ermolina and Morgan, 2005):

$$K_{Stern} = \rho_{q,Stern}\mu_{Stern} \tag{2.11}$$

where $\rho_{q,Stern}$ and μ_{Stern} are the surface charge density and ion mobility in the Stern layer, respectively.

The diffuse layer conductance, which is typically one to two orders of magnitude lower than the Stern layer conductance, consists of two components, the electroosmostic conductance $K_{Diff,eo}$ and the movement of charge with respect to the liquid $K_{Diff,m}$. The diffuse layer conductance can be expressed as (Ermolina and Morgan, 2005):

$$K_{diff} = K_{diff,m} + K_{diff,eo} = \frac{4F^2cz_i^2D_e(1+3m/z_i^2)}{R_gT\kappa}(\cosh\left[\frac{z_iq\zeta}{2k_bT}\right]-1) \tag{2.12}$$

where F is the Faraday constant, c is electrolyte concentration, z_i is the valence of the counterion, D_e is the diffusion coefficient of the excess free charge in the diffusion layer, R_g is the gas constant, T is the absolute temperature, q is the charge on the electron and k_b is Boltzmann's constant. ζ is the zeta potential, a potential located at the slipping plane relative to a point in the bulk fluid away from the interface. The inverse Debye length κ is given by (Ermolina and Morgan, 2005):

$$\kappa = \sqrt{(2cz_iF^2)/(\varepsilon_0\varepsilon_mR_gT)} \tag{2.13}$$

The dimensionless parameter m is the contribution of the electroosmotic ion flux to the diffuse layer surface conductance, as (Ermolina and Morgan, 2005):

$$m = \left(\frac{R_gT}{F}\right)^2\frac{2\varepsilon_0\varepsilon_m}{3\mu_mD_e} \tag{2.14}$$

where μ_m is the dynamic viscosity of the suspending medium. For aqueous solutions of most ions at room temperature, m is about 0.15; however, for the hydrogen ion H+, m is about

0.03 (Lyklema and Minor, 1998).

2.1.3 Dielectrophoretic force

As mentioned above, particles can be polarized in the presence of an electric field. If the electric field is uniform, the redistribution of charge on either side of a particle is equal and opposite, so the particle is merely polarized (see Fig. 2.2). In the case of a non-uniform electric field, in contrast, the local fields on either side of the particle are different (Figs. 2.4c and 2.4d). A net force arises ($\boldsymbol{F}_{DEP}$) which is produced by the interaction of the induced effective dipole moment of the particle with the non-uniform electric field, given by the following equation (Jones, 1995):

$$\boldsymbol{F}_{DEP} = (\boldsymbol{p} \cdot \nabla)\boldsymbol{E} \tag{2.15}$$

It should be noted that Eq. (2.15) is only valid with the assumption that the particle dimensions are much smaller than the spatial change of the electric field, which is referred to as the point dipole approximation (Al-Jarro et al., 2007; Nili et al., 2011). This assumption does not hold when the particle is close to a null field, or the magnitude of the local electric field varies significantly across particle dimensions. This equation also describes the force on the effective dipole moment, which is based on the spherical particle and all higher-order moments are neglected. However, some non-spherical particles can have significant higher-order components, and in some cases these moments strongly influence the observable motion (Green and Jones, 2006). In these cases, the induced higher-order multiple moments other than dipole moment must be considered (Jones and Washizu, 1996; Wang et al., 1997). An alternative and more accurate approach, i.e., the Maxwell stress tensor (MST), can be used to determine the dielectrophoretic force (Li and Qian, 2013; Wang et al., 1997) which is applicable to particles of arbitrary shape and size.

In an *AC* electric field, the time-averaged force on a spherical particle can be expressed as a function of the real part of the complex effective polarizability $\tilde{\alpha}$. By substituting Eq. (2.2) into Eq. (2.15), the force is:

$$\boldsymbol{F}_{DEP} = \frac{4}{3}\pi a^3 Re[\tilde{\alpha}(\boldsymbol{E} \cdot \nabla)\boldsymbol{E}^*] \tag{2.16}$$

where $\boldsymbol{E}^*$ is the complex conjugate of the electric field. In an *AC* electric field with spatially varying field magnitude and constant phase (the phases in this case are real), and with the complex effective polarizability $\tilde{\alpha}$ being replaced by the Clausius-Mossotti factor $\tilde{K}$ (Eq.

(2.4)), the full expression of the time-averaged DEP force on a spherical particle is (Jones, 1995; Morgan and Green, 2003):

$$\boldsymbol{F}_{DEP} = 4\pi a^3 \varepsilon_0 \varepsilon_m Re[\tilde{K}](\boldsymbol{E}\cdot\nabla)\boldsymbol{E} \tag{2.17}$$

where $(\boldsymbol{E}\cdot\nabla)\boldsymbol{E}$ is the electric field factor, which can be expressed as $(\boldsymbol{E}\cdot\nabla)\boldsymbol{E} \approx \frac{1}{2}\nabla|\boldsymbol{E}|^2$ in the case of linear and isotropic dielectrics (Pohl, 1978). The variation in the magnitude of the DEP force with frequency is given by the real part of the Clausius-Mossotti factor $Re[\tilde{K}]$:

$$Re[\tilde{K}] = \frac{(\sigma_p - \sigma_m)(\sigma_p + 2\sigma_m) + (2\pi f)^2 \varepsilon_0{}^2 (\varepsilon_p - \varepsilon_m)(\varepsilon_p + 2\varepsilon_m)}{(\sigma_p + 2\sigma_m)^2 + (2\pi f)^2 \varepsilon_0{}^2 (\varepsilon_p + 2\varepsilon_m)^2} \tag{2.18}$$

Since $\tilde{K}$ represents the particle's effective polarizability and the direction of DEP force is therefore dependent on the sign of the $Re[\tilde{K}]$. Depending on $Re[\tilde{K}]$, the particle can experience either positive DEP (p-DEP), which means the particle is more polarizable than the suspending medium and the DEP force induces particle motion toward stronger electric fields (Fig. 2.4c), or negative DEP (n-DEP), which means the particle is less polarizable than the suspending medium and the DEP force induces particle motion toward the region with a weaker electric field (Fig. 2.4d).

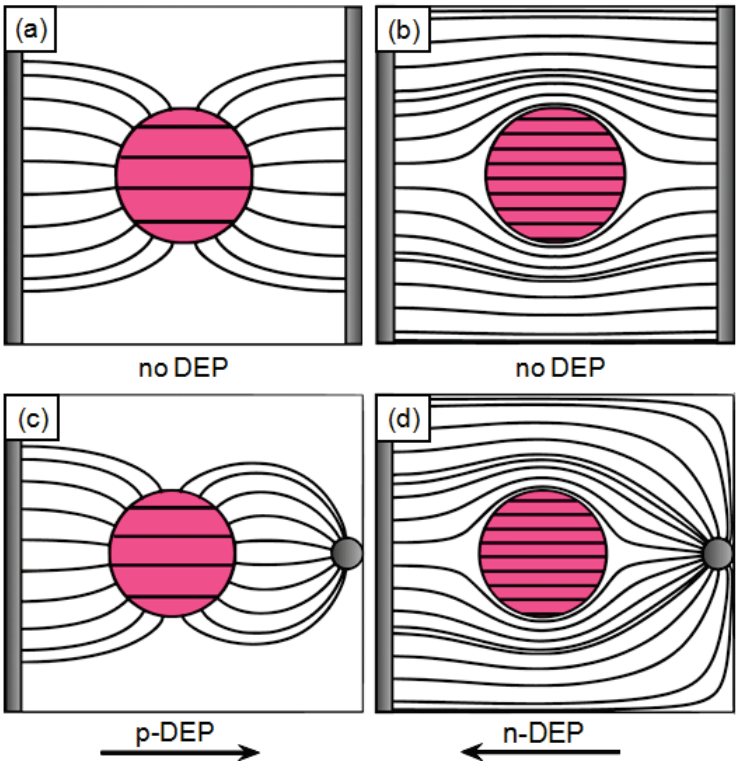

Figure 2.4: Electric field lines show a particle which is more polarizable (**(a)** and **(c)**) or less polarizable (**(b)** and **(d)**) than the suspending medium in a uniform (**(a)** and **(b)**) or a non-uniform (**(c)** and **(d)**) electric field. The arrows represent the direction of the induced DEP force and movement in this case.

(adapted from Morgan and Green (2003))

In a homogeneous electric field, the forces acting on opposite ends of the particle are equal and there is no net movement (Figs. 2.4a and 2.4b), whereas in an inhomogenous electric field, the forces acting on either side are different, and the net force (DEP) results in movement of the particle (Figs. 2.4c and 2.4d). The DEP force thus arises due to the difference in local electric field on the two sides of the polarized particle, thereby initiating translational motion of the particle (Jones, 1995; Neculae et al., 2012; Pethig and Markx, 1997). Since the direction of a particle's dielectrophoretic motion is independent of the sign of the electric field, the particle does not have to carry a net electric charge for motion to be induced and, therefore current (*DC*) as well as alternating current (*AC*) can be applied to superimpose an electric force field on a particle (Huang et al., 2001; Pethig, 2013). Eq. (2.17) indicates that the dielectrophoretic force depends upon the difference in polarizability between the particle and the surrounding medium. The force is also proportional to the size (volume) of the particle, and to the gradient of the electric field. DEP separation can thus be based on differences in size or polarizability, or a combination of the two properties.

2.2 Forces and particle dynamics

Forces acting on particles give rise to particle movement in the fluid medium. There are basically two types of forces which induce particle movement in electrohydrodynamic systems: intrinsic forces and externally imposed forces. Externally imposed forces which are size dependent, such as gravitational force, predominate in particle separation processes on the micrometer scale. In addition to gravitational force, there are also electrical forces that arise in local uniform or non-uniform electric fields and which cause particle motion. Intrinsic processes such as Brownian motion originates in the thermal energy, causing suspended particles to move in a random manner. This uncontrolled force becomes dominant at reduced particle size, meaning that it should be considered for some cases of micron-sized particle separation.

2.2.1 Gravity

In a gravitational field, a particle with volume V_p and mass density ρ_p experiences buoyancy when suspended in a fluid medium with mass density ρ_m. According to Newton's Second Law, this force can be written as:

$$\boldsymbol{F}_g = m\boldsymbol{g} = V_p\left(\rho_m - \rho_p\right)\boldsymbol{g} \tag{2.19}$$

where $\boldsymbol{g}$ is gravitational acceleration. If the mass density of particle ρ_p is greater than the medium ρ_m, the gravitational force is downward, and vice versa. For a spherical particle, the gravitational force can be expressed as:

$$\boldsymbol{F}_g = \frac{4}{3}\pi a^3 \left(\rho_m - \rho_p\right)\boldsymbol{g} \tag{2.20}$$

2.2.2 Hydrodynamic drag

In the presence of hydrodynamic flow, a drag force acts on the spherical particles. The traditional form of the hydrodynamic drag force equation can be stated as follows (Leal, 2007):

$$\boldsymbol{F}_{drag} = \frac{1}{2}\pi a^2 \rho_m C_D (\boldsymbol{u}_m - \boldsymbol{u}_p)^2 \tag{2.21}$$

where $\boldsymbol{u}_m$ and $\boldsymbol{u}_p$ are the velocities of the fluid and the particle, respectively. C_D is the drag coefficient, which depends on the Reynolds number of the particle Re_p, given by (Clip et al., 1978):

$$C_D = \begin{cases} \dfrac{24}{\mathrm{Re}_p} & \text{if} \quad \mathrm{Re}_p < 0.1 \\ \dfrac{24}{\mathrm{Re}_p}\left(1+0.15\mathrm{Re}_p^{0.687}\right) & \text{if} \quad \mathrm{Re}_p > 0.1 \end{cases} \tag{2.22}$$

and

$$\mathrm{Re}_p = \frac{2a\rho_m \left|\boldsymbol{u}_m - \boldsymbol{u}_p\right|}{\mu_m} \tag{2.23}$$

When a particle moves through a fluid medium with a low Reynolds-number limit (Re_p <0.1), it experiences a viscous drag which is approximately proportional to the velocity of the particle ($\boldsymbol{u}_p$) relative to the suspending medium ($\boldsymbol{u}_m$), but opposite in direction. Substituting Eqs. (2.22) and (2.23) into Eq. (2.21), the viscous drag force can be described as (Leal, 2007):

$$\boldsymbol{F}_{drag} = 6\pi a \mu_m (\boldsymbol{u}_m - \boldsymbol{u}_p) \tag{2.24}$$

The expression of the viscous drag force (Eq. (2.24)) is known as Stokes' drag with a Stokes' drag coefficient f_s (Leal, 2007):

$$f_s = 6\pi a \mu_m \tag{2.25}$$

2.2.3 Electrical forces

In electrohydrodynamic systems, the major electric forces acting on particles suspended in a fluid are electrophoretic force and dielectrophoretic force.

Electrophoresis (EP) is the motion of particles with a non-zero net charge under the influence of an applied electric field. The external electric field exerts an electrostatic Coulomb force which acts on charged particles and causes particle motion toward the electrode of opposite charge to that of the particle. The Coulomb force on a particle in electrophoresis, as stated by Morgan and Green (2003), is:

$$\boldsymbol{F}_{EP} = Q_{tot}\boldsymbol{E} \tag{2.26}$$

where Q_{tot} is the total charge on the particle.

When particles are suspended in an aqueous medium, an electrical double layer forms around the particle in order to maintain electric neutrality, so that the particle is electroneutral overall. The particle therefore appears to have zero net charge, but when placed in an electric field it moves. This is due to the mobility of ions in the double layer, which is referred to as the electrophoretic mobility (μ_E). This electrophoretic mobility results in a constant velocity $\boldsymbol{v}_{EP}$ of the particle suspended in a viscous medium, which is stated as follows (Morgan and Green, 2003):

$$\boldsymbol{v}_{EP} = \mu_E\boldsymbol{E} \tag{2.27}$$

Generally, the electrophoretic mobility of a particle depends on the thickness of the double layer in relation to the size of the particle, i.e., the ratio of the particle radius to the Debye length given by κa . For a particle with a thin double layer ($\kappa a \gg 1$), the electrophoretic mobility is defined by the well-known Helmholtz-Smoluchowski equation (Ermolina and Morgan, 2005):

$$\mu_E = \frac{\varepsilon_0\varepsilon_m\zeta}{\mu_m} \tag{2.28}$$

When a particle has a thick double layer ($\kappa a \ll 1$), the electrophoretic mobility is defined by Hückel's equation (Hunter, 2003):

$$\mu_E = \frac{2\varepsilon_0\varepsilon_m\zeta}{3\mu_m} \tag{2.29}$$

A factor of at most 1.5 was found to describe the difference between the high and the low limits of κa. For the electrophoretic mobility of arbitrary values of κa, Henry (1931) and Ohshima (2001) developed an expression:

$$\mu_E = \frac{2}{3}\frac{\varepsilon_0 \varepsilon_m}{\mu_m}\left(1+\frac{1}{2\left[1+2.5/\left\{\kappa a(1+2e^{-\kappa a})\right\}\right]^3}\right) \tag{2.30}$$

A dipole moment is induced in a dielectric particle suspended in a medium when placed in a non-uniform electric field. A net force is produced by the interaction of the induced dipole moment of the particle with the non-uniform electric field and is referred to as the dielectrophoretic force. A detailed description of the mechanism of dielectrophoresis and the dielectrophoretic force can be found in the previous section.

The motion of a particle suspended in an aqueous medium and subjected to a dielectrophoretic effect can be assumed to be in steady state. In this case, the dielectrophoretic force (Eq. (2.17)) and the viscous drag force (Eq. (2.24)) are balanced. For a spherical microparticle, the steady-state dielectrophoretic particle velocity can be expressed as (Morgan and Green, 2003):

$$\boldsymbol{v}_{DEP} = \frac{2a^2 \varepsilon_0 \varepsilon_m Re[\tilde{K}]}{3\mu_m}\left(\boldsymbol{E}\cdot\nabla\right)\boldsymbol{E} \tag{2.31}$$

The fluid medium in this equation is assumed to be static and the particle moves in the Stokes regime. The steady-state particle DEP velocity depends on the particle radius, the real part of the Clausius-Mossotti factor, the permittivity and viscosity of the fluid and, most importantly, the electric field factor $\left(\boldsymbol{E}\cdot\nabla\right)\boldsymbol{E}$.

However, the high electric potential applied in electrokinetic systems causes fluid motion due to Joule heating. The motion of the fluid medium disturbs the particle's DEP motion and should be taken into account when calculating particle velocity. The detailed motion of the fluid induced by Joule heating will be discussed later.

2.2.4 Brownian motion

All particles suspended in a fluid medium undergo Brownian motion, the scale of which is dependent on both particle size and the viscosity of the suspending medium. Brownian motion can cause significant particle displacements and velocities in comparison with typical deterministic forces such as DEP or gravity, particularly for sub-micron and nanoparticles. We currently have little control over this force, although this does not mean that Brownian motion cannot be predicted. According to Einstein's theory, the average particle displacement from

one position to another position tends to be zero. However, the *root mean square* (*rms*) of the displacement of the particle in one dimension is non-zero, which follows a Gaussian profile and could be expressed as (Einstein, 1956):

$$\Delta x = \sqrt{2Dt_d} \tag{2.32}$$

where D is the diffusion coefficient for the particle. t_d is the elapsed time of the Gaussian probability distribution for the particle. For a spherical particle with radius *a* suspended in a medium with dynamic viscosity μ_m, the diffusion coefficient is defined by the Stokes-Einstein equation (Probstein, 2005):

$$D = \frac{k_b T}{6\pi\mu_m a} \tag{2.33}$$

Eq. (2.33) is considered meaningful only for a single isolated particle. For a collection of particles, diffusion of the ensemble must be considered.

2.3 Fluid dynamics

In many situations, the local field in the electrokinetic system also produces body forces on the fluid, setting it into motion and thus resulting in the movement of suspended particles. A deep understanding of such fluid motion is essential when designing DEP separation devices and for improved control of particle separation.

2.3.1 Fluid flow

The motion of fluids is described by the Navier-Stokes equations and by the continuity equation. For an incompressible, Newtonian fluid with given body forces, it is expressed (Morgan and Green, 2003) as:

$$\nabla \boldsymbol{u}_m = 0 \tag{2.34}$$

$$\rho_m \frac{\partial \boldsymbol{u}_m}{\partial t} + \rho_m \left(\boldsymbol{u}_m \cdot \nabla\right)\boldsymbol{u}_m = -\nabla p + \mu_m \nabla^2 \boldsymbol{u}_m + \boldsymbol{f}_{tot} \tag{2.35}$$

where t is time, p is pressure and $\boldsymbol{f}_{tot}$ is the total applied force. Eq. (2.35) can be simiplified by examining the scale of the system with respect to the ratio of the inertial term to the viscous term, and determined by a factor which is referred to as the Reynold's number of the fluid (Castellanos et al., 2003):

$$\frac{\rho_m(\boldsymbol{u}_m \cdot \nabla)\boldsymbol{u}_m}{\mu_m \nabla^2 \boldsymbol{u}_m} \sim \mathrm{Re} = \frac{\rho_m \boldsymbol{u}_m L_c}{\mu_m} \tag{2.36}$$

where L_c is the characteristic length of the system. If the $\mathrm{Re} \ll 1$, then the viscous term dominates the fluid, where inertial term can be neglected; If the $\mathrm{Re} \gg 1$, then the inertial term dominates the fluid, and the viscous term can be neglected (Morgan and Green, 2003).

2.3.2 Electrothermal force

The strong electric fields that are commonly applied in DEP systems will invariably generate Joule heating, which gives rise to fluid motion and in turn results in viscous drag force on particles. The temperature gradients and thus the fluid flow induced by Joule heating is referred to as the electrothermal effect. There are principally two types of volume force initiated by Joule heating: electrothermal force ($\boldsymbol{f}_E$) due to gradients in conductivity and permittivity, and buoyancy force ($\boldsymbol{f}_B$) arising from gradients in fluid density (Ramos et al., 1998). In electrokinetic systems, the total applied force $\boldsymbol{f}_{tot}$ in Eq. (2.35) could be considered as a sum of the electrothermal force $\boldsymbol{f}_E$ and the buoyancy force $\boldsymbol{f}_B$ (Castellanos et al., 2003):

$$\boldsymbol{f}_{tot} = \boldsymbol{f}_E + \boldsymbol{f}_B \tag{2.37}$$

Both the electrothermal force and the buoyancy force can induce fluid motion when they dominate fluid flow in systems of different scale.

The inhomogenous electric fields used in DEP-based devices not only produce a DEP force for manipulating particles, but also generate electric volume force in the medium by initiating gradients in conductivity and permittivity due to Joule heating. The time-averaged electrothermal body force in terms of conductivity and permittivity gradients is given by (Ramos et al., 1998):

$$\boldsymbol{f}_E = \frac{1}{2}\mathrm{Re}\left[\left(\frac{(\sigma_m \nabla \varepsilon_m - \varepsilon_0 \varepsilon_m \nabla \sigma_m)\cdot \boldsymbol{E}}{\sigma_m + j\omega\varepsilon_0\varepsilon_m}\right)\boldsymbol{E}^* - \frac{1}{2}|\boldsymbol{E}|^2 \nabla \varepsilon_m\right] \tag{2.38}$$

As discussed by Ramos et al. (1998), the conductivity gradient produces free volume charge and the Coulomb force (the first term on the right-hand side of Eq. (2.38)), whilst the permittivity gradient produces the dielectric force (the second term on the right-hand side of Eq. (2.38)). The electrical body force is also frequency-dependent: in certain frequency ranges, either Coulomb force (low frequencies) or dielectric force (low frequencies) dominates (Morgan and Green, 2003).

Since the gradients of both conductivity and permittivity were caused by temperature changes, $\nabla\varepsilon_m = (\partial\varepsilon_0\varepsilon_m / \partial T)\nabla T$ and $\nabla\sigma_m = (\partial\sigma_m / \partial T)\nabla T$. Thus Eq. (2.38) can be written as temperature gradient-dependent, as stated by (Castellanos and Perez, 1998):

$$\boldsymbol{f}_E = \frac{1}{2}\mathrm{Re}\left[\frac{(\sigma_m(\partial\varepsilon_0\varepsilon_m / \partial T) - \varepsilon_0\varepsilon_m(\partial\sigma_m / \partial T)}{\sigma_m + j\omega\varepsilon_0\varepsilon_m}(\nabla T \cdot \boldsymbol{E})\boldsymbol{E}^* - \frac{1}{2}(\partial\varepsilon_0\varepsilon_m / \partial T)\nabla T|\boldsymbol{E}|^2\right] \tag{2.39}$$

The change in the local temperature field can be expressed by applying the energy balance equation (Castellanos et al., 2003):

$$\rho_m c_p \frac{\partial T}{\partial t} + \rho_m c_p \boldsymbol{u}_m \cdot \nabla T = k\nabla^2 T + \sigma_m |\boldsymbol{E}|^2 \tag{2.40}$$

where c_p is the specific heat capacity, k is the thermal conductivity of the fluid and $\sigma_m|\boldsymbol{E}|^2$ is the Joule heating term. The distribution of temperature field is assumed to rapidly reach a stationary state, so the first term on the left hand can be neglected. Moreover, Eq. (2.40) could be further simplified by the ratio of the heat convection term ($\rho_m c_p \boldsymbol{u}_m \cdot \nabla T$) to the heat diffusion term ($k\nabla^2 T$), which is related to the Pelect number Pe (Castellanos et al., 2003):

$$\frac{|\rho_m c_p(\boldsymbol{u}_m \cdot \nabla)T|}{|k\nabla^2 T|} \sim \mathrm{Pe} = \frac{\rho_m c_p \boldsymbol{u}_m L}{k} \tag{2.41}$$

If $\mathrm{Pe} \ll 1$, then the heat diffusion term dominates, and the convection term can be neglected; if $\mathrm{Pe} \gg 1$, then the convection term dominates, and the diffusion term can be neglected. In microsystems, heat convection is neglected, since the calculated Pelect number is much lower than unity ($\mathrm{Pe} \ll 1$). Equation (2.40) is then reduced to Poisson's equation (Castellanos et al., 2003):

$$k\nabla^2 T = -\sigma_m \boldsymbol{E}^2 \tag{2.42}$$

Ramos et al. (1998) proposed an order-of-magnitude estimation of the incremental temperature rise by substituting for the electrical field in Eq. (2.42):

$$\Delta T \approx \frac{\sigma_m U^2}{k} \tag{2.43}$$

where U is the applied voltage. For the two co-planar electrode configuration applied in Castellanos et al. (2003), the temperature increment can be described by substituting the electric field into Eq. (2.42):

$$\Delta T = \frac{\sigma_m U^2}{2k}\left(\frac{\theta}{\pi} - \frac{\theta^2}{\pi^2}\right) \tag{2.44}$$

where θ is the angle measured from one electrode. Therefore, the analytical expression for the electrothermal body force $\boldsymbol{f}_E$ can be given by combining Eq. (2.39) and Eq. (2.44), as follows (Castellanos et al., 2003):

$$\boldsymbol{f}_E = -M\frac{\varepsilon_0\varepsilon_m\sigma_m U^4}{8k(\pi d_r)^3 T}\left(1-\frac{2\theta}{\pi}\right) \tag{2.45}$$

where d_r is the radial distance from the center of co-planar electrodes. M is dimensionless factor with a value between -0.6 and +6.6 for T = 300 K, and defined as (Castellanos et al., 2003):

$$M = \frac{(T/\sigma_m)(\partial\sigma_m/\partial T)-(T/\varepsilon_0\varepsilon_m)(\partial\varepsilon_m/\partial T)}{1+(\omega\varepsilon_0\varepsilon_m/\sigma_m)^2}+\frac{1}{2}\frac{T}{\varepsilon_0\varepsilon_m}\frac{\partial\varepsilon_m}{\partial T} \tag{2.46}$$

In DEP microsystems with a characteristic system length L_c smaller than 1 mm, an order of magnitude estimation shows that the buoyancy force is negligible compared to the electrothermal force, so the fluid flow in microsystems can be considered as the flow induced by electrothermal force (Castellanos et al., 2003). By substituting Eq. (2.45) into Eq. (2.35), the maximum fluid velocity at $\theta = \frac{\pi}{2}$ can be stated as (Castellanos et al., 2003):

$$u_m = 5.28\times10^{-4}\frac{M}{T}\frac{\varepsilon_0\varepsilon_m\sigma_m U^4}{k\mu_m d_r} \tag{2.47}$$

It can be seen from Eq. (2.47) that the fluid motion initiated by electrothermal body force in microsystems is dependent on the applied voltage to the power of 4, indicating a significant influence of voltage variation on flow velocity. In addition to voltage, there is also a linear dependence on conductivity, i.e., the electrothermal force dominates fluid flow at high conductivities. The characteristic system length, the operating temperature and the frequency of the AC signal, as well as the dielectric, thermal and hydrodynamic properties of the fluid can also influence flow motion. Electrothermal flow can therefore be a dominant problem in microsystems for dielectrophoretic particle separation.

2.3.3 Buoyancy force

In addition to electrothermal force, gravity also applies a body force on the fluid, thus causing fluid motion. In general, the gravitational body force or buoyancy force generated on the fluid by a temperature field is due to the change in local density caused by temperature difference (Morgan and Green, 2003):

$$\boldsymbol{f}_B = \Delta\rho_m\boldsymbol{g} = \frac{\partial\rho_m}{\partial T}\Delta T\boldsymbol{g} \tag{2.48}$$

Dimensional analysis shows that, in microsystems, the buoyancy force is unimportant in comparison with the electrothermal force. However, with increments in the characteristic length of the system, the magnitude of gravitational force becomes even greater than the electrothermal force. Castellanos et al. (2003) numerically calculated different types of fluid motion and pointed out that, when the order of magnitude of the system's characteristic length (L_c) is larger than 1 mm, the buoyancy body force which is exerted on the fluid and is generated by the temperature difference resulting from Joule heating drives recirculation of fluid flow between regions of higher electric field strength and regions of lower electric field strength. This numerical prediction was supported by the experimental analysis conducted by Arnold and Chapman (2000) and Arnold (2001), who observed large convection rolls driven by Joule heating-induced buoyancy force in a millimeter-scale system.

Du et al. (2007) developed a new model to predict fluid motion in millimeter systems. With system scaling up from micron to millimeter scale, i.e. increasing system dimension, more electric power is required for providing non-uniform electric field and consequently, joule heating increases. Since channel width could not be neglected due to the closed magnitude compared to system characteristic length (L_c), energy balance Eq. (2.40) becomes (Boussinesq, 1903; Du et al., 2007):

$$\rho_m c_p \frac{\partial T}{\partial t} + \rho_m c_p \boldsymbol{u}_m \cdot \nabla T = k \nabla^2 T + q_{gen} \tag{2.49}$$

where q_{gen} is the heat generation in a system in which the medium has a specific volume V, defined as (Du et al., 2007):

$$q_{gen} = \frac{U^2}{R_s} \cdot \frac{1}{V} \tag{2.50}$$

where R_s is the resistance of the entire system. It is assumed in this equation that all of the heat generated from resistance heats the fluid within the model system.

In millimeter-scale systems, heat convection is large compared to heat diffusion, as can be calculated using the Pelect number in Eq. (2.41), which is much larger than unity ($\mathrm{Pe} \gg 1$). In addition, the temperature field can be assumed to rapidly reach steady state after application of the electric field. Eq. (2.49) thus becomes:

$$\rho_m c_p V \boldsymbol{u}_m \nabla T = \frac{U^2}{R_s} \tag{2.51}$$

Here, the temperature gradient can be approximated using the relation:

$$\nabla T \approx \frac{\Delta T}{L_c} \tag{2.52}$$

By combining Eqs. (2.51) and (2.52), the temperature increment in millimeter systems can be described as (Du et al., 2007):

$$\Delta T = \frac{U^2 L_c}{R_s \rho_m c_p V \boldsymbol{u}_m} \tag{2.53}$$

Since fluid motion is dominated by buoyancy body force in millimeter-scale systems, the electrothermal body force can be neglected (Du et al., 2007). By substituting Eq. (2.48) into Eq. (2.35), the fluid velocity term is given as:

$$\mu_m \nabla^2 \boldsymbol{u}_m = \frac{\partial \rho_m}{\partial T} \Delta T \boldsymbol{g} \tag{2.54}$$

The change of density caused by the temperature gradient depends on the volumetric thermal expansion coefficient α_v, which is:

$$\alpha_v = \frac{1}{\rho_m} \frac{\partial \rho_m}{\partial T} \tag{2.55}$$

By combining Eqs. (2.53), (2.54) and (2.55), the fluid velocity initiated by the buoyancy volume force can be expressed as (Du et al., 2007):

$$u_m = U \sqrt{\frac{\alpha_v g L_c^{\ 3}}{V c_p \mu_m R_s}} \tag{2.56}$$

Eq. (2.56) indicates that the buoyancy force induced by fluid motion governs millimeter-scale systems, depending on the applied voltage, characteristic length of the system as well as dielectric, thermal and hydrodynamic properties of the fluid.

3 Dielectrophoresis in aqueous suspension: impact of electrode configuration

Dielectrophoresis allows to moving neutral or charged particles in liquids by supplying a non-uniform electric field. When using alternating current and insulated electrodes this is possible in conducting media such as aqueous solutions. With scaling up DEP channel to reach higher throughput, relatively high field strengths and hence DEP forces are required for effectively moving particles in the enlarged DEP systems, i.e. both the electrodes and distance between electrodes are in millimeter-scale. Traditional electrode configurations could hardly meet the requirements in DEP system scale-up due to geometry limitations and high energy consumptions. These drawbacks allow us to study the structure of the electrodes and design novel electrode configurations that can be used in large DEP devices for dielectrophoretic microparticle separation.

In addition, high field strength applied in aqueous solution causes the undesired electrothermal effect due to Joule heating. This electrothermal effect induces motion of the suspending medium and thus disturbances particle's DEP motion. Another side effect which is generated by the interaction of insulated electrodes and the conductive aqueous medium, termed as high-pass-filter effect. The high-pass-filter effect allows strong electric signals only at high frequencies and hence influences the effective voltage across the electrode when system frequency is low. Both side effects and their impacts will be discussed in this chapter.

Parts of this chapter have been published on the Journal "*Microfluids and Nanofluidics"* (Wang et al., 2014).

3.1 Electrode and flow channel design

For continuous separation, the fluid flow has to be split into two or more streams. The bigger the difference achieved in particle concentrations of these streams, the higher the separation factor. This in turn depends on particle trajectories, which results from the superimposed force, i.e. the dielectrophoretic force. As indicated in Eq. (2.17), the dielectrophoretic force field can be described by the field factor, which is referred to as the gradient of square of electric field $\nabla|\boldsymbol{E}|^2$. Pohl (1978) gives an order of magnitude relation of the gradient of square of the electric field on its parameters:

$$\nabla|\boldsymbol{E}|^2 \propto \frac{U^2}{L^3} \tag{3.1}$$

where L is the distance between electrodes in this case. It can be seen form Eq. (3.1) that, the gradient of square of the electric field and hence the dielectrphoretic force is proportional to the square of the applied voltage while inversely proportional to the cubic of the electrodes distance.

According to the relationship between particle trajectories on the one hand and electrode configuration and fluid flow direction on the other hand, electrode arrangement in the flow channel is a key element of a DEP separator. Principally there are two options, orthogonal and horizontal arrangements. In the orthogonal electrode arrangement (Fig. 3.1a), two electrodes are oppositely installed on two sides of the channel with fluid flowing in between both electrodes. Differently, in the horizontal electrode arrangement (Fig. 3.1b), electrodes are installed on one side of channel and the fluid passes them subsequently. Typically, the horizontal electrode arrangement is realized as an array (Fig. 3.2). This is called interdigitated electrode configuration (IDE) and already utilized in DEP microsystems such as chips for particle separation (Kumar et al., 2009; Morganti et al., 2011; Weiss et al., 2009).

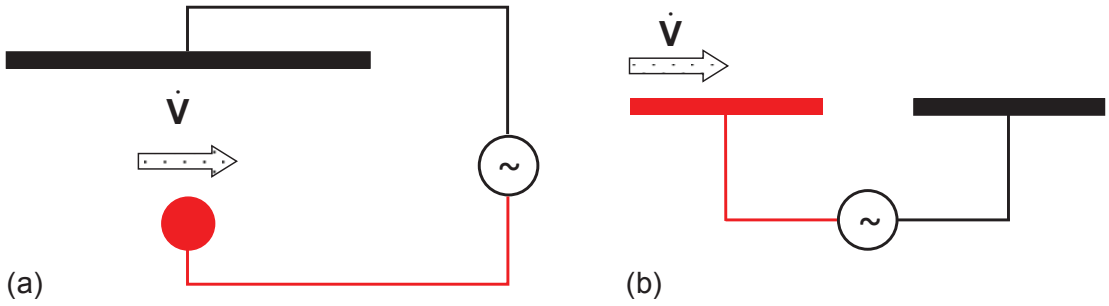

Figure 3.1: Types of DEP electrode configuration: **(a)** orthogonal and **(b)** horizontal to the medium flow ($\dot{V}$) with respect to electrode arrangement.

On the other hand, the increase of fluid flow will require much higher electric field input for generating sufficiently high DEP force to effectively move particles.

An increase of throughput can be achieved by an increase of particle concentration and fluid flow rate. In case of orthogonal electrode configuration, an increase of particle concentration enhances the interaction between particles, which possibly align along the electric field forming a chain-like agglomeration of particles. This pearl-chain effect (Jones, 1995) might intervene in DEP motion and potentially bridge the two electrodes. Such a “short-circuit” between electrodes will increase electrical current and thus energy consumption of the DEP system (Du et al., 2009). In case of large particles forming chains the open cross section area of the channel is reduced and so is the DEP effect due to increased fluid velocity.

To realize a certain gradient of the square of the electric field with an orthogonal electrode configuration, a relatively high voltage is required in comparison to an IDE due to the relative large distance between electrodes. Concurrently, for a certain voltage input in a DEP system, the DEP force can be enhanced cubically by decreasing the distance between electrodes (Eq. (3.1)).

Currently, the IDEs applied in DEP systems are configured with metal plates (either insulated or bare). The disadvantages of such a plate IDE system (Fig. 3.2a) are a very weak electric field at the center of the electrodes and a rapid change of gradient of square of the electric field at positions in the vicinity of electrodes (Cao et al., 2008; Crews et al., 2007). Due to both problems, current plate IDE cannot homogeneously manipulate particle trajectories. For this purpose, a novel design of a horizontal electrode configuration is required, which should provide strong gradient of square of the electric field that is as homogeneously distributed in the vicinity of electrodes array as possible.

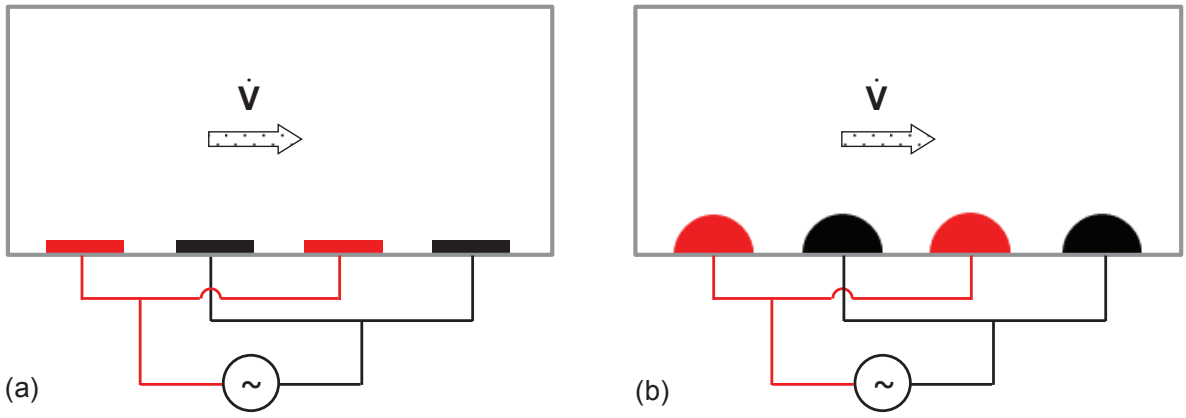

Figure 3.2: Interdigitated electrode arrangement with different electrode shapes: **(a)** traditional plate interdigitated electrode configuration and; **(b)** novel cylindrical interdigitated electrode configuration.

Here a novel design of an IDE configuration is presented that meets the above mentioned requirements by using cylindrical instead of plate electrodes (Fig. 3.2b). The superiorities of this proposed cylindrical IDE structure will be testified by simulating the effect of this decisive modification in terms of the gradient of square of the electric field distribution and hence particle motion and compare with experimental measurements in a DEP cell.

3.2 Experimental particle motion in a cylindrical IDE-DEP cell

3.2.1 IDE-DEP system

The test IDE-DEP system consists of a DEP cell mounted with group of cylindrical IDEs with a fixed ratio of electrode diameter *d* to distance between electrodes *L* (aspect ratio) of *d:L* = 1:2 (Fig. 3.3a). Particles located at the subsurface of medium (suspended in medium), will be repelled from higher electric field region along horizontal direction (*x*) under the influence of n-DEP force (their initial positions as indicated in Fig. 3.3b). Meanwhile, the cycling fluid flow, which is induced electrothermally (ETE) follows the direction of n-DEP force (Fig. 3.3b).

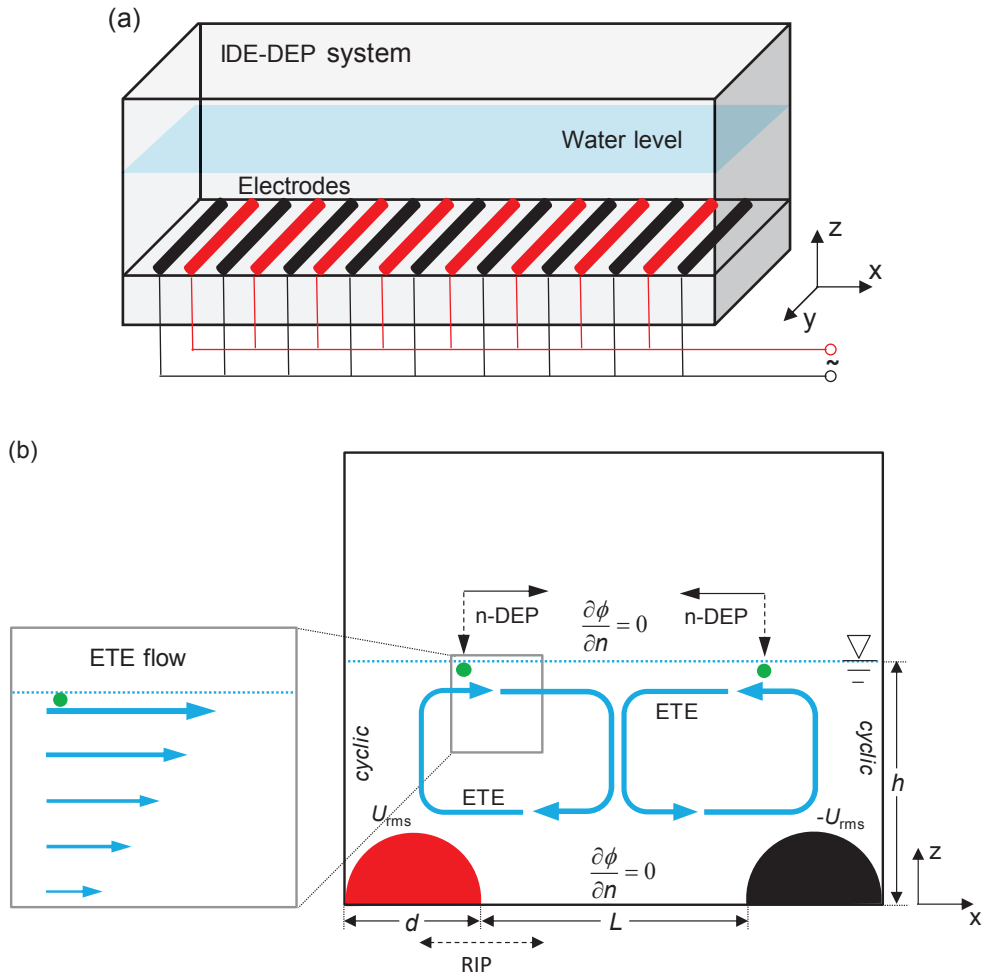

Figure 3.3: (a) Three-dimensional (3D) schematic diagram of the IDE-DEP system with groups of cylindrical IDEs. **(b)** Cutout of the IDE-DEP system showing two electrodes (black solid semi-circles) interdigitatedly installed. Particle (green solid circle) suspending at the subsurface of aqueous medium will be moved to mid between two electrodes when n-DEP effect occurs. In case of n-DEP the fluid flow velocity V_{ETE} (blue arrow lines), which results from electrothermal effect (ETE), enhances particle (located at the subsurface of the liquid medium) motion velocity. The dashed line indicates the region of particle initial positions (RIP) for velocity measurements.

3.2.2 Experimental setup

The experimental setup was composed of a CCD camera (IMAGING SOURCE Co. Ltd DFK 31AU03), a lens (IMAGING SOURCE Co. Ltd), a function generator (VOLTCRAFT® 7202) and a power amplifier (FM1290, FM ELEKTRONIK BERLIN). Groups of electrodes were installed subsequently in a DEP cell (Fig. 3.3), having aspect ratio (a ratio of diameter or length of electrode to distance between electrodes, *d:L*) of 1:2. Titanium wires insulated with rutile were used as electrodes with diameter of 2 mm. Insulation on cylindrical electrodes were applied to diminish problems in conductive aqueous media such as the risk of short circuit and electrochemical reaction. Resin particles (with relative dielectric constant of ε_p = 3) were utilized in the experiment with a mean particle diameter of 808 µm. Demineralized water (with relative dielectric constant of ε_m = 78.5) was used for the suspending medium. By settling heavy resin particles in aqueous suspension, a light fraction of particles was obtained that stuck to the surface of the suspension. These collected particles were used in the dielectrophoresis experiment. Both size and velocity of observed single particles were measured. This was done by analyzing the image of particle captured by optical system (CCD camera and lens) and using *SigmaScan Pro 5.0*, calibrated with standard 500 µm polymer microspheres (Duke Scientific Co. Ltd).

3.2.3 Experimental determination of particle motion

Due to the much lower permittivity of resin particle compared to that of demineralized water, the resin particle suspended at the water surface presents a negative DEP effect, and hence moves toward lower electric field region. The local particle velocity in horizontal direction v_x was obtained by dividing motion distance (Δs_x) by motion time (Δt).

$$v_x = \frac{\Delta s_x}{\Delta t} \tag{3.2}$$

Particle velocities were determined at different heights *h* (2 mm, 2.5 mm, 3 mm, 5 mm and 7 mm) above electrodes. Each experiment was repeated 10 times. The height of particle away from electrodes was varied by controlling the height of demineralized water. After experiment, the recorded video clips were processed by capturing pictures using software of *SigmaScan Pro. 5.0*. The region of particle initial positions (RIP) was defined thereafter, i.e. from electrode center to first quarter of electrode distance (1/2 *d* + 1/4 *L*), as indicated with dotted double-arrow in Fig. 3.3b. The time difference between two captured pictures was chosen as motion time (Δt), in the magnitude of 1/30 s for reducing measurement error at most. The experimental errors were evaluated by comparing the measured particle motion distance to the half of the characteristic length (*L/2*).

3.3 Model and simulation

3.3.1 Particle motion model

As can be seen in Fig. 3.3, the motion of a spherical particle suspending on the subsurface of the aqueous medium could be assumed to be a steady state condition where negative DEP force and viscous drag force are balanced. Neglecting Brownian motion and gravity, the steady state particle velocity can be expressed by Eq. (2.31). In Eq. (2.31), the fluid medium is considered to be static, but this is typically not the case. The electric current causes Joule heating, which in turn leads to a motion of fluid medium induced by temperature gradients (Fig. 3.3), termed as the electrothermal effect. Typically, there are two types of electrothermal flow which dominate in different scale systems. The details of Joule heating induced electrothermal flow have been discussed in Chapter 2. In millimeter systems with electrode distances larger than 1 mm is considered to be buoyancy force dominates where electric force can be neglected. The buoyancy induced flow velocity was given by Eq. (2.56). As a result, the resultant velocity of particle suspending on the subsurface of the medium can be expressed as a combination of Eq. (2.31) and Eq. (2.56):

$$v_{DEP+ETE} = \frac{a^2 \varepsilon_0 \varepsilon_m Re[\tilde{K}]}{3\mu_m} \nabla |\boldsymbol{E}|^2 + U\sqrt{\frac{\alpha_v g {L_c}^3}{Vc_P \mu_m R_s}} \tag{3.3}$$

The second term of Eq. (3.3) represents the ETE influence on fluid flow and thus, due to drag, on particle motion in the millimeter scale (Du et al., 2007). In case of n-DEP, the medium motion increases the velocity of suspended particle.

The model of predicting the disturbance of electrothermal induced fluid motion on particle's DEP motion as described by the second term of Eq. (3.3) was developed and experimentally verified with a millimeter scale concentric annuli electrode configuration by Du et al. (2007). While for a millimeter scale IDE-DEP system, this model is considered to be appropriate for predicting particle motion under maximized ETE influence based on the following assumptions:

1. In millimeter IDE-DEP system, heat convection is large compared to heat diffusion, as calculated the Peclet number using Eq. (2.41) which is Pe > 28 in this case study.
2. The length of channel (5 cm) related to electrical resistance between electrodes (R_s) is taken into account for calculating system energy balance (Eqs. (2.49) and (2.50)).
3. At the characteristic system length (L_c) of the order of 1 mm, buoyancy due to Joule heating always dominates the fluid flow (Arnold and Chapman, 2000; Arnold, 2001;

Castellanos et al., 2003).

By using this model, some additional model assumptions for calculating ETE velocity ion should be emphasized:

1. ETE influence on particle motion depends on ETE velocity which varies spatially (Fig. 3.3b). Maximum ETE influence on particle motion occurs at maximum ETE velocity (v_{ETE}).
2. Maximum ETE velocity (v_{ETE}) appears at the subsurface of the fluid and is considered to be constant during particle motion under stationary conditions.

3.3.2 Numerical simulation

Two cases were investigated: for comparing cylindrical IDE with plate IDE configuration, the distribution of the gradient of square of the electric field was simulated at microscale, in which both the diameter of electrode (*d*) and the distance between electrodes (*L*) are 10 µm in a DEP system with height (*h*) of 50 µm. In another case, to demonstrate the performance potential of cylindrical IDE, simulations were performed at millimetre scale with an aspect ratio of 1:2 (electrode diameter of 2 mm and distance between electrodes of 4 mm).

Simulations were performed by implementing the model into the source code of *OpenFOAM*, an open source software package that uses *CFD* solvers based on the finite volume method. For describing the quasi-electrostatic field, Maxwell's equations were used in the following form (Green et al., 2002):

$$\boldsymbol{E} = -\nabla\phi \tag{3.4}$$

$$\nabla \cdot \boldsymbol{J} + \frac{\partial \rho}{\partial t} = 0 \tag{3.5}$$

$$\nabla \cdot \left(\varepsilon_0 \boldsymbol{E}\right) = \rho \tag{3.6}$$

where ϕ is the electric potential, ρ is the volume charge density and $\boldsymbol{J}$ is the electric current density. For a homogeneous medium with zero charge density in computational domain, Eqs. (3.4), (3.5) and (3.6) can be simplified to Laplace's equation (Morgan and Green, 2003):

$$\nabla^2\phi = 0 \tag{3.7}$$

Both the electric field strength $\boldsymbol{E}$ and the gradient of square of the electric field $\nabla|\boldsymbol{E}|^2$ can be calculated as a function of ϕ (Eq. (3.4)). Simulations were performed for the two-dimensional (2D) plane located at the center line (y = Y/2), as presented in Fig. 3.3b. By this means wall effects and disturbances by the edges of the electrodes can be neglected since the electrodes are long compared to their diameter. Besides, the periodical array of electrodes allows simplification of the whole system using one representing group of electrodes for simulation (Cao et al., 2008). Further, both alternating current (*AC*) input voltage and direct current (*DC*) voltage, equivalent to the root mean squared voltage (U_{rms}) of the *AC* input were applied. The electric potentials on both surfaces of electrodes were given as positive and negative with a value of U_{rms}, respectively. On the left and right sides of model, *cyclic* boundary conditions were set to simulate the presence of an infinite number of electrode groups. For the upper and bottom edges between electrodes, either *Dirichlet* boundary condition ($\phi = 0$) or *Neumann* boundary condition ($\frac{\partial \phi}{\partial n} = 0$, where n donates the external normal vector to the boundary) was used with the assumption that the substrate and the top of the chamber always have much lower conductivity and permittivity than the medium in IDE channel (Green et al., 2002). Based on the *OpenFOAM* simulation results of the gradient of square of the electric field $\nabla|\boldsymbol{E}|^2$, particle velocities were calculated by Eq. (3.3) using *MATLAB*.

3.4 Results

3.4.1 Comparison of cylindrical IDE and plate IDE

The gradient of square of the electric field generated by cylindrical IDE was compared with that of plate IDE (Fig. 3.4). The maximum gradient of square of the electric field of plate IDE (2.16×10^{19} $V^2 \cdot m^{-3}$) at the edges of plates is much higher compared to the maximum value (2.8×10^{16} $V^2 \cdot m^{-3}$) of cylindrical IDE at both sides of the cylindrical electrode in the direction of x axis. Close to the electrodes, the gradient of square of the electric field distribution generated by cylindrical electrodes is almost ideally homogeneous, while the extreme values of the gradient of square of the electric field on the plate IDE surface differ for about 6 orders of magnitude (Fig. 3.5). In addition, the cylindrical IDE has no such areas of very weak gradient of square of the electric field around the electrodes, hence improving much larger effective DEP force field area compared to the plate IDE. Further, the gradient of square of the electric field of plate IDE shows much smaller values than that of cylindrical IDE at the same height of DEP channel. All of these significant improvements from the cylindrical IDE suggest it as promising electrode design for realizing effective DEP effect with lower energy requirement.

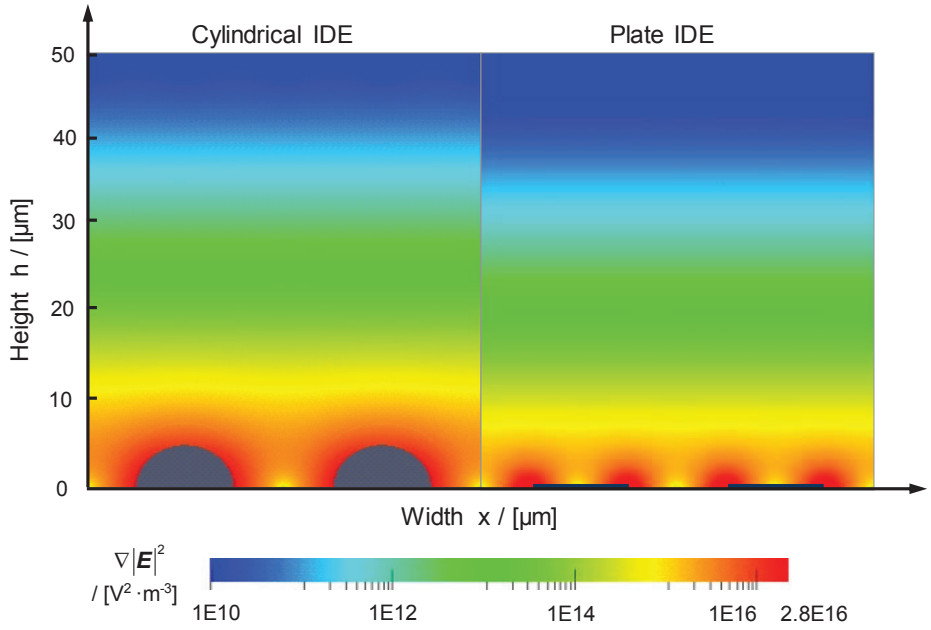

Figure 3.4: Simulation of the gradient of square of the electric field for cylindrical IDE (left) and plate IDE (right). Both the length and diameter of electrodes and the distance between two electrodes were 10 µm (aspect ratio *d:L* = 1:1). The effective voltage applied in this simulation was 1 V_{eff}.

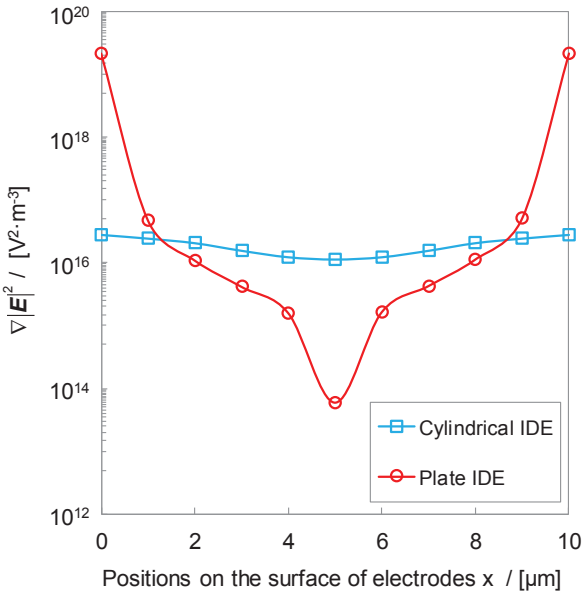

Figure 3.5: The gradient of square of the electric field distribution on the surfaces of both cylindrical (diameter 10 µm) and plate IDEs (width 10 µm).

Models and simulation were validated by comparison with numerical simulation results from literature (Green et al., 2002) for IDE plate electrode with high consistency in the maximal value and distribution of the gradient of square of the electric field. However, the mesh resolution influenced the simulation results, and thereby arising mesh error (Visser et al., 2012). The mesh error becomes more significant at the geometrical spots with maximal and

minimal gradient terms, but negligible at other positions. The solution from the finer mesh was compared with those from the coarser mesh. It is indicated that a large increase of mesh resolution turns out to be a significant enhancement of maximum value of the gradient of square of the electric field. The difference of variety of simulation results at the maximal and minimal spots becomes negligibly small, when the mesh resolution reaches a sufficiently high magnitude, which is considered to be the critical fine mesh resolution allowing accurate simulation.

3.4.2 High-pass-filter effect

For DEP application in polar solvents such as aqueous solutions, short circuits as well as electrochemical reactions (electrode fouling) often occurs at bare electrodes and also a reduction of electric field strength across the aqueous solution due to its high conductivity (Du et al., 2009). In addition, the use of bare electrodes increases risk of human electric shock. Therefore, an insulation coating on metal electrodes is crucial to prevent from the abovementioned problems in an aqueous DEP system (Cummings and Singh, 2003). However, the insulated electrodes together with the conductive aqueous medium generate a high-pass-filter effect (Baune et al., 2008). It can be represented by an electrical circuit as shown in Fig. 3.6. The capacitors, C_{E1} and C_{E2}, formed by dielectric insulation film together with electrodes and aqueous medium, connect in series with parallel connected resistor, R_m, and capacitor, C_m, from aqueous medium.

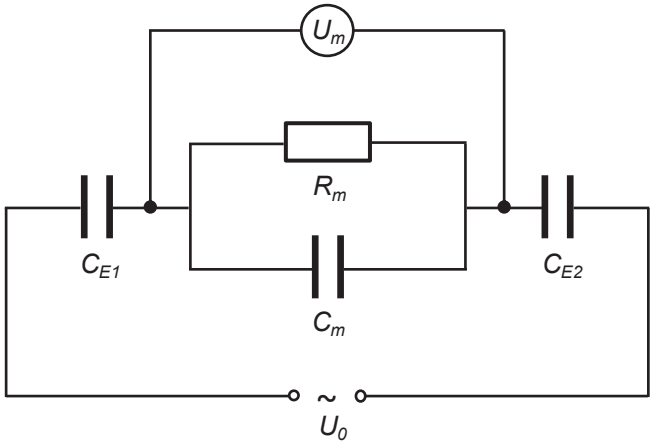

Figure 3.6: Electrical circuit analogy for high-pass-filter effect in an electrode configuration with two electrodes insulated. The dielectric insulation films together with electrode and medium form two capacitors C_{E1} and C_{E2}, while the aqueous medium in the electrode configuration can be represented by paralleled connected resistor R_m and capacitor C_m.

The frequency-dependent voltage fraction, i. e. voltage across the medium U_m relative to applied voltage U_0, can be given (Baune et al., 2008):

$$\frac{U_m}{U_0} = \frac{Z_m}{(Z_{E1} + Z_{E2} + Z_m)} \tag{3.8}$$

where, Z , impedance formed by insulation films and medium with subscripts of *E1*, *E2* and *m*, respectively, can be obtained from,

$$Z_m = \frac{j\omega R_m C_m}{R_m + j\omega R_m C_m} \tag{3.9}$$

$$Z_{E1} = \frac{1}{j\omega C_{E1}} \tag{3.10}$$

$$Z_{E2} = \frac{1}{j\omega C_{E2}} \tag{3.11}$$

In this work, the voltage fraction for electrode configuration with aspect ratio of 1:2 was simulated as shown in Fig. 3.7. The output voltage U_m can be obtained as 121.1 V_{eff}, while the applied voltage is 183.5 V at the frequency of 100 Hz.

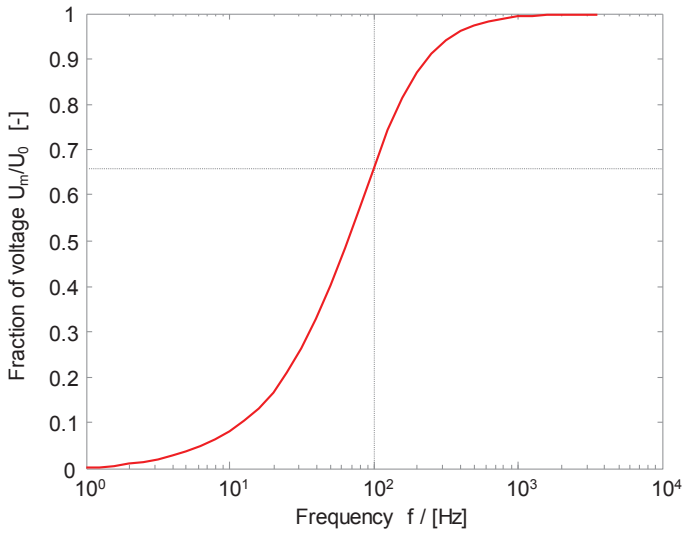

Figure 3.7: Frequency dependence of voltage fraction with aspect ratio (*d:L*) of 1:2. The dashed line indicates the voltage across aqueous medium (electric conductivity of 0.001 S • m^{-1}) among electrode configurations at the frequency of 100 Hz.

3.4.3 Experimental validation

The transformation of magnitude of cylindrical IDE channel from micrometer to millimeter was performed and verified to be reasonable with sufficient accuracy in simulation, by experimental results as shown in Fig. 3.8.

The dependency of DEP effect on the gradient of square of the electric field was experimentally examined by measuring particles motion velocity at different height to the electrodes of a DEP cell and comparing with simulation results. A resin particle suspended at the surface of demineralized water of height *h* in the system was observed to move from an electrode (higher electric field region) to the mid between electrodes (lower electric field region) under isothermal conditions (T = 298.15 K), presenting negative DEP effect, as presented in Fig. 3.3b. With rising temperature gradients, an ETE effect was observed with a flow direction from electrode to the mid between electrodes at the surface of aqueous medium, which in turn increased particles motion velocity. Based on the simulation results of the gradient of square of the electric field in the horizontal direction and using Eq. (3.3), the velocity of resin particle (diameter of 808 μm) was theoretically predicted in steady state (Fig. 3.8). Both simulation results and experimental measurement present well agreement.

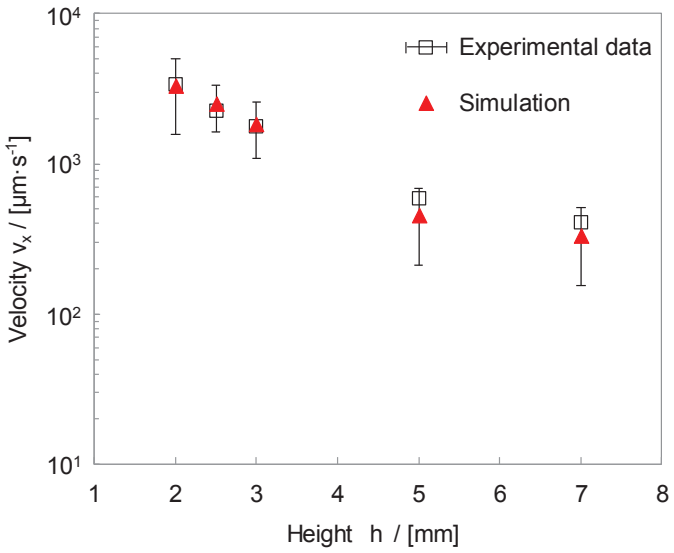

Figure 3.8: Comparison of experimental results of particle velocities and numerical solution using Eq. (3.3) for different distances between particle and IDE (height *h*) with aspect ratio (*d*:*L*) of 1:2. (Experimental data of particle velocity see Appendix A, Table A.1)

3.4.4 Electrothermal effect

The influence of ETE on particle DEP effect can be represented by comparing both velocities induced by DEP and ETE, i.e. a ratio of DEP to ETE velocity. The results simulated (Fig. 3.9) using the identical DEP system in the experiment demonstrated dominant DEP effect, when

the particle is positioned very close to the electrodes (lower height to electrodes), where the gradient of square of the electric field is higher. As an example, the induced DEP velocity at the height of 2 mm to the electrode is about 60 times higher than ETE velocity, as presented in Fig. 3.9. An equivalent height, at which a balanced effect between DEP and ETE is reached, can be obtained. In this DEP system, the equivalent height is about 6 mm. Above this height, ETE is more dominant. Due to the convective fluid flow induced by the ETE, the particles motion will be disturbed and thereby unpredictable. It demonstrates that a working height of DEP force in a certain IDE-DEP system can be predicted and should be taken into account during design of DEP system, for achieving an effective DEP effect while minimizing the influence of ETE effect.

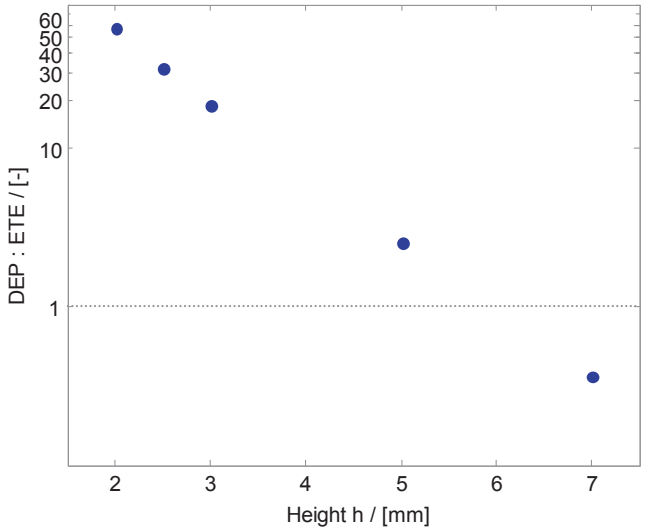

Figure 3.9: Ratio of DEP to ETE velocity at different distances between particle and IDE (height *h*) with aspect ratio (*d:L*) of 1:2.

3.4.5 Performance analysis of different electrode configurations

For studying the impact of electrode configuration to the DEP effect, the DEP velocities of particle at different height (1 mm to 5 mm) to the electrode in three different types of electrode configurations, plate IDE, cylindrical IDE and orthogonal electrode configuration, were simulated as presented in Fig. 3.10. Both plate and cylindrical electrodes have identical aspect ratio 1:2, i.e., diameter or length of electrode is 2 mm with electrodes distanced 4 mm. The distance between electrodes in the orthogonal electrode configuration is 4 mm, while the diameter of smaller spherical electrode is 2 mm with another plate electrode oppositely positioned above it at a distance of 6 mm, as shown in Fig. 3.1 (a). Hence in the case of orthogonal electrode configuration, the maximal height of particle position is the electrodes distance. The variety of DEP velocity as a function of height presents a similar tendency, which

is the decrease of DEP velocity with the increase of height. The cylindrical IDE generates much higher (around 3.3 times to plate IDE and 2.9 times to the orthogonal electrode in average) DEP velocity compared to the others, due to its more inhomogeneous electric field induced by the more non-uniformly structured electrode configuration. The higher particle velocities at high (5 mm) and low (1 mm) heights on orthogonal electrodes as compared to plate IDE can be explained by the high electric field gradient distribution at near electrode region. It hints that the cylindrical IDE could provide similar DEP effect at the same height to the electrodes but requiring much lower voltage input, thereby much lower energy consumption. In addition, the disturbance induced by ETE to the particle DEP motion will be lower at the same height in the cylindrical IDE DEP system compared to the others.

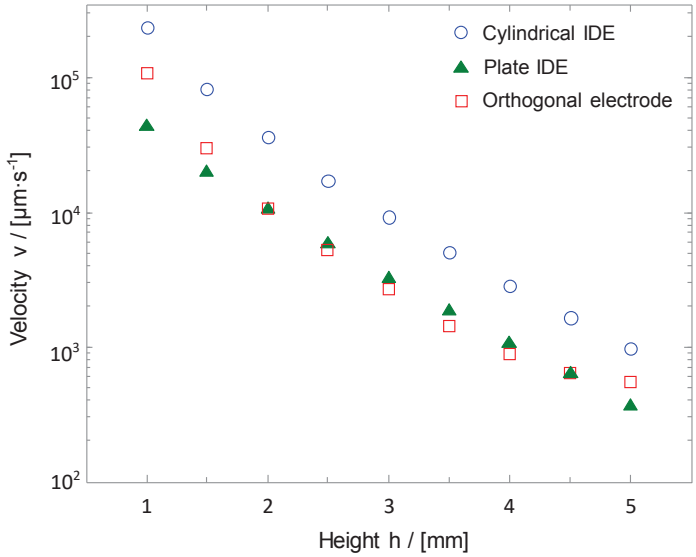

Figure 3.10: Simulation comparison of DEP velocity (logarithm) at different distances between particle and IDE (height *h*) in cylindrical IDE, plate IDE and orthogonal electrode configuration with identical voltage input.

3.5 Discussion

In this chapter, an electrode configuration with interdigitatedly installed cylindrical electrodes is suggested. For the first time the gradient of square of the electric field was simulated for such a system and compared with plate IDE electrode configuration. The simulation results demonstrate that a cylindrical IDE could provide more homogeneously distributed gradient of square of the electric field on the electrode surface and higher gradients of square of the electric field than plate IDE above a certain height to the electrodes.

The velocity of resin particle suspended at the surface of demineralized water in a DEP channel mounted by cylindrical IDEs with aspect ratio (*d:L*) of 1:2 was theoretically simulated

and experimentally measured at different heights of particle to the electrode. In all cases simulations met experimental results within their standard deviations. This good agreement indicates that the simulations can be used for reliable predictions of similar systems.

Fluid flow induced by ETE was observed to influence or even determine particle motion. The impact of characteristic length both on ETE fluid flow speed and voltage across medium was demonstrated. The comparison of DEP and ETE velocity, as presented by a ratio of DEP to ETE, demonstrated that the DEP velocity is dominant at the height of particle position to the electrode below 6 mm in the experimental cylindrical IDE system. The DEP velocities of particle in aqueous medium in cylindrical IDE at different heights of particle position to the electrode were simulated and compared with them in plate IDE and orthogonal electrode configuration. The simulation results demonstrated that the cylindrical IDE could generate more effective DEP effect at identical height compared to the other electrode configurations, and thereby indicating that an identically effective DEP effect with lower energy demand can be expected using cylindrical IDE electrode configuration.

4 Predicting and eliminating Joule heating constraints in large IDE-DEP channels

For scaling up DEP separation, the simplest way to enlarge throughput per unit is to increase the electrode dimensions and electrode distances. However, a DEP system with a large distance between electrodes and, definitely requires high electric potential and accordingly high energy input. This in turn causes unavoidable energy consumption and undesirable thermally induced medium flow by Joule heating disturbing the particle DEP motion, which is a general DEP problem. It is a problem that can be solved in parts by using cylindrical interdigitated electrodes, which were suggested to reduce the energy demand, as discussed in Chapter 3.

The aforementioned general DEP problem raises the question whether an optimal design of DEP channel geometries and electrode arrangement exist for a specific application, which provides optimal distribution of the gradient of square of the electric field and, hence, maximized separation efficiency at minimized energy demand. Obviously it is not possible to outwit physics, in particular the limitations in creating the gradient of square of the electric field. Consequently, these limitations act as constraints when optimizing the trade-off of conflicting requirements, both dielectrophoretic and electrothermal. It can be expected that in continuous separation systems, i.e. with imposed flow, the relative disturbance of DEP particle motion by electrothermal induced fluid motion reduces with volumetric flow rates of the imposed flow. Hence Joule heating disturbances are largest at zero flow rates, i. e. in a batch process which is therefore chosen for a worst case study to demonstrate the possibility of eliminating Joule heating disturbances.

This general problem will be solved here in this chapter, by firstly describing the interplay of channel geometry, size and position and secondly, based on these findings, by identifying optimality. By this means, one would expect that it is possible to avoid Joule heating disturbances in DEP systems even in a worst case, i.e. the batch process.

Parts of this chapter have been published on the Journal "*Chemical Engineering Science"* (Wang et al., 2015).

4.1 Layout of the IDE-DEP system

With respect to the IDE-DEP system, a solely structure parameter of cylindrical IDE, i.e. the aspect ratio (*d: L)* of 1:2 was developed in Chapter 3. However, the impact of variation of

aspect ratio on DEP force field and particle motion was missing. Here in this chapter, a DEP cell is being presented that is mounted with four groups of cylindrical IDEs with four different aspect ratios (*d:L* = 2:1, 1:1, 1:2, and 1:4) (Fig. 4.1). Different from plate IDE, the variation of cylindrical electrode diameter will definitely influence the effective channel height. To avoid this, electrode distance *L* was solely varied which was considered as varies of aspect ratio in this case study.

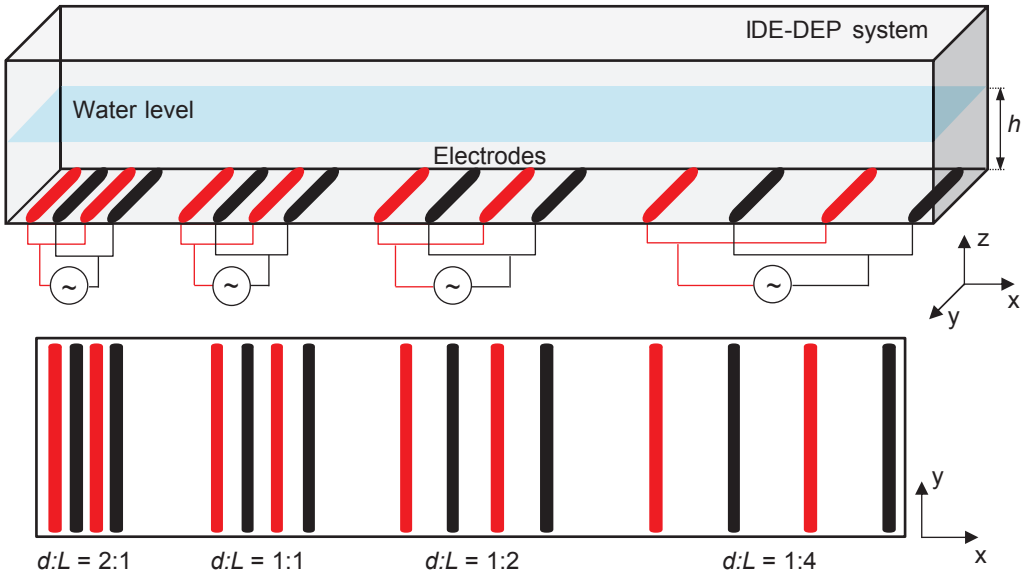

Figure 4.1: Schematic diagram of the IDE-DEP system with four groups of cylindrical IDEs specified by different aspect ratios (*d:L*) as 2:1, 1:1, 1:2 and 1:4, respectively.

4.2 Experimental setup

Except for the IDE-DEP cell as presented above, all the other experimental setup in this chapter are keeping consistent with those used in Chapter 3 (see Section 3.2.2).

Particle velocities were measured at different heights *h* (2 mm, 2.5 mm, 3 mm, 5 mm and 7 mm) above electrodes in four different cylindrical IDEs with different aspect ratios (2:1, 1:1, 1:2, 1:4). The height of particle away from each aspect ratio electrode was determined by controlling the height of water. The experimental particle motion velocity can be determined by using Eq. 3.2 (Chapter 3, Section 3.2.3). Each experiment was repeated 10 times, due to the experimental error.

4.3 Model and simulation

The model of particle motion in the IDE-DEP system was given by Eq. 3.3 with reasonable assumptions (Chapter 3, Section 3.3.1).

For investigating influence of the aspect ratio on the gradient of square of the electric field distribution, simulations were performed in millimeter scales with 2 mm of electrodes diameter (*d*) and 10 mm channel height (*h*). An *OpenFOAM* solver was utilized for solving Laplace's equation Eq. (3.7). Boundary conditions were specified to be the same as those described in Chapter 3 (see Section 3.3.2 and Fig. 3.3b).

Particle velocities of different aspect ratio electrodes were then calculated by *MATLAB* using Eq. 3.3.

4.4 Results

4.4.1 Dependence of the field factor on aspect ratios

The influence of electrode design on the gradient of square of the electric field $\nabla|\boldsymbol{E}|^2$ was simulated for five cylindrical IDE arrays with different aspect ratios. In all cases $\nabla|\boldsymbol{E}|^2$ depend exponentially on channel height *h*. With identical voltage input, i.e. 200 V_{eff}, the distribution of gradient of square of the electric field at positions very close to electrode surface decreases with the decrement of aspect ratio (from 4:1 to 1:4), while the effective working range of $\nabla|\boldsymbol{E}|^2$ enlarges apparently (Fig. 4.2). As an example, if a gradient of square of the electric field of almost $\nabla|\boldsymbol{E}|^2 = 1\times10^{10}$ $V^2\cdot m^{-3}$ is required, the working range in terms of channel height increases from 5 mm to 9 mm for aspect ratios of 4:1 and 1:4 respectively (Fig. 4.3a). This channel height enlargement allows for an 80 % increase of the DEP-system's throughput.

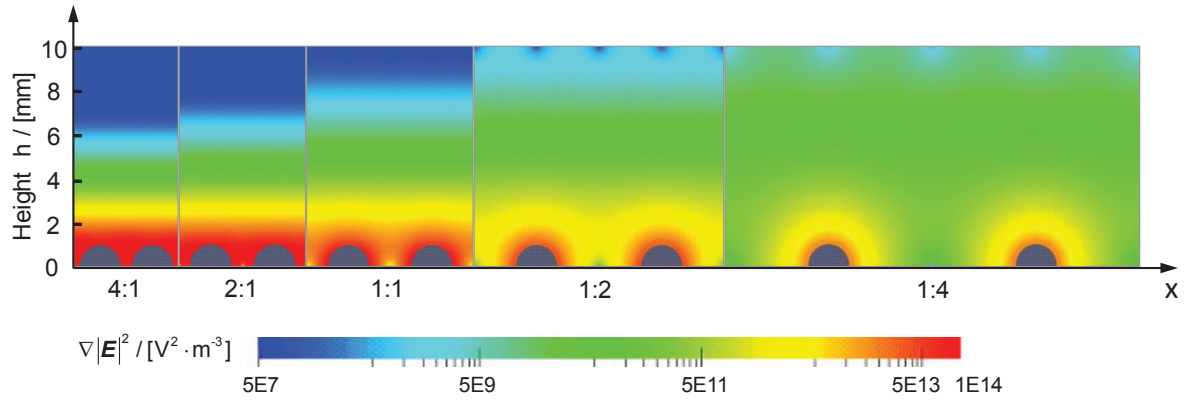

Figure 4.2: Simulated dependency of the gradient of square of the electric field ($\nabla|\boldsymbol{E}|^2$) distribution over channel height on structure parameters for cylindrical IDEs with different aspect ratios.

For all aspect rations calculated, there is the same value of $\nabla|\boldsymbol{E}|^2$ at identical height as illustrated by the intersection of all curves in Fig. 4.3a at a DEP channel height of around 3 mm and an $\nabla|\boldsymbol{E}|^2$ of approximately $1.2\text{x}10^{12}$ $V^2\cdot m^{-3}$.The same fact is also shown by a nearly

horizontal line of $\nabla|\boldsymbol{E}|^2$ as a function of aspect ratio at 3 mm height (Fig. 4.3b), indicating a diminishing dependence of $\nabla|\boldsymbol{E}|^2$ on the aspect ratio at this height. Below this height the $\nabla|\boldsymbol{E}|^2$ decreases with aspect ratio. Reversely, when the height is larger than 3 mm the $\nabla|\boldsymbol{E}|^2$ increases with decreasing aspect ratio.

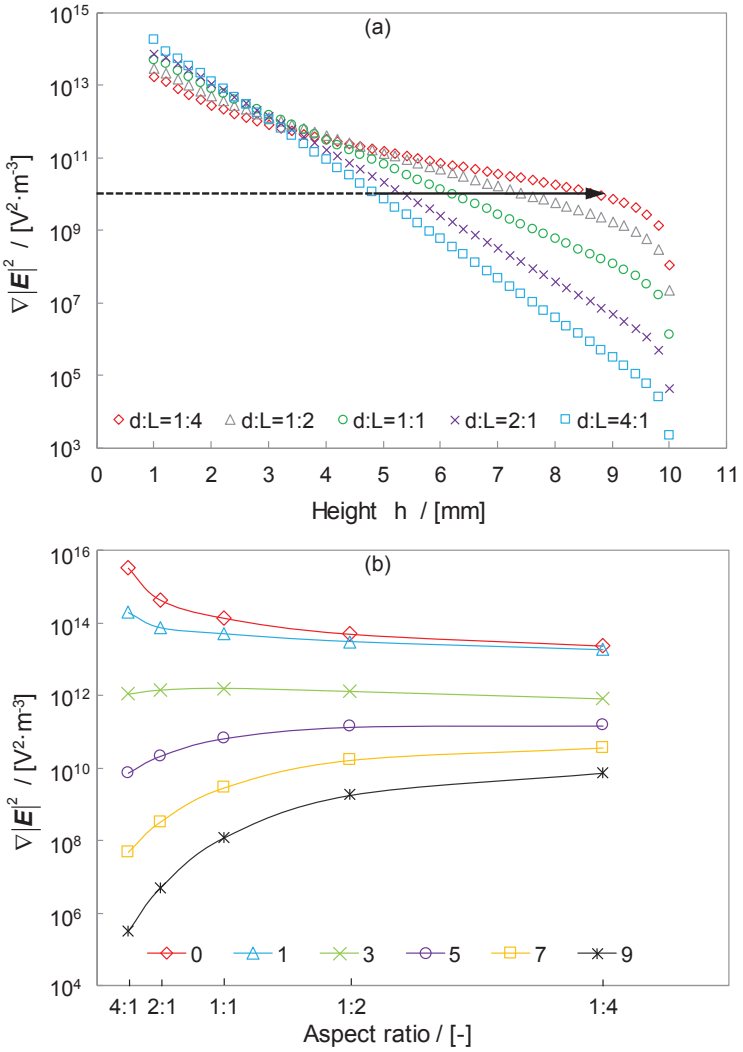

Figure 4.3: (a) Dependence of the gradient of square of the electric field on channel height *h* for aspect ratios of electrode geometries; the arrow indicates the expansion of working range in terms of channel height at chosen $\nabla|\boldsymbol{E}|^2$; **(b)** Influence of aspect ratio of el electrode configuration on $\nabla|\boldsymbol{E}|^2$ at different channel heights.

4.4.2 Experimental particle motion

The application of high voltage at bare metal electrodes in DEP system with aqueous medium induces undesired side effects such as electrochemical reaction. For avoiding this, electrodes need to be insulated. However, the much lower resistance of aqueous medium between electrodes compared to that of insulation material results in a high-pass-filter effect, which was

already discussed in Chapter 3. Besides the dependency of high-pass-filter effect on the dielectric properties and thickness of the insulation film (Baune et al., 2008), It can be found that this effect is also influenced by geometry of electrode configuration, i.e. aspect ratios (Fig. 4.4).

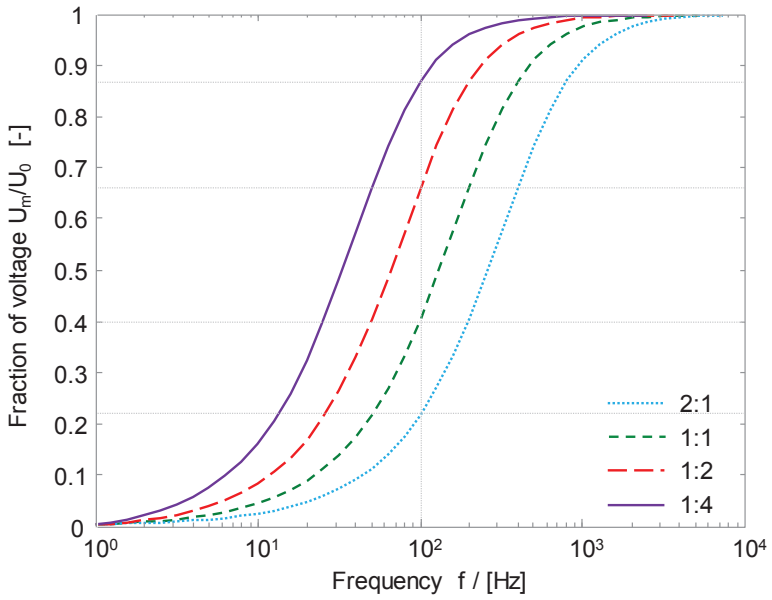

Figure 4.4: Frequency dependence of voltage fraction for different aspect ratios (*d:L*). The intersection of dashed line indicates the difference of voltage across medium among electrode configurations with different aspect ratios at multi- frequencies. Aqueous med medium with the conductivity of 10 µS·cm^{-1}; IDE insulated by 2 µm rutile layer.

The size of electrode *d* together with the distance between electrodes *L* changes the impedances of insulation film on the electrode and the medium between electrodes and thereby resulting in a different high-pass-filter effect, indicated by voltage fraction U_m/U_0. With increasing distance between electrodes at a given frequency also the voltage across aqueous medium U_m increases and, thus, the voltage fraction. For example, at frequency of 100 Hz, the voltage fraction in cylindrical IDE electrode configuration with aspect ratio of 1:4 is about 0.87, while the voltage fraction in the other cylindrical IDEs (1:2, 1:1, 2:1) could only reach 0.66, 0.4, and 0.22, respectively (Fig. 4.4). With an input voltage of 183.5 V_{eff}, the voltages across medium, U_m, generated in all four cylindrical IDE electrode configurations, are 159.6, 121.1, 73.4, and 40.4 V_{eff}, respectively, which were proved by comparing experimentally determined particle velocities with calculated ones and the latter being obtained by using aforementioned effective voltages (Fig. 4.5).

The dependence of the gradient of square of the electric field on the structure parameters was experimentally examined by measuring particle motion velocities in a DEP cell at well-defined

distances between particle and electrodes (height *h*). These results were used for verifying simulation results (Fig. 4.5). A resin particle was observed to move at the subsurface of demineralized water at height *h* from a higher electric field region to a lower electric field region at the mid between electrodes at standard environmental temperature (T = 298 K), presenting negative DEP effect. The temperature gradients within the liquid, which were induced by Joule heating, were shown to be proportional to the square of effective voltage (Eq. (2.53)). With this voltage rising, an ETE was observed inducing a flow direction from electrode to the mid between electrodes that contributed to particles' DEP motion velocity.

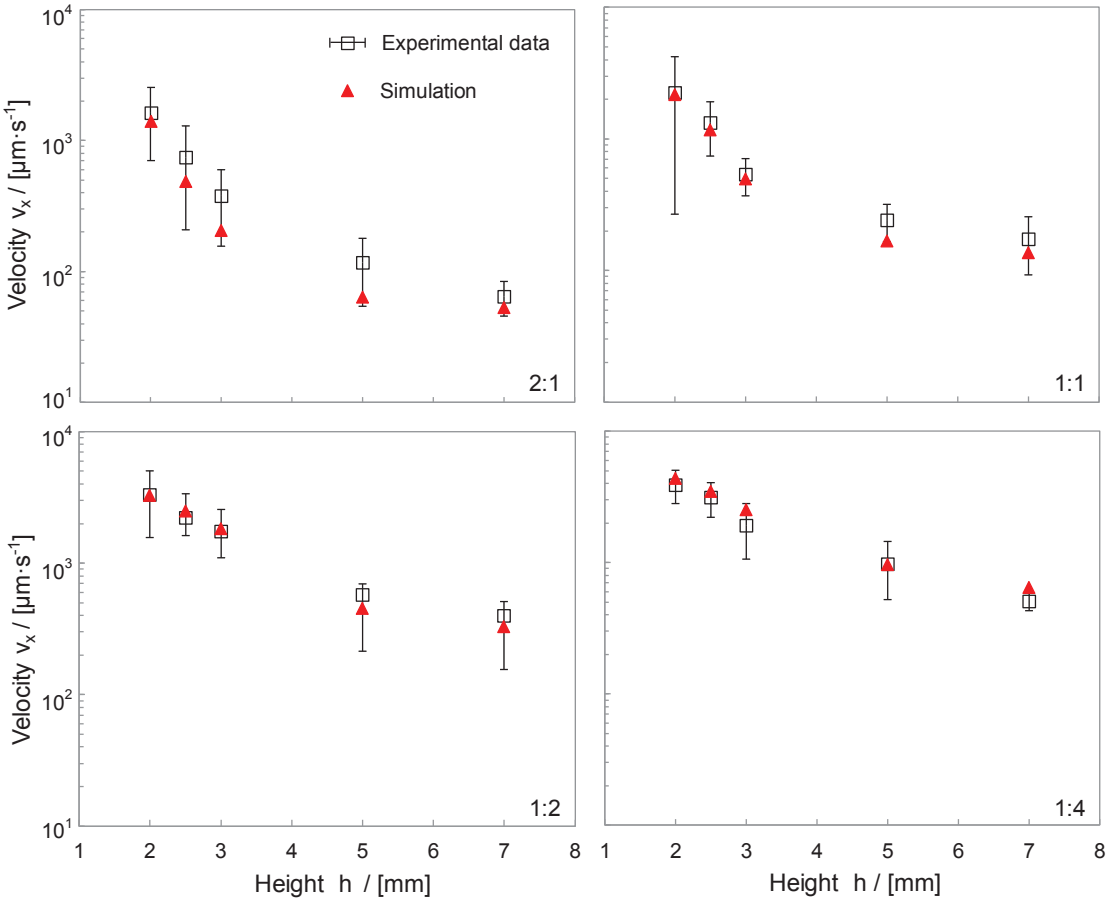

Figure 4.5: Comparison of experimental and numerical net particle velocities (of combined DEP and ETE) for different distances between resin particle and electrodes (height *h*) in a DEP system mounted by cylindrical IDE (Fig. 4.1) with aspect ratio (*d:L*) of **(a)** 2:1**(b)** 1:1, **(c)** 1:2 and **(d)** 1:4, respectively. The voltage input (U_0) is 183.5 V_{eff} with an electric field frequency (f) of 100 Hz. (Experimental data of particle velocity see Appendix A, Table A.1).

Based on calculated horizontal gradient of square of the electric field and using Eq. (3.3), net horizontal velocities of the resin particles were theoretically predicted for steady state. Both predictions and experimental measurements are in good agreement within experimental

standard deviations (Fig. 4.5). For the aspect ratio of 1:1 electrodes as seen Fig. 4.5b, standard deviation was largest at lowest height (2 mm). This can be explained by the fact that $\nabla|\boldsymbol{E}|^2$ varies more strongly in horizontal (x) direction with decreasing height (Fig. 4.6) and so does particle velocity. Further, with the increase of particle-electrode distances (height h), both experimental mean velocities and calculated velocities of particle decrease apparently. In particular, when the height is below a certain value, i.e. 3 mm in case of 2:1 and 1:1 electrodes and 5 mm in case of 1:2 and 1:4 electrodes, the variation of particle velocity exhibits an approximately exponential function tendency.

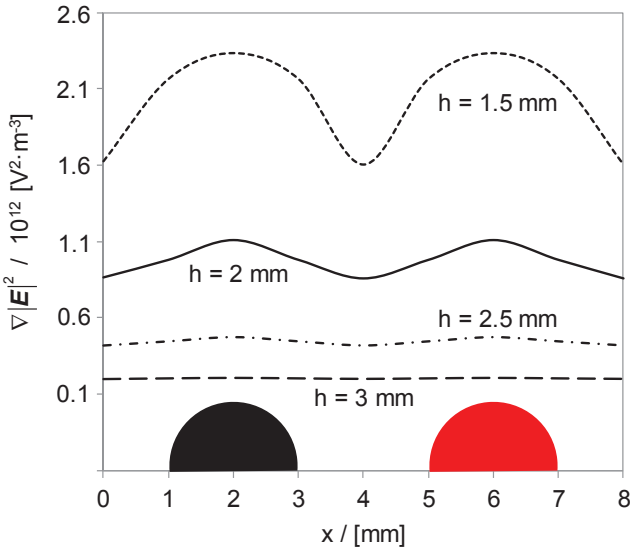

Figure 4.6: Calculated dependence of gradient of square of the electric field $\nabla|\boldsymbol{E}|^2$ on x direction at different heights for aspect ratio of 1:1 electrodes. The voltage across the medium (U_m) is 121.1 Veff with an electric field frequency of 100 Hz.

To further evaluate the accuracy of particle velocity prediction, a correlation of experimentally measured particle mean velocities and predicted values was analysed for four aspect ratios and confirmed good accuracy (Fig. 4.7a). Additionally, relative error between experiment and predicted particle velocity was calculated for different electrode distance (Fig. 4.7b). Obviously, systems of moderate electrode-electrode distances of 2 mm and 4 mm present lower relative error compared with smallest (1 mm) and largest (8 mm) distance of electrodes. The result indicates that predicting ETE disturbance of particle's DEP motion by using Eq. (3.3) is more reliable at moderate conditions, i.e. aspect ratio of 1:1 and 1:2 electrodes. For extreme case such as 1 mm electrodes distance, additional variables should be taken into account for calculating ETE velocity.

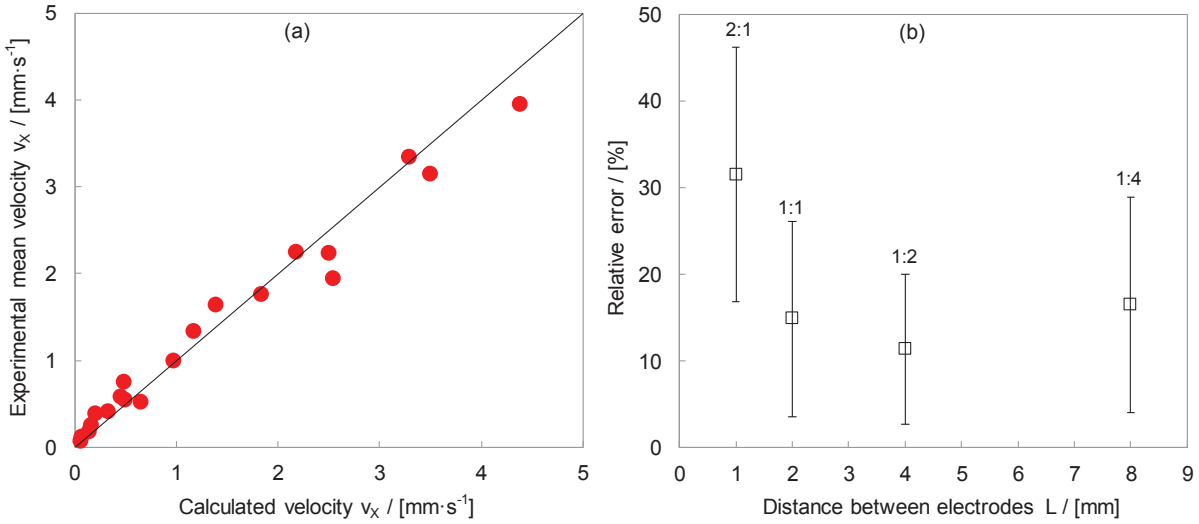

Figure 4.7: (a) Correlation of calculated and experimentally determined particle mean velocities (R^2 = 0.9614); data refer to aspect ratios 2:1, 1:1, 1:2 and 1:4; **(b)** Relative error between experimentally determined and calculated particle velocities in dependence of electrode distance and aspect ratio (*d:L*), n = 10.

4.4.3 Electrothermal disturbances

The significance of DEP on particle motion, which depends on particle height h (determining $\nabla|\boldsymbol{E}|^2$ in first term of Eq. 3.3), was quantitatively described by its ratio to the electrothermally induced medium flow velocity that is determined by the aspect ratio at the power of 1.5 according to second term of Eq. (3.3) (Fig. 4.8). For all DEP systems with aspect ratios from 2:1 to 1:4, DEP contribution to particle motion decreases with electrode-particle distance h. Hence, the highest DEP/ETE ratio (269.1) was obtained at lowest h (2 mm) and for closest distance between electrodes (*d:L* = 2:1), while the lowest ratio (0.014), i.e. highest disturbance of DEP by ETE, was found at 7 mm height. This is due to the fact that the gradient of square of the electric field, which is driving DEP velocity, reduces with cubic of electrode-particle distances h, as depicted by Eq. (3.1)(Pohl, 1978). Interestingly the influence of ETE is lessening with rising aspect ratio for electrode-particle distances h larger than 5 mm. This was observed despite a strong influence of inter-electrode distance L on ETE induced velocity which is proportional to $L^{1.5}$.

At a particle height below 4 mm, DEP effect is dominant for all electrode distances and at least four folds in strength (*d:L*= 1:4) compared to ETE. This demonstrates that, when using an appropriate DEP system, the disturbance induced by ETE could be significantly reduced.

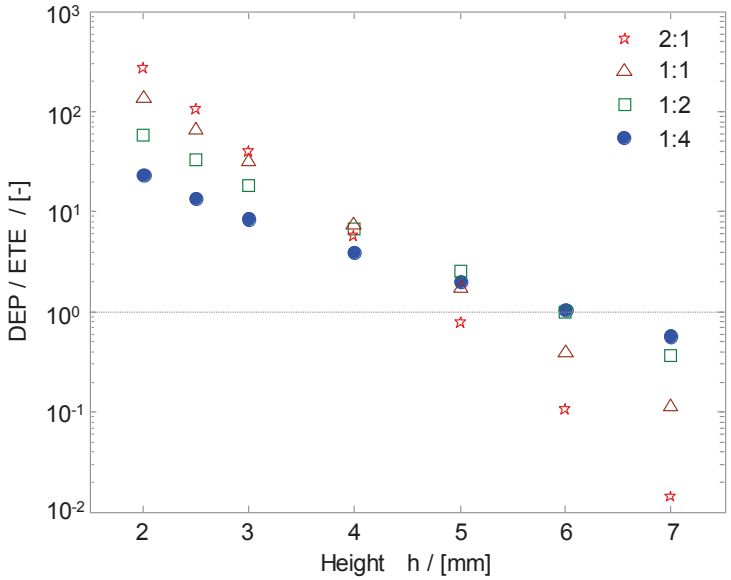

Figure 4.8: Calculated ratios of n-DEP velocity (resin particle) to the ETE velocity as a function of distance of particles and electrodes in the DEP system with different cylindrical IDE configurations (aspect ratios of 2:1, 1:1, 1:2 and 1:4 respectively).

For an IDE-DEP system of millimeter scale, both parameters effective channel height *h* and inter-electrode distance *L* determine performance. Thus, a further dimensionless parameter *L/h* is introduced that controls the performance ratio of DEP to ETE. It was found that this influence decreases with aspect ratio and so does the maximum ratio of DEP to ETE (black chain line in Fig. 4.9).

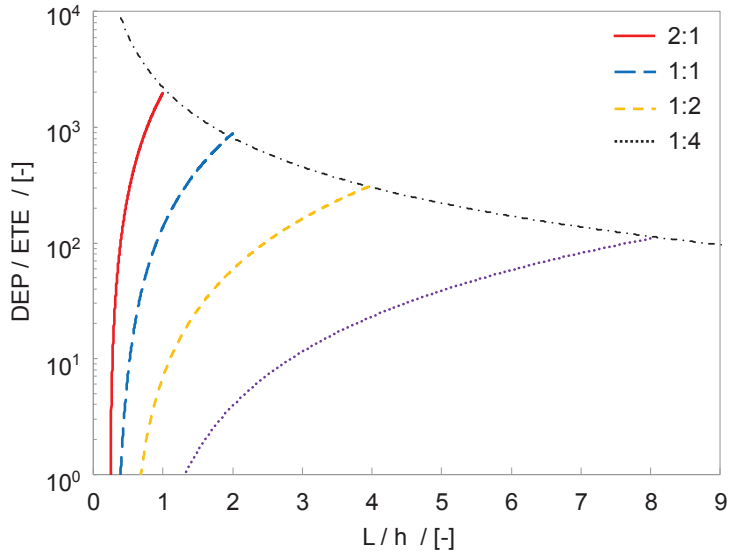

Figure 4.9: Calculated ratios of n-DEP velocity (resin particle) to the ETE velocity as a function of *L/h* with voltage of 121.1 V_{eff} for aspect ratios 2:1, 1:1, 1:2 and 1:4, respectively.

4.4.4 Critical height of IDE-DEP channel

In general, the performance of an IDE-DEP system with channel heights *h* at millimeter scale can be controlled by changing electrode structure parameter, i.e. electrode diameter *d* and electrodes distance *L*. Thus, the ratio of electrode distance to channel height (*L/h*) was proposed to predict the influence of ETE on particles DEP motion in IDE-DEP system. A critical channel height is defined as maximum channel height where DEP velocities are dominant, i.e. 4 mm height for aspect ratio of 1:2 electrodes with 7 folds in strength compare to ETE as indicated in Fig. 4.10. Besides geometry of electrodes, other parameters such as voltage input, particle size and electric properties of suspending medium also influence the design of IDE-DEP system with minimized ETE constraints. Based on particle motion model (Eq. (3.3)), the influences of these parameters on critical channel height h_c are qualitatively shown (Fig. 4.10). The increase of both voltage and particle radius could result in the enlargement of critical height due to the quadratic dependence of DEP velocity on both parameters. With increasing medium conductivity σ_m, more Joule heating is expected and the critical height reduces. It was shown that by this means a tailoring of IDE structure, channel geometries and system parameters allows for achieving maximum DEP velocities with minimized ETE disturbance in a batch system and, thus, in continuous systems as well.

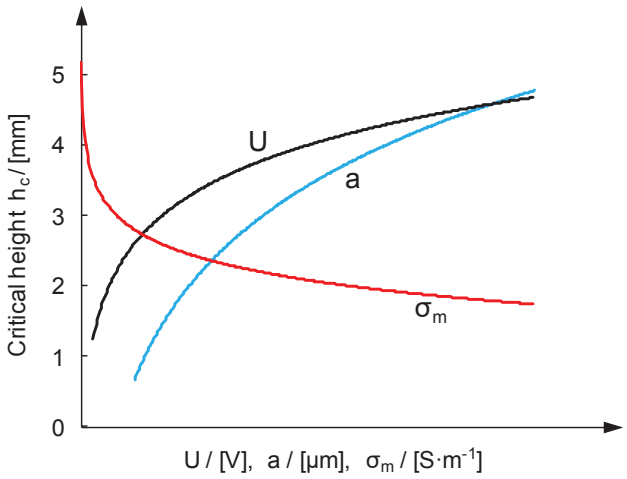

Figure 4.10: Sensitivity of voltage (*U*), particle radius (*a*) and medium conductivity (σ_m) for the impact of these parameters on predicted critical height of DEP channel.

4.5 Discussion

In this chapter, the impact of structure parameters of cylindrical IDE to the DEP effect was numerically and experimentally studied. The simulation of gradient of square of the electric field performed for cylindrical interdigitated electrode configuration with different aspect ratios(*d:L*) demonstrated that the trade-off between effective working range, DEP driving force and electrothermal interference of DEP induced particle trajectories can be solved by

identifying the ideal aspect ratio and channel height. Exemplarily an 80 % increase of DEP-system's volume and, thus, possible throughput was shown for identical electrode length. Interestingly the influence of the aspect ratio on the gradient of square of the electric field is not intuitive as it changes at certain height of channel. Above this height (3 mm in the case study) the gradient of square of the electric field increases with the decrease of aspect ratios, and vice versa.

The experimental micro-particle velocities showed good agreement with calculations; in nearly all cases deviations were smaller than standard deviations. This allows for numerically predicting particle's DEP motion as well as to quantify the undesired ETE. For certain parameters this effect was observed to influence or even determine the particle motion. The results demonstrate that channel height is key for proper separation. For example, in the case study the height of the continuous DEP separator should not exceed 4 mm. On the contrary, when the particle height is beyond a certain value (here: above 6 mm), the undesired ETE becomes predominant and controls the particle velocity.

A qualitative sensitivity analysis was done for the impact of voltage input, particle size and medium properties on the critical design parameter. From this, design criteria were deduced for the IDE-DEP system that allow for minimizing the influence of Joule heating. The findings demonstrate that, even if high voltages are applied, Joule heating problems can be effectively suppressed in DEP system scale-up.

5 Microparticle trajectories in a high-throughput separator for contact-free fractionation by dielectrophoresis

For effective dielectrophoretic microparitcle separation, it is essential to establish a continuous flow system which allows operation to be possible at high-throughput. In addition, an improved understanding of both dielectrophoretic and hydrodynamic behavior of particles, i.e., study the motion trajectories of microparticles in a continuous DEP field-flow system, helps us to better manipulate particles and hence to achieve controllable, accurate and contact-free fractionation. With respect to the design of a continuous dielectrophoretic flow system, a tailored electrode arrangement for providing appropriate DEP force on particles is required. As the most commonly utilized electrode configuration, the interdigitated electrode (IDE) structure has shown its priority in variety of DEP based applications. In particular, the independence of the channel height on the space between electrodes of such an array gives the opportunity to scale up the DEP separation channel. It was reported in Chapter 3 that cylindrical structured IDE (cIDE) configurations present more homogeneously distributed gradients of square of the electric field in the vicinity of the electrodes compared to the traditional plate structured IDE configuration. The homogeneously distributed gradient of square of the electric field in an IDE-DEP system results in a more effective and sustained DEP force field for particle manipulation. Subsequently, a tailored design of such cIDE structures was discussed in Chapter 4. The dependence of the gradient of square of the electric field distribution on its structure parameter, the space between electrodes *L*, was numerically investigated and experimentally evaluated. The results show that DEP systems in which the electrode spacing exceeds the electrode diameter provide a comparably small DEP force close to the electrode surface, while simultaneously the effective DEP working range, i.e., possible channel size, is enlarged. This lays the foundation for designing a high-throughput DEP based device.

In this chapter, a continuous cIDE separator for contact-free size-based microparticle fractionation is suggested. Dielectrophoretic force scales with the volume of the particle, which makes it very suitable for size fractionation. A combined model based on a modified Lagrangian particle tracking solver that calculates the force fields according to Laplace's equation and the Navier-Stokes equation will be established and experimentally validated by measuring motion trajectories of polystyrene microparticles (45, 25, and 11 μm in diameter) in a fluid flow and electric field of a tailored cIDE separator. Using this as a basis, numerical studies will be conducted to evaluate the fractionation performance as a function of operation and design parameters.

Parts of this chapter have been published on the Journal "*Chemical Engineering Science*" (Wang et al., 2016).

5.1 Layout of the cIDE separator

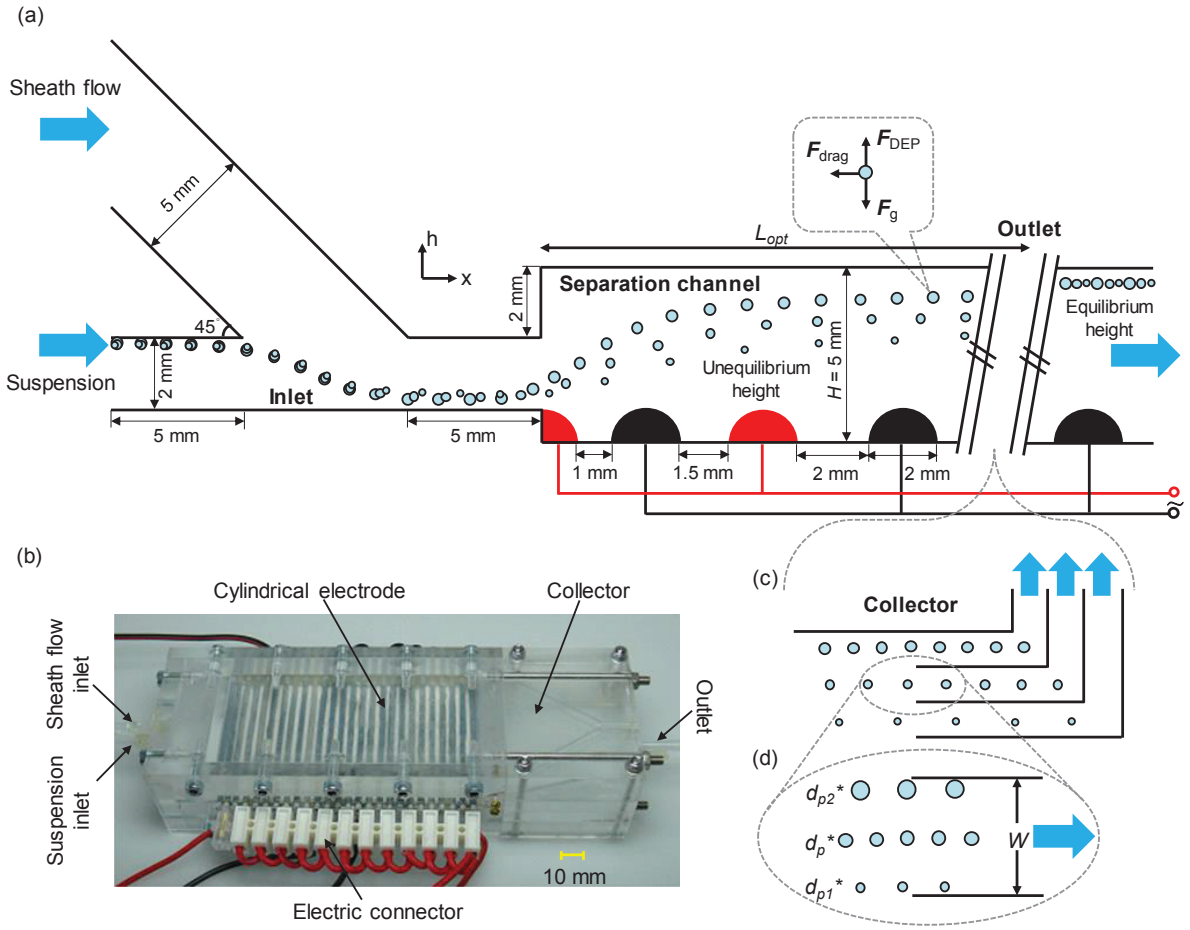

Figure 5.1: (a) Two-dimensional (2D) schematic diagram (side view) of the cIDE separator of channel height H and hydrodynamic particle motion trajectories. Gravity points from top to bottom; **(b)** Experimental setup of the cIDE separator composed of 26 cylindrical electrodes with diameter of 2 mm and electrode length of 50 mm; **(c)** Schematic representation (part view) of the particle collector. Particle trajectories determine optimal channel length L_{opt}, at which the collector (comprising n single collector channels of width $W = H/n$) is best positioned; **(d)** Single collector used for obtaining the target fraction with mean particle size d_p^*. The resolution is determined by the smallest particle size (d_{p1}^*) and the biggest particle size (d_{p2}^*) entering the single collector channel.

The proposed cIDE separator (Fig. 5.1a) consists of two inlet channels (left), a particle separation channel (middle) and an outlet channel (right). The two inlet channels are a 2 mm wide suspension flow inlet and a 5 mm wide sheath flow inlet with 45-degree deflection in between. The sheath flow channel design is based on the idea of maximizing the initial DEP

force by driving the particle motion as close as possible to the surface of the first electrode, where the gradient of square of the electric field is highest. The separation channel consists of an interdigitated array of 2 mm diameter cylindrical electrodes. The electrodes generate a highly inhomogeneous electric field with maximum field strength very close to the electrodes. Particles experiencing negative DEP will therefore be repelled from the electrode surface. The first four electrodes are arranged with increasing distance between them, i.e., 1 mm, 1.5 mm and 2 mm. All other electrodes have a constant 2 mm tip-to-tip distance. The collector at the end of the separator is subdivided into *n* single collector channels (Fig. 5.1c). Each collector channel is utilized for collecting particles of certain size fraction (e.g. d_p^*, d_{p1}^* *and* d_{p2}^*) (Fig. 5.1d). For the separator a channel height *H* of 5 mm was chosen, which presents a good trade-off between channel height and low disturbance of the DEP induced particle motion by Joule heating, as those discussed in Chapter 4.

The particles that are injected at the top position of the suspension inlet are forced by the sheath flow towards the channel bottom. Consequently, they enter the separation channel at the bottommost position very close to the surface of the first electrode, where the DEP force is the strongest. The narrowest spacing between the first pair of electrodes can generate the strongest DEP force in the vicinity of them, allowing a fast levitation due to the negative DEP effect (Wang et al., 2015).

With increasing height above the electrodes, both the field strength and the field gradient are decreasing. Particles experiencing negative DEP should be levitated depending on their diameter. It can be expected that the resulting difference in levitation height is remarkable due to the cubic dependence of the DEP force on the particle diameter. Controlled by the diameter, particles will reach their final equilibrium height (at which the DEP force matches the gravitational body force) at a different time (Mathew et al., 2015). It is important to distinguish the proposed fractionation method from DEP-FFF, in which particles are fractionated according to their dielectric properties at equilibrium conditions (Huang et al., 1997; Leu and Weng, 2009; Wang et al., 1998). A size dependent separation can be achieved only during the transient state before this equilibrium is reached. Hence, the latter electrodes are spaced wider to provide a larger DEP working area, insuring sustainable and effective DEP particle levitation throughout the whole separation process (Wang et al., 2015).

5.2 Numerical simulation

5.2.1 Particle motion analysis

Particle motion trajectories within the cIDE separator were predicted by implementing a modified Lagrangian particle tracking code (Kang et al., 2006) in *OpenFOAM* (original source code of the *OpenFOAM* solvers see Appendix B) using the following simplifications:

1. The influence of the particles on both fluid flow and electrical field were neglected, since the particles are much smaller than the electrode spacing (Kang et al., 2006).
2. The effect of Brownian motion was ignored, as particles are larger than 1 μm (Kissa, 1999).
3. Electrostatic and dielectrophoretic interactions between particles are not considered due to the low input suspension concentration (chosen to enable observation of single particle motion trajectories).
4. Wall effects are negligible with the assumption that particles are always far from either side of the channel wall.
5. Any thermal effect induced by Joule heating on both particles and fluid medium is not considered due to the negligible temperature rise of ΔT below 0.5 K (detailed temperature rise evaluation see Section 5.4.5).

Therefore, the motion of particles is controlled only by a negative DEP force ($\boldsymbol{F}_{DEP}$), a viscous drag force ($\boldsymbol{F}_{drag}$) and a gravitational body force ($\boldsymbol{F}_{g}$), as illustrated in Fig. 5.1a.

Based on model simplification No.1, particle is considered as a point dipole and hence the negative DEP force for the spherical particles can be determined by Eq. (2.17). With the presence of fluid flow, a hydrodynamic drag force acts on the spherical particles. At laminar flow with low particle Reynolds number limit, the calculated Re_p is smaller than 0.1 (Eq. (2.23)) in this case, which is referred to as the Stokes drag. Hence the drag force can be expressed by Eq. (2.24). The gravitational force for the spherical microparticle with mass density ρ_p suspended in a fluid medium with mass density ρ_m is given by Eq. (2.20).

As mentioned above, three forces are acting on the particle in the separation channel, i.e., gravitational force, viscous drag force and DEP force. Since the particle acceleration time scale is much smaller than the residence time, we can neglect inertia and assume that the particle velocity is only a function of the spatial position. The force balance is then given in vector notation by:

$$\boldsymbol{F}_{DEP} + \boldsymbol{F}_{drag} + \boldsymbol{F}_{g} = 0 \tag{5.1}$$

The force field acting on a particle with known properties is given in the entire separator domain. The velocity and subsequently the trajectory of a particle can thus be easily obtained by employing a suitable tracking algorithm and by solving Eq. (5.1).

Since the DEP force decreases with height above the electrodes, the particles will eventually reach a steady equilibrium levitation height, at which the DEP force balances with gravity and the vertical component of $\boldsymbol{F}_{drag}$ in Eq. (5.1) is zero. This height is independent of particle size if equilibrium is reached (Markx et al., 1997; Mathew et al., 2015), while the time for particles to ascend and reach their equilibrium height is size dependent and usually takes several minutes. For the 45 μm particle in our case study, for example, it takes about 3 min from entering the separation channel (h =1.3 mm) to reaching the final equilibrium height (h = 4.5 mm). Due to the cubic dependence of the DEP force on the particle radius a, particles will ascend at different velocities depending on their size before reaching the equilibrium height, i.e., bigger particles will ascend with higher velocities than smaller particles. Eventually, fractionation can be achieved by extracting the particles during their transient ascend before the equilibrium is reached.

5.2.2 Electric field and flow field calculation

The electric field can be determined by solving Laplace's equation (Eq. (3.7)) for the electric potential ϕ. The value of the gradient of square of the electric field ($\nabla|\boldsymbol{E}|^2$) can be evaluated as a function of ϕ. *OpenFOAM* was used to calculate the distribution of $\nabla|\boldsymbol{E}|^2$ within the DEP separation channel. The simulation domain was considered to be two-dimensional since the electrodes are long compared to their diameter (Green et al., 2002). *Dirichlet* boundary conditions ($\phi = \pm U_{rms}$) where applied at the electrode surface to match the *AC* input signal (Crews et al., 2007). *Neumann* boundary conditions ($\frac{\partial \phi}{\partial n} = 0$) where applied at the channel inlets and the channel wall (Lewpiriyawong et al., 2010). A *cyclic* boundary condition was applied at the right side for simulating the presence of an arbitrary number of electrodes (Cao et al., 2008).

The flow field of an incompressible, Newtonian fluid is calculated by solving the continuity equation together with the Navier-Stokes equation, as presented by Eqs. (2.34) and (2.35). In this case, the Joule heating induced thermal effect was assumed to be negligible (model simplification No. 5), and no other external forces act on the fluid, hence the total force $\boldsymbol{f}_{tot}$ in Eq. (2.35) is considered to be zero. The steady state Navier-Stokes equation (Eq. (2.35)) then becomes (Çetin et al., 2009):

$$\rho_m(\boldsymbol{u}_m \cdot \nabla)\boldsymbol{u}_m = -\nabla \boldsymbol{p} + \mu_m \nabla^2 \boldsymbol{u}_m \tag{5.2}$$

Here the non-slip velocity boundary conditions were assigned on the channel wall and each electrode, whereas uniform values of velocity were specified at both channel inlets

corresponding to the experimental volumetric flow rates of the fluid. While pressure is equal in inlets and the right side.

To ensure stable solutions of both fields calculation, the dependence of the field distribution on mesh resolution was evaluated in the computational domain.

5.3 Experimental setup

The setup included a CCD camera (DFK 31AU03, IMAGING SOURCE Co. Ltd), a confocal telelens (IMAGING SOURCE Co. Ltd), a function generator (VOLTCRAFT ® 7202), a power amplifier (FM1290, FM ELEKTRONIK BERLIN), a peristaltic pump (REGLO ANALOG MS-216, LsmaTec Co. Ltd), a syringe pump (LEGATO 270, WORLD PRECISION INSTUMENTS INC.), a cooling system (SITUS Technicals Ltd.) and a cIDE-DEP cross-flow channel (Fig. 5.1c) equipped with cylindrical IDEs. Conventional mechanical processes such as precision milling were utilized for fabrication of the millimeter scale device and for controlling the distance between electrodes. Electrodes were made of titanium insulated by rutile for diminishing problems in conductive aqueous media such as the risk of short circuit and electrochemical reaction, as discussed in Chapter 3. A cooling system composed of two Peltier elements (input 12 V, 10 A, controlled by a Peltier controller with an NTC thermal sensor) were mounted under the electrodes to dissipate any heat generated by the current. Non-functionalized polystyrene microsphere (PS) particles (Polysciences, Inc., ε_p = 2.55, ρ_p = 1005 kg·m^{-3}) with diameters of 45 μm, 25 μm, and 11 μm were utilized in the experiment.

The original microparticle suspensions contain slight anionic surface charge and minimal surfactants during manufacturing process and the final preparation as indicated by the particles provider. To keep a minimized impact of the surface charge on particles' DEP effect, all the experimental particles were pretreated. Two steps of pretreatment were conducted: particles were washed three times with 0.1 mol·L^{-1} sodium chloride solution for removing residual surfactants and thereby reducing their surface charges (Bettelheim et al., 2012); afterwards, these particles were rewashed three times with Milli-Q water (Milli-Q®, σ_m = 5.5×10^{-6} S·m^{-1}, ε_m = 78.5, ρ_m = 1000 kg·m^{-3}). After the pretreatment, the particles were resuspended in Milli-Q water and tested in a batch DEP setup mounted with IDE electrodes. All pretreated particles presented strong n-DEP effect.

For examining the effectiveness of pretreatment, zeta potential of three different sized particles were measured using a *Beckman Coulter Delsa^{TM} Nano C* (Beckman Coulter, Krefeld, Germany) that features a diode laser (30 mW, λ_0 = 658 nm). The zeta potential measurements were carried at scattering angle 15° and the scattered light was detected using a photo

multiplier tube and analyzed with a digital correlator. A sample volume of 5 mL was filled in a *Flow Cell* and equilibrated at T = 298.15 K for 1 min before the measurement time of 3 x 140 s. The correlation function is recorded at 5 positions in the flow channel to correct for the electro-osmotic flow profile. For the evaluation the Smoluchowsky equation and the properties of pure water were used (refractive indices n (658 nm, 298.15 K) = 1.3328, μ_m (298.15 K) = 0.8878 cP, ε_m = 78.3 as given by the Beckman Coulter software). Measurement was considered valid in case the mobility profile gave a parabolic shape expected from electrophoretic light scattering theory (Xu, 2001).

The syringe pump and peristaltic pump were employed for providing suspension and sheath flow identical to those used in simulation, respectively. The input voltage is 200 V_{eff} with a frequency of 200 kHz. The optical system consisting of a *CCD* camera equipped with a telelens was applied to observe and record the particle motion trajectories in the region of the first pair of electrodes. The particle trajectories were recorded as a digital video clip and processed using *Sigmascan Pro 5.0* by defining particle positions (x, h) on every picture extracted at each 1/30 second. Both the horizontal position x and the height of particle h were determined by comparing to the reference objects included in each picture. To minimize the experimental error, trajectories of ten individual particles of the same size were recorded and averaged.

5.4 Results

5.4.1 Electric field gradient simulation

The calculated $\nabla|\boldsymbol{E}|^2$ distribution within the DEP separation channel shows that the highest value of the $\nabla|\boldsymbol{E}|^2$ is found at both sides of the electrodes where the distance between the electrodes is closest (Fig. 5.2a). With increasing height above the electrodes, the $\nabla|\boldsymbol{E}|^2$ value decreases. As expected, electrodes with closer spacing, i.e., the first pair electrodes on the left side with 1 mm space in between, generate higher $\nabla|\boldsymbol{E}|^2$ at positions very close to the electrode surface compared to those with 1.5 mm and 2 mm spacing. In particular, the maximum $\nabla|\boldsymbol{E}|^2$ and thus strongest DEP force appears at the top position of the first electrode, which is caused by the quarter circle geometry of the first electrode (see Fig. 5.1a) and by the material interface between the electrode and the channel wall (Pesch et al., 2015). It is important to note that the solution is incorrect in regions very closed to the electrode edge (Green et al., 2002; Wang et al., 1996), i.e., maximum value of the $\nabla|\boldsymbol{E}|^2$. This numerical

error, however, does not affect particles since the particle focus region is always away from the electrodes (detailed discussion see Section 5.4.4).

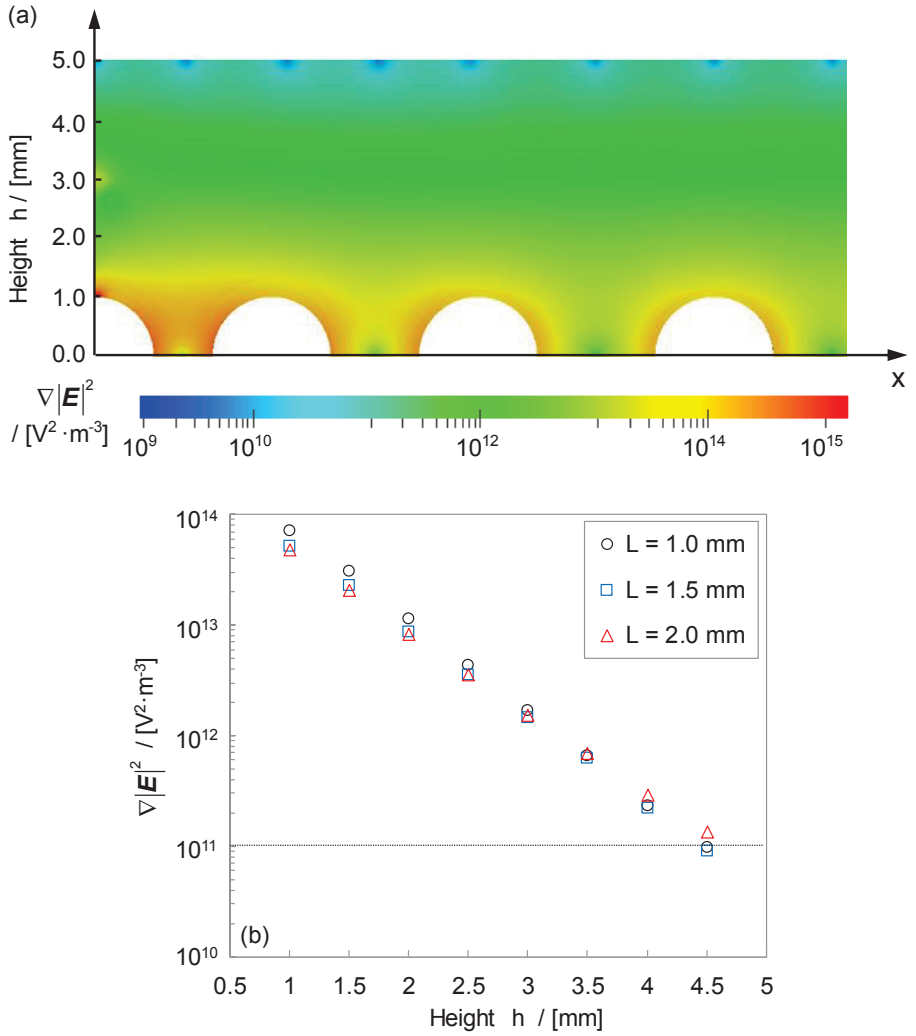

Figure 5.2: (a) Calculated distribution of the gradient of square of the electric field in the initial part of the DEP channel; distances (*L*) between electrodes were 1 mm, 1.5 mm and 2 mm, respectively, voltage input was 200 V_{eff}; **(b)** Dependence of $\nabla|\boldsymbol{E}|^2$ on height for three *d* = 2 mm electrode arrays with different spacing *L*. Dashed line indicates $\nabla|\boldsymbol{E}|^2$ value at which DEP force and gravitational force are balanced.

The dependence of $\nabla|\boldsymbol{E}|^2$ on height was evaluated for electrodes with different spaces (Fig. 5.2b). Closer spaced electrodes show steeper drop of $\nabla|\boldsymbol{E}|^2$ with height compared to wider spaced electrodes. The curves intersect at a height of approximately 3 mm, presenting a similar $\nabla|\boldsymbol{E}|^2$ value of about 1.54x10^{12} V^2·m^{-3}. Below this height, 1 mm spaced electrodes show higher $\nabla|\boldsymbol{E}|^2$ value than the other electrode spacings, and vice versa. The minimum $\nabla|\boldsymbol{E}|^2$ for balancing n-DEP ($Re[\tilde{K}]$ is specified as -0.48 at the frequency of 200 kHz, detailed discussion of $Re[\tilde{K}]$ see Section 5.4.2) and gravitation in vertical direction in this case was

calculated to be $1x10^{11}$ $V^2 \cdot m^{-3}$. In this particular setup, only the 2 mm spaced electrodes provide this value or higher (given as dashed line in Fig. 5.2b) up to height of 4.5 mm (channel height 5 mm). They thus provide a larger vertical DEP working area than the other electrode spacings. The tailored electrode arrangement, i.e., increasing electrode spacing as used in the present cIDE separator, combines both a strong DEP force field at the first electrodes and a more effective DEP working area at latter electrodes.

5.4.2 Evaluation of the Clausius-Mossotti factor

The 45 µm, 25 µm, and 11 µm polystyrene particles utilized in the experimental were pretreated for reducing residual surfactants and surface charges. Zeta potential of three different size particles was measured before and after pretreatment, respectively (Tab. 5.1). As shown in Tab. 5.1, a significant drop of zeta potential was found for 45 µm particle after washing step, while slight decrease and even slight, non-significant increase of zeta potential can be seen for 25 µm and 11 µm particles, respectively. The result indicates a partial surface charge removal due to the washing step.

Table 5.1: The measured zeta potential (ζ) of 45 µm, 25 µm and 11 µm polystyrene particles before (Original sample) and after washing step (Pretreated sample). *s.d.* indicates the standard deviation.

Particle diameter	Original sample			Pretreated sample		
(µm)	ζ (mV)	*s.d.* (mV)	pH (-)	ζ (mV)	*s.d.* (mV)	pH (-)
11	-10.70	0.84	6.9	-13.98	2.16	6.8
25	-22.57	1.99	6.8	-17.85	7.54	6.8
45	-33.01	2.92	7.0	-2.55	0.56	6.9

The conductivities of the pretreated particles was evaluated thereafter using Eq. (2.10) which is based on double layer conductance approximation (Ermolina and Morgan, 2005), given as σ_p (45 µm) = 2.4×10^{-7} $S \cdot m^{-1}$, σ_p (25 µm) = 1.6×10^{-5} $S \cdot m^{-1}$ and σ_p (11 µm) = 2.1×10^{-5} $S \cdot m^{-1}$, respectively.

According to Eq. (2.18), the particles' DEP response depends on the interplay between frequency, conductivity and permittivity of the particles and the medium. Due to their double layer conductance, even after washing the particles have a comparably high overall conductivity, which is, for 11 µm and 25µm, higher than that of the Mili-Q water used as suspension. This is quite usual for polystyrene particles (Ermolina and Morgan, 2005). The 11 µm and 25 µm particles should therefore present positive DEP at low frequencies and negative DEP at high frequencies (due to the much lower permittivity of polystyrene compared to the

suspending medium). The 45 µm particle should show negative DEP at all frequencies (as both conductivity and permittivity are lower for PS than for Milli-Q water). According to Eq. (2.18) and to the results of preliminary experiments, all three particle sizes show negative DEP at the utilized frequency of 200 kHz (Fig. 5.3). The real part of Clausius-Mossotti factor $Re[\tilde{K}]$ for three different size particles at this frequency was calculated using Eq. (2.18) to be the identical value of -0.48.

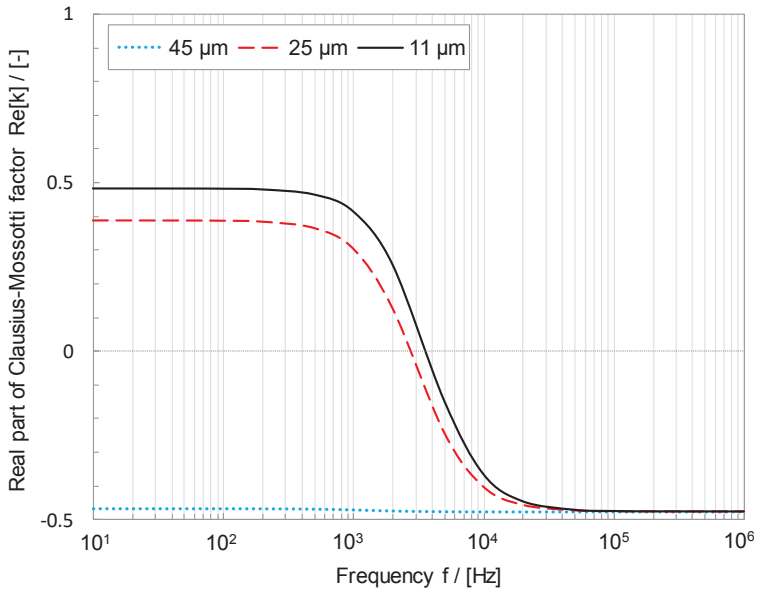

Figure 5.3: Clausius-Mossotti factors evaluation as a function of frequency for 45 µm, 25 µm and 11 µm polystyrene particles after washing step. The electric filed frequency of 200 kHz was utilized for particle trajectory measurements.

5.4.3 Simulation of particle motion trajectories in the cIDE separator

The fluid flow distribution within the separator was simulated to evaluate the influence of the fluid on the particle motion. The 2.7 times higher sheath flow input rate than that of the suspension flow was optimally designed to deflect particles towards the channel bottom before they enter the separation channel (Fig. 5.4a). Maximum flow (red area) appears at the narrow region, in which suspension flow and sheath flow intersect into a mixed flow with a velocity of approximately 1.6 mm·s^{-1}. Due to the different dimensions of the inlet channel and the separation channel, the fluid flow distribution at the interface region gives rise to a slightly upward pointing flow stream at the end of the intersection area. Apart from the interface position, the flow develops homogeneously along the vertical direction of the separator.

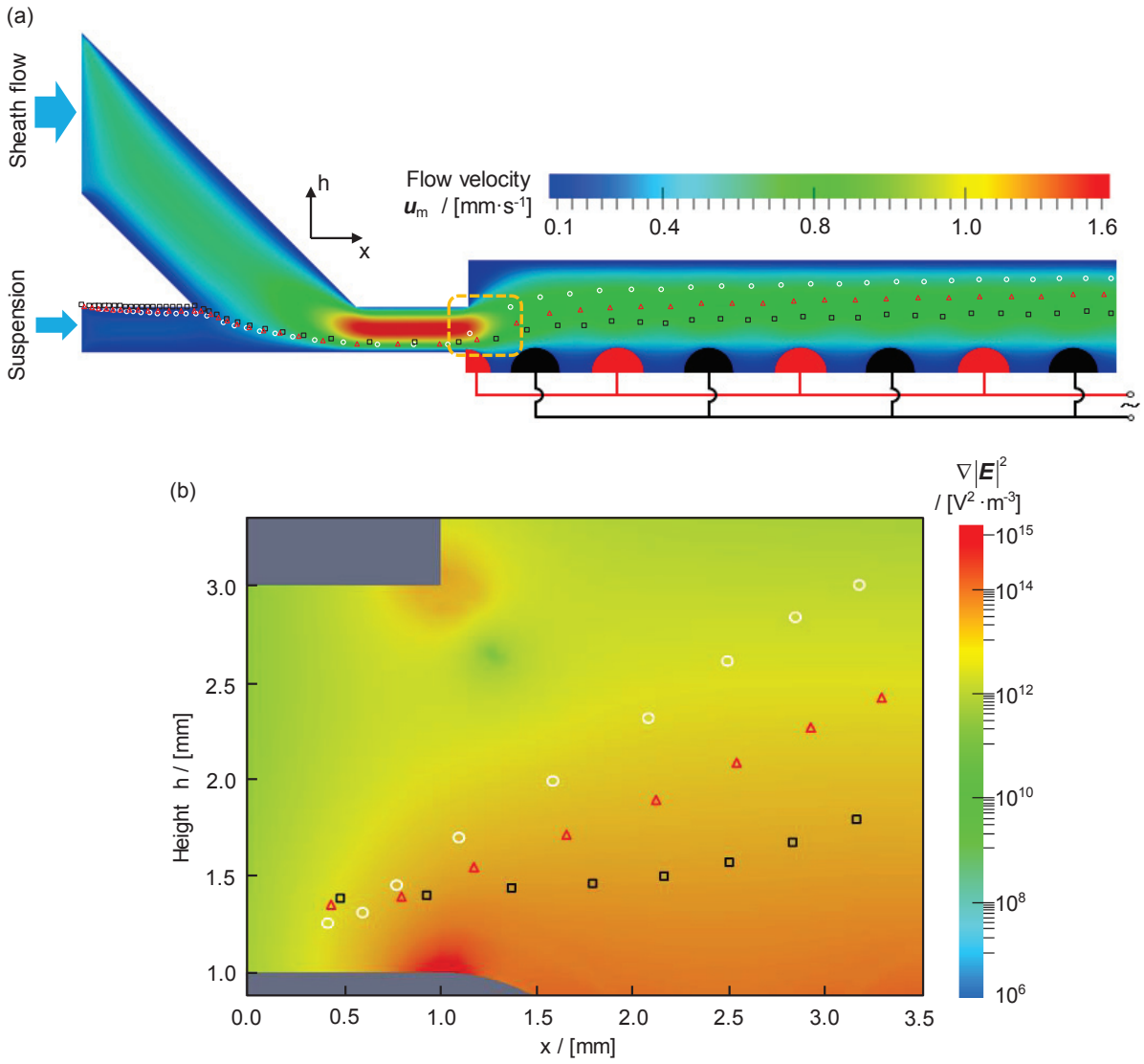

Figure 5.4: (a) Simulated fluid velocity distribution and trajectories of 45 µm (white circle), 25 µm (red triangle) and 11 µm (black square) PS particles (ρ_p = 1005 kg·m^{-3}) suspended in Milli-Q® water (ρ_m = 1000 kg·m^{-3}, μ_m = 1x10^{-3} Pa·s) in the cIDE separator. The time step between two trajectory dots is 2 s. The electric field was generated by a voltage input of 200 V_{eff} at a frequency of 200 kHz. The velocity of both suspension and sheath flow at the channel inlets are 0.1 and 0.27 mm·s^{-1} (simulation), respectively (equivalent to 0.6 and 4.1 mL·min^{-1} in the experiment); **(b)** Particle trajectories in the entrance zone of the DEP separation channel (within the yellow square as indicated in Fig. 5.4a). Time step between two trajectory dots is 0.5 s. The background shows distribution of $\nabla|\boldsymbol{E}|^2$.

The particles, which were injected at the top position of the suspension inlet with a specified initial velocity, were horizontally accelerated and, due to the influence of the sheath flow, perpendicularly suppressed towards the surface of the first electrode. While entering into the separation channel (yellow square in Fig. 5.4a), the particles were levitated significantly to

different heights above the electrode. This is due to a strong negative DEP force (Eq. (2.17)) acting on the polystyrene microspheres in Milli-Q water at a frequency of 200 kHz. Larger particles were repelled to higher positions than smaller particles, which is due to the cubic dependence of the DEP force on the particle radius, as described by Eq. (2.17).

Fig. 5.4b shows detailed particle trajectories in the yellow square region with the $\nabla|\boldsymbol{E}|^2$ distribution as background. As it can be seen, the 45 µm particles (white circle) are repelled with the highest vertical velocity, whereas the 11 µm (black square) particles rise up slower. The three particles gained a levitation height difference of 1.8 mm, 1.1 mm, and 0.4 mm during their passage of the highlighted area. The particle levitation is fastest in the highlighted region. The following experimental validation of particle trajectories will thus focus on this region.

In the yellow square region, the DEP force reduces dramatically with particle height (particle-electrode distance) due to the small electrode spacing of 1 mm. The loss of DEP force is compensated thereafter by the larger spaced electrodes that provide a much larger DEP working area throughout the rest of the separation channel. As a result, although the particles rise slower after passing the first pair of electrodes, the DEP levitation continues further in general. The effective DEP working area provided by the widely spaced electrodes levitates particles in competition with gravity in perpendicular direction (*h*), which results in different vertical positions *h* (depending on particle size) at the same horizontal position *x* (Fig. 5.4a). Simulation of particle trajectories indicate that dielectrophopretic size-based dynamic fractionation can be realized before reaching the steady state, at which all particles independent of size will have the same vertical position.

5.4.4 Mesh resolution study

The demonstration of self-consistency of the underlying PDE (partial differential equation) is of fundamental importance in simulation and thereby the impact of mesh resolution on both the electric field and flow field was numerically evaluated. For the distribution of fluid flow, negligible changes can be seen in Fig. 5.5(a) and (b) while slight differences were found in Fig. 5.5(c) with varied mesh resolution. Note that the variation of flow velocity in Fig. 5.5(c) at the region that affects particle motion (highlighted in blue) reduces gradually with increased mesh resolution. Particularly there is almost no difference of flow profile between mesh 4 and 5, indicating the independence of fluid on mesh at this point. Besides, the maximum difference of flow on mesh resolution within the blue region appears at the height of 1.8 mm with a flow velocity of 0.79± 0.02 mm·s^{-1} (*n*=5). The deviation is considered to be acceptable for precise fluid flow calculation.

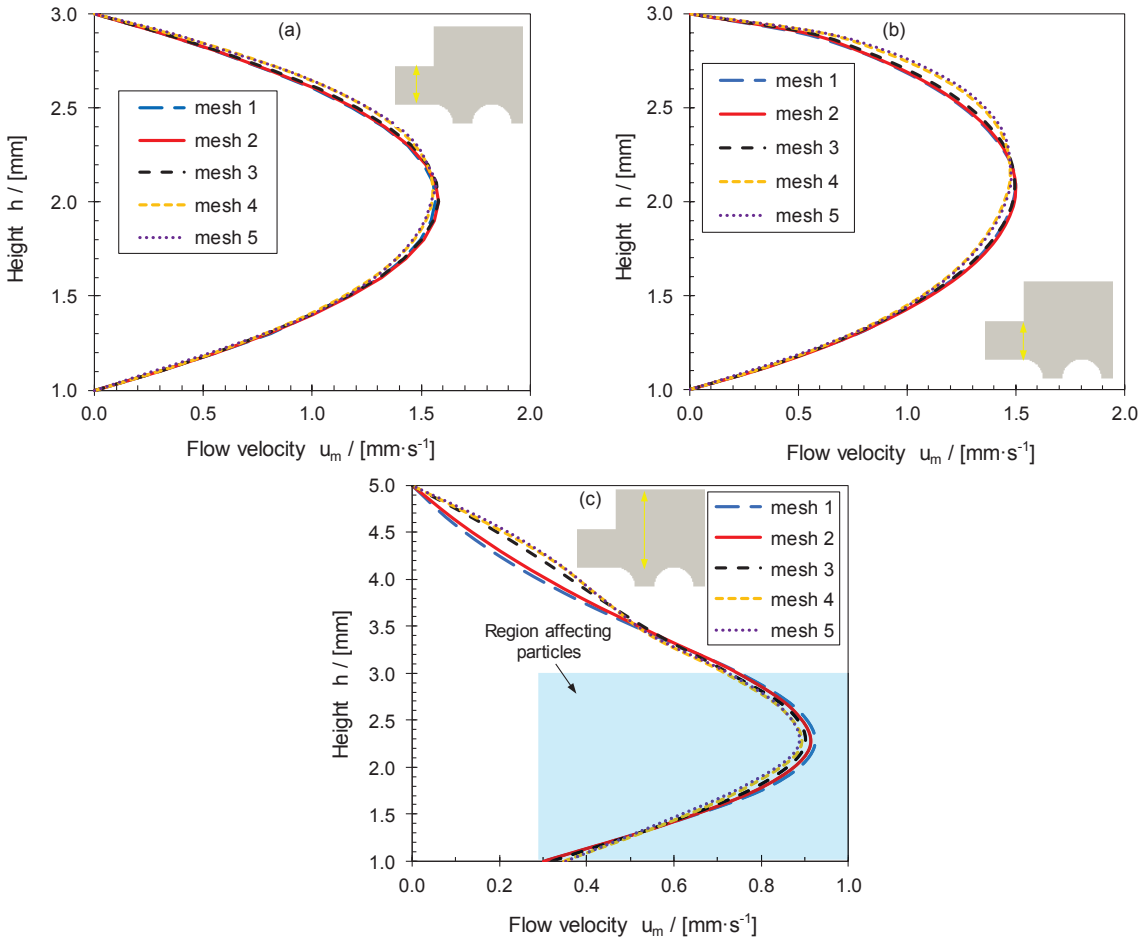

Figure 5.5: Dependence of the fluid flow distribution on mesh resolution. Three different x positions **(a)** *x*=0 mm, **(b)** *x*=1 mm and **(c)** *x*=2.5 mm were evaluated with varied mesh resolutions (mesh 1: 34 200 cells; mesh 2: 136 800 cells; mesh 3: 307 800 cells; mesh 4: 855 000 cells; mesh 5: 3 420 000 cells) at each position. Lines were plotted over height *h* as indicated by the yellow double-headed arrow with grey geometry as background.

For the gradient of square of the electric field, no change was found at both center of electrode gap (Fig. 5.6(a)) and center of electrode (Fig. 5.6(b)). However, significant variations arise at both the electrode edge and the 90-degree edge (Fig. 5.6(c)). This is attributed to the numerical error that arises in calculating Laplace's equation very close to boundaries. It is already known from the literature (Green et al., 2002) that numerical solutions for Laplace's equation are incorrect close to electrodes or 90-degree edges. Nevertheless, this numerical error does not affect the region of particle motion (highlighted in blue in Fig. 5.6(c)) since the concept of contact-free fractionation proposed in our manuscript allows that particle moving at regions away from both electrodes and boundary walls. At the region affecting particles, no difference was found of field gradient with varied mesh resolutions.

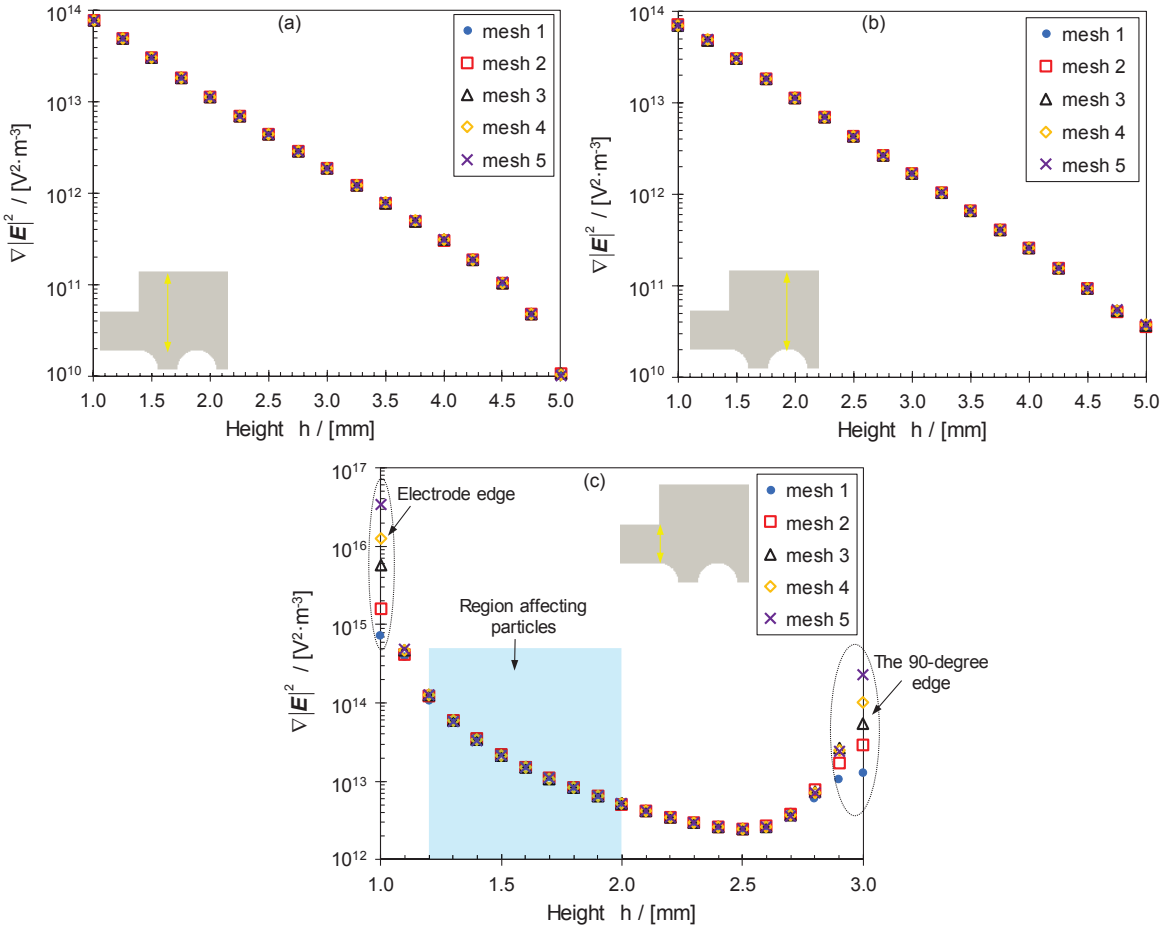

Figure 5.6: Dependence of gradient of square of the electric field distribution on mesh resolution. Three different *x* positions **(a)** *x*=2.5 mm, **(b)** *x*=4 mm and **(c)** *x*=1 mm were evaluated with varied mesh resolutions (mesh numbers are consistent with Fig. 5.5).

5.4.5 Experimental validation of particle trajectories

Experimental volumetric flows of suspension and sheath at the inlet were set to be consistent with the simulation. Both flow rate calculations were verified experimentally by measuring 11 µm particle velocities at *x* = 0 (cf. Fig. 5.4b) and at different *h* ranging from 1 to 3 mm. Under the assumption of a small Stokes number, the particles will follow the fluid stream directly. This allows for measuring the fluid profile by analyzing the particle velocity as a function of *h* (Fig. 5.7). As shown in Fig. 5.7, experimentally obtained particle velocities (red dots) at different heights present good agreement with the fluid profile simulation (blue line). However, some higher particle velocity values than shown by the fluid profile where found especially at the midstream position at *h* = 2 mm, which is probably attributable to the unstable sheath flow caused by the use of the peristaltic pump.

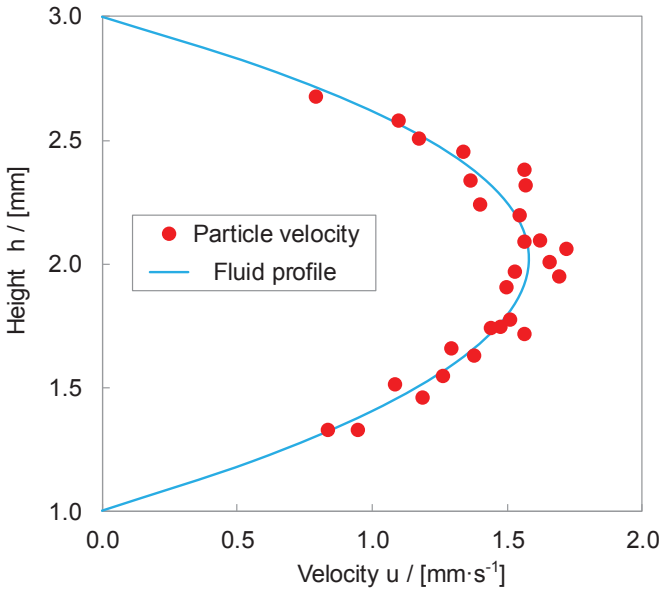

Figure 5.7: Comparison of simulated fluid profile with experimentally measured 11 µm particle velocities. Volume flow rates of both simulation and experiment are consistent with Fig. 5.4. (Experimental data of particle velocity see Appendix A, Table A.3)

When measuring fluid flow using tracers (seed particles), the particle response time should be much smaller than the characteristic time scale of the fluid (Stokes number $Stk << 0.1$). The particle motion trajectories can then be used to estimate the fluid flow with sufficient accuracy (Crowe et al., 2011). The Stokes number is defined as the ratio of the particle relaxation time (τ_p) to the characteristic time of the fluid medium (τ_m), given by (Park and Jung, 2009):

$$Stk = \frac{\tau_p}{\tau_m} = \frac{2a^2 \rho_p u_{\max}}{9 \mu_m L_c} \tag{5.3}$$

where $u_{\max}$ is the maximum flow velocity. The Stokes number was calculated using Eq. (5.3) to be 4.25×10^{-6}, meaning that the particles will follow the fluid stream almost immediately. Trajectories of 45, 25, and 11 µm polystyrene particles were experimentally obtained by capturing the particle motion and thereafter measuring particles' *x* and *h* positions at identical time steps (0.5 s) in the highlighted region (yellow square in Fig. 5.4a) and the results are plotted in Fig. 5.8 (filled symbols) against the particle trajectories obtained by simulation (unfilled symbols). The filled symbols represent the experimental particle mean positions and the bars represent position ranges (maximum and minimum positions at each time step). Differently to the simulation, the utilization of the syringe pump for experimentally injecting particles to the suspension inlet resulted in random particle initial positions. Nearly all simulated particle positions are in good agreement with the experimental results, indicating that the model prediction of particle trajectory is reliable.

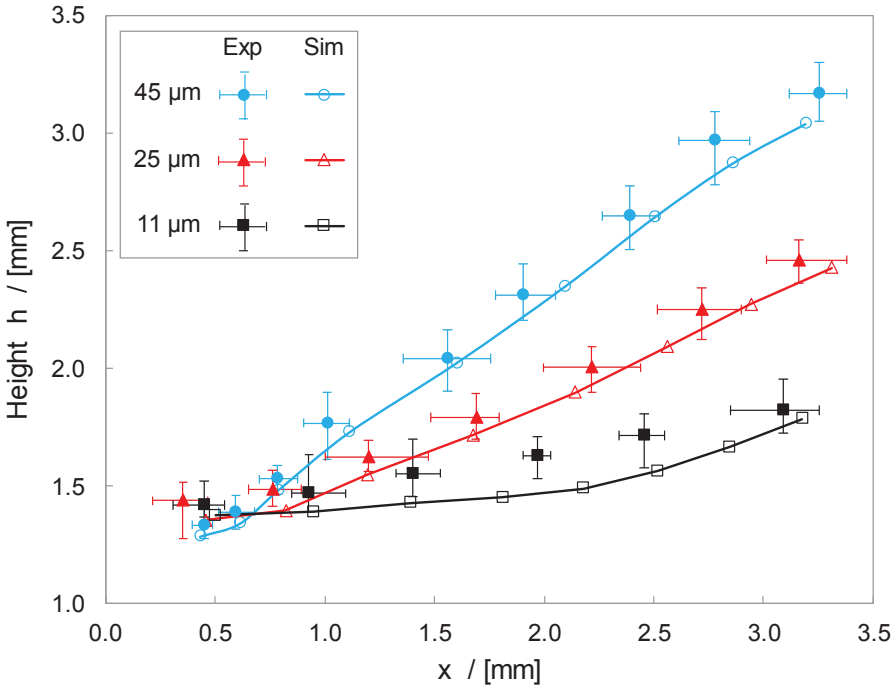

Figure 5.8: Comparison of experimental and simulated results for particle trajectories. Filled symbols with position bars represent experimental results while non-filled symbols connected with a continuous line represent simulated results. All the operation parameters are consistent with Fig. 5.4. (Experimental data particle position see Appendix A, Table A.2).

Due to the utilization of the cooling system, no significant temperature change was observed during experimental particle trajectory measurements. In addition, the calculated temperature rise in this system (U_{rms} = 200 V_{eff}) based on two temperature rise approximations which dominate in different scale systems is 0.37 K (Eq. (2.43)) and 0.05 K (Eq. (2.53)), respectively. Both temperature rises are considered acceptable for DEP based devices since the temperature rise of less than 1-2 K does not significantly alter the material properties (Mathew et al., 2015) and does not influence the particles motion trajectories.

For 25 µm and 11 µm particles, the experimental mean residence time is 12.5 % and 25 % smaller than the residence time from the simulation. This is because the unstable sheath flow, as mentioned above, gives rise to higher experimental flow rates especially at the midstream position. To our surprise, this increased flow rate in the experiments has almost no impact on particles' perpendicular levitation as compared to simulation because of the extremely strong DEP force, which allows a further increase of the volume flow rate for reaching higher throughput. The increasing deviation of the experimental particle positions towards higher values of *h* with decreasing particle size suggests a small deviation between the experiment and the simulated fluid flow. The fluid flow points slightly upwards after passing the constriction that will cause an upwards pointing drag force on the particles. The drag force has a quadratic

dependence on the particle diameter whereas the DEP force has a cubic dependence. Hence, with decreasing particle diameter the drag force becomes more dominant over the DEP force. The deviation between the experimental fluid flow and the simulated fluid flow could, for example, be caused by the pulsed flow that is generated by the peristaltic pump.

5.4.6 Performance analysis

The performance of the proposed cIDE separator was quantified by introducing a dimensionless parameter, resolution of fractionation *R*, which is defined as the ratio of the specific target particle size, d_p^*, and the smallest size difference that can be separated, $\Delta d_p = d_{p2}^* - d_{p1}^*$ (Fig. 5.1d):

$$R = \frac{d_p^*}{\Delta d_p} \tag{5.4}$$

The definition of *R* is derived from Flagan (Flagan, 1999) for describing the performance of the differential mobility analyzer. Eq. (5.4) indicates that, for a certain particle size, the resolution increases with decreasing size difference Δd_p. In the current cIDE separator, the size difference is constrained by the width of the collector *W* at the channel outlet (Fig. 5.1d). Physically, the outlet must have a certain finite size, even if it is positioned at the correct height for a certain particle diameter. In this case, particles being a little smaller (d_{p1}^*) or bigger (d_{p2}^*) than the target particle size will also pass through the collector (Fig. 5.1d), which gives rise to a broad outlet particle size distribution. The resolution *R* is thus the ratio between target diameter and difference in separable particle size Δd_p, that is, the difference in diameter between the biggest and the smallest particle that would pass the outlet. This value depends, amongst others, on the width of the outlet. It was defined in a way that, when fractionating a certain particle size from a mixture of particle sizes, the higher the fractionation resolution, the smaller the output particle size distribution and hence the higher the purity of resultant output particles.

Fig. 5.9 illustrates the dependence of the resolution on collector width for particles with different size. Each specific particle size was plotted with a bar (Δd_p) for showing the size difference. For a given collector width, the fractionation resolution *R* varies with the particle diameter. The first rise in the resolution can be attributed to the increasing difference in levitation speed with increasing particle size (due to the cubic dependence of the DEP force on the particle radius). A peak point appears at the specific particle diameter of around 20 µm. With increasing particle diameter above 20 µm the resolution drops again. This is due to the fact that bigger particles reach the equilibrium faster. The drop in resolution is then because

the bigger particles are already close to equilibrium and hence have only small differences in levitation height. A longer channel might be required for the fractionation of small particles to achieve better DEP levitation along the channel length, while a shorter channel might be demanded for larger particles to discriminate them before they reach the equilibrium. As a consequence, the presented 20 µm optimum particle diameter is a value specific for the given channel length and will thus vary with varying channel geometry.

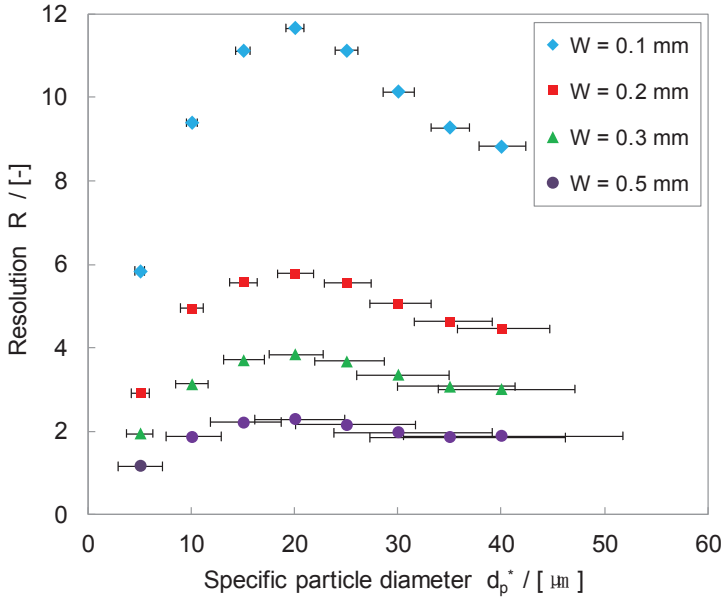

Figure 5.9: Calculated separation resolution as a function of specific particle diameter and collector widths. The bars represent Δd_p. All the operating parameters are consistent with Fig. 5.4.

The variation tends to be more prominent at smaller collector widths, i.e. at 0.1 mm it is possible to achieve much higher resolution for all particle sizes compared to other widths. Correspondingly, fine fractionation of particles with even smaller size differences can be realized with expected high resolution. On the contrary, at large widths of the collector, particle separation is only possible with huge size differences, resulting in relatively low resolutions. Although the resolution of fractionation can be improved by narrowing the width of the collector, it is in fact not possible to separate large particles with a very small collector width, since particles would aggregate and thus clog the collector, especially at high concentrations (Moschallski et al., 2010). In addition, decreasing the collector width might cause the undesired turbulence or vortex at the channel outlet due to high Reynolds number of the fluid, which give rise to a reduction of fractionation efficiency. Thus, a tailored outlet channel design with a collector width that is in accordance to the particle size is a key aspect for an effective fractionation. The required outlet channel width can be calculated and presented as a function of the desired resolution and the outer system parameters. It was found that the resultant width

of the collector is strongly dependent on the operating parameters. For a given resolution, the collector width can be enlarged with increasing applied voltage (Fig. 5.10). This is due to the improvement of DEP force resulting from high voltage input enhances particles' dielectrophoretic levitation and there by the height difference between them. The enlargement of collector width with voltage seems to be more prominent especially at low resolutions. Different diameter particles are compared to evaluate the dependence of the relevance between voltage and collector width on particle' specific size, which present analogous variation tendency.

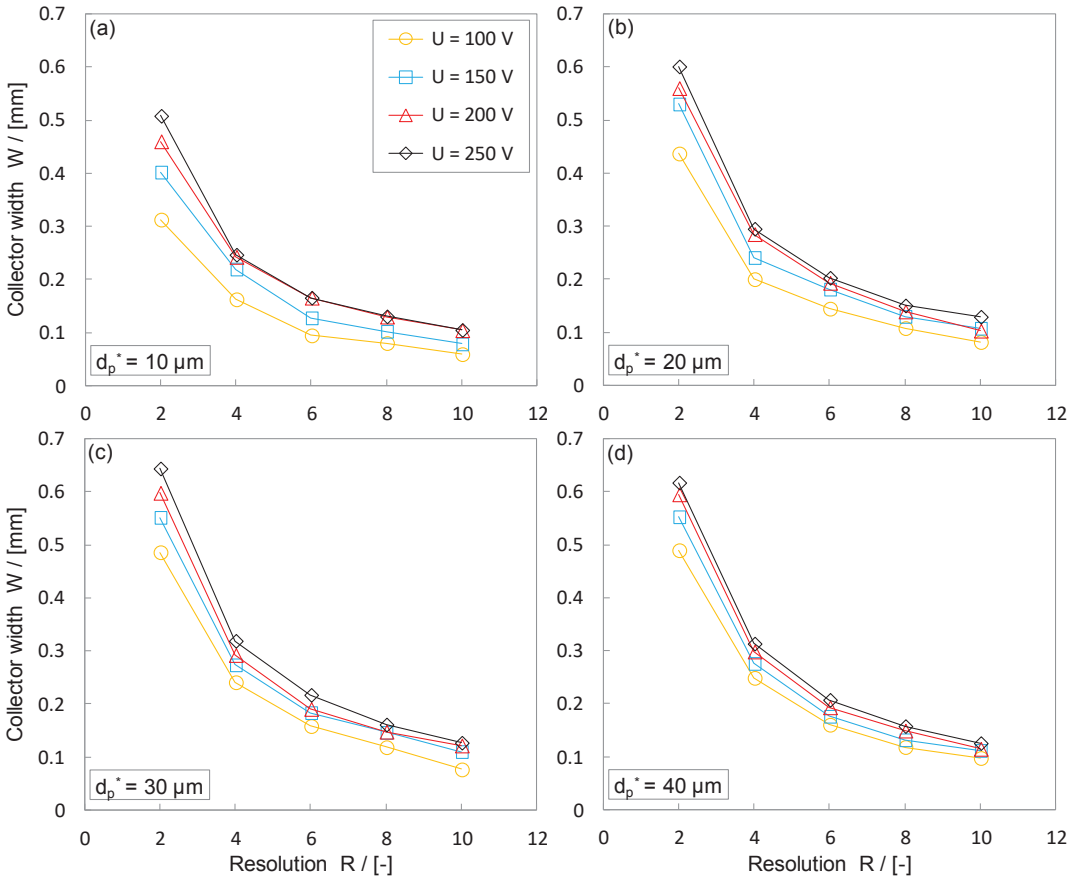

Figure 5.10: Calculated collector width *W* as a function of the desired resolution *R* for varied voltage input and constant volume flow rate (4.7 mL • min^{-1}). Specified particle size with **(a)** 10 µm, **(b)** 20 µm, **(c)** 30 µm and **(d)** 40 µm in diameter is evaluated, respectively.

Another important operating parameter, i.e. volume flow rate, which determines the DEP system's throughput, was numerically investigated to examine its impact on resultant width of the collector. Differ from voltage, an increasing of volume flow rate gives rise to a reduced collector width at certain resolution. This might be attributed to the loss of DEP response time for effectively levitating particles to the desired height and thereby reduces the height difference between them at high flow rates. Moreover, small particles are more sensitive than

large particles, as they show a stronger dependence of the resultant collector width on the volume flow rate (compare 10 µm particle Fig. 5.11a to 40 µm particle Fig. 5.11d).

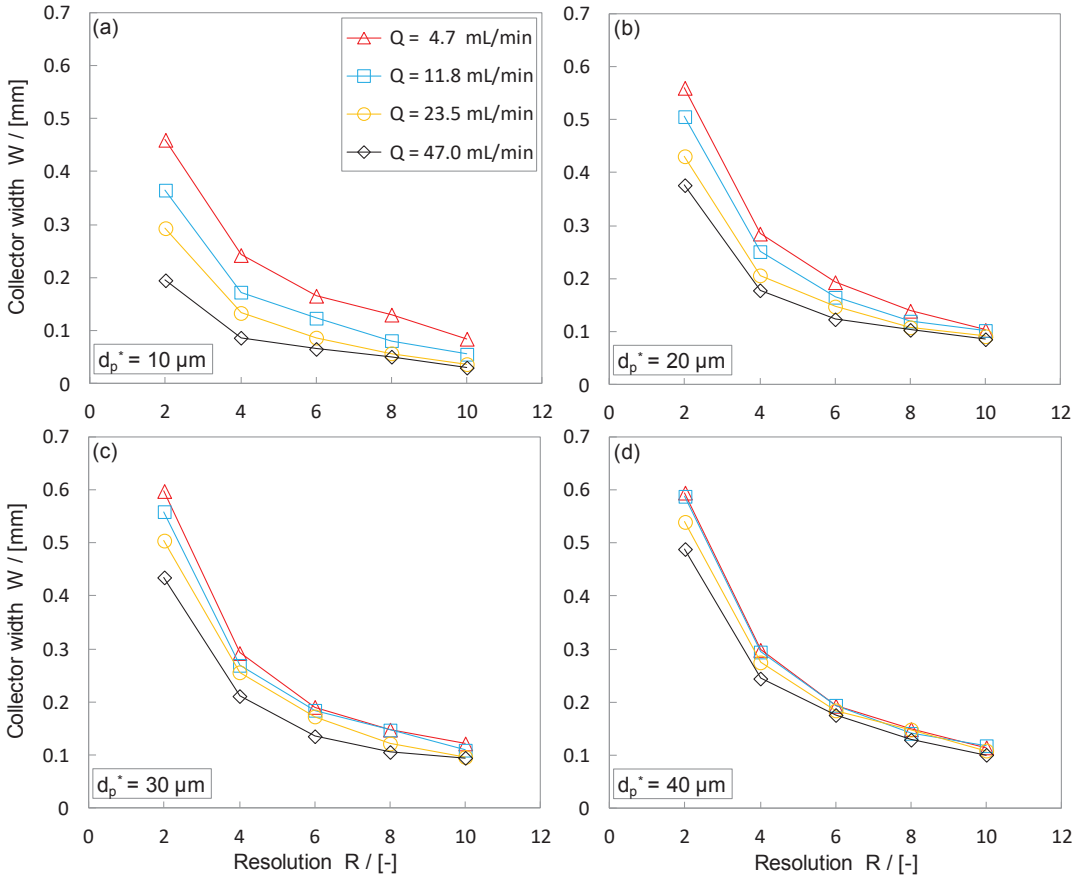

Figure 5.11: Dependence of the required collector width on volume flow rate at different resolutions. The voltage input in this case is 200 V_{eff} with specific particles size of **(a)** 10 µm, **(b)** 20 µm, **(c)** 30 µm and **(d)** 40 µm being considered.

The dependence of the fractionation resolution on both operation parameters was quantitatively evaluated (Fig. 5.12). For a specific particle size and a given collector width, resolution increases with voltage input, while it drops with increasing volume flow rate. To the best of our knowledge, the majority of DEP applications with respect to continuous microparticle separation were achieved with maximum system volume flow rates of up to 1 mL·min^{-1}. The proposed cIDE separator could achieve fractionation of 10 µm particles at a high resolution of R = 5 (i.e., separating 10 µm particle from 9 µm and 11 µm particles) and a minimum flow rate of 4.7 mL·min^{-1} (Fig. 5.12), which is a nearly fivefold increase of throughput compared to the literature. Surprisingly, a further increment of the volume flow by one order of magnitude to 47 mL·min^{-1} is calculated to be possible with a fractionation resolution of R = 2, indicating that a separation of 10 µm particle from 7.5 µm and 12.5 µm particles is possible

(Fig. 5.12). In any case, it is a step towards dielectrophoretic based particle fractionation at high throughput.

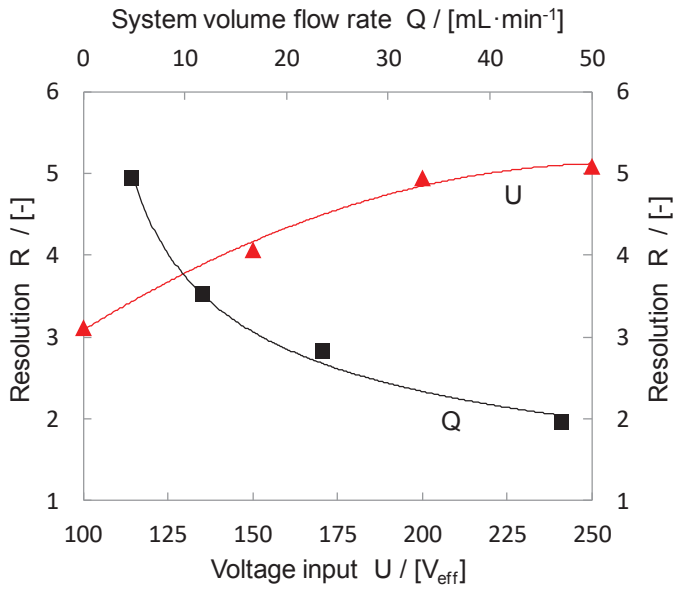

Figure 5.12: Numerical estimation of the dependence of voltage input *U* (filled triangle with red fitting line) and system volume flow rate *Q* (filled square with red fitting line) on resolution *R*. Particles of 10 µm in diameter where evaluated with a specified 0.2 mm collector width. The solid lines are fitted to the simulated data (points) to guide the eye.

5.4.7 Evaluation of the DEP effect on cell viability

Electric fields are known to affect the viability of biological cells. Hence, in case of cell manipulation it is important to assess the influence of the applied voltage on the cells. The effect of DEP on cell viability mainly depends on both the electric field strength and the Joule heating effect (Bisceglia et al., 2015; Qian et al., 2014). The electric field directly affects the cell viability by inducing a transmembrane potential superimposed on the endogenous potential of the cell membrane. If the total membrane potential exceeds the order of 0.2-1 V for several cell types, then dielectric membrane breakdown occurs (Heida, 2012; Mernier et al., 2010). Voldman (2006) proposed an approximation of the imposed transmembrane potential V_{tm}, as:

$$|V_{tm}| = \frac{1.5|\boldsymbol{E}|a}{\sqrt{1+(\omega\tau)^2}} \tag{5.5}$$

where τ is the time constant given by:

$$\tau = \frac{ac_m(R_{cyto} + \frac{1}{2}R_m)}{1 + ag_m(R_{cyto} + \frac{1}{2}R_m)} \tag{5.6}$$

where R_{cyto} is the cytoplasmic resistances and c_m and g_m are the cell membrane specific capacitance and conductance, respectively.

For example, the calculated $|V_{tm}|$ of a 10 μm diameter cell in an electric field with an applied voltage of 200 V_{eff} (the maximum electric field strength $\boldsymbol{E}$ is 2×10^5 $V\cdot m^{-1}$) at frequency of 200 kHz, is only 0.26 mV. This is much lower than its endogenous potential (approximately 75 mV in (Voldman, 2006)), therefore, very little stress is imposed on cell membrane and hence dielectric membrane breakdown will not happen. Also, the maximum field strength utilized in this case ($2.5x10^5$ $V\cdot m^{-1}$) is nearly three times below the critical value ($7x10^5$ $V\cdot m^{-1}$), which was indicated by Bisceglia et al. (2015). Only values above this limit should affect the cells' structure and induce apoptosis in cells.

Electric fields in a conductive medium will also cause power dissipation in the form of Joule heating. A temperature variation lower than 1 K is considered as approximate daily variation in cell temperature (Heida, 2012). While a temperature rise of more than 4 K above cells physiological temperature can result in cell death (Zellner and Agah, 2012). As mentioned above, the calculated temperature rise in our case is 0.37 K and 0.05 K, respectively. This indicates that, Joule heating will not be a problem for cell separation in this proposed process.

5.5 Discussion

In this chapter, a novel DEP separator with cIDE configuration was proposed for continuous microparticle fractionation at high throughput. It is based on a dielectrophoretic manipulation of particle trajectories in a flow field. The concept requires the channel to be long enough to cover the entire region in which all particle sizes ascend towards their equilibrium state. On the other hand, depending on the target particle size and the flow rate, the channel cannot be arbitrarily long, as particles will eventually reach an equilibrium height which is identical for all particle sizes. This method can be considered as contact-free, because the electrodes, which cause the size specific levitation, repel the particles sufficiently due to the negative DEP effect and the particles do not need to be in contact with the electrodes. Besides, the electrodes utilized in this system were coated with dielectric insulation film (rutile) in which bare metal electrodes are not in direct contact with the sample fluid. Hence, it is expected that the reported issues associated with conventional DEP platforms such as electrode fouling, contamination

and bubble formation (Shafiee et al., 2009) can thus be prevented. By tailoring the design of the cylindrical electrode arrangement, i.e., increasing spaces between the first three electrodes, both a strong DEP force field at the first few electrodes and a broader DEP working area generated by the following electrodes are being provided. This allows for sustainable and effective DEP particle levitation.

Trajectories of 45, 25 and 11 μm particles within the cIDE separator were numerically simulated and experimentally validated with good agreement. Dielectrophoresis, having a cubic dependency on the particle radius, in combination with hydrodynamic drag and gravity was successfully used to levitate particles of different sizes to different dynamic positions. The position differences during the transient ascend of the particles allows for a size-based fractionation of particles at the outlet. The voltage needed for size-selectively separating particle trajectories in the proposed device varied between 100 V and 250 V resulting in a maximum electric field strength below 2.5×10^{5} $V\cdot m^{-1}$. This value is nearly three times below the critical value at which the field affects the cells' structure and might induce their apoptosis. From this and the low Joule heating found (a temperature rise below 0.5 K) it can be concluded that the device can be used to size-selectively separate even sensitive microparticles such as living cells. However, when using media of high conductivity (e.g. σ_m higher than 10^{-4} $S\cdot m^{-1}$), significant temperature rise might occur that may interfere with particle trajectories inside the separator. Further, it was found that the channel used in the experiments is too long to separate the microparticles in question without increasing the flow rate by an order of magnitude. Such an increase, however, enlarges the pressure drop of the system and requires a more stable and better sealed system.

With respect to device performance, a dimensionless parameter, resolution, is introduced for quantitative characterization of the fractionation accuracy. Numerical predictions show that the resolution increases with decreasing collector width at the outlet channel. For a given target resolution, the required collector width increases with voltage and decreases with volume flow rate. At a specified width of the collector, a high resolution can be achieved by trading-off voltage and volume flow rate. The results indicate the possibility of continuous dielectrophoretic microparticle fractionation with high resolution and high throughput.

6 Conceptual improvement of IDE-DEP systems by using a concentric cIDE separator – a simulation study

Continuous, high-throughput dielectrophoretic fractionation of microparticles is still faced with problems. Improvement of IDE-DEP-based, continuous-flow systems to provide a sufficient DEP force for particle manipulation is needed, especially in DEP system scale-up, in order to maximize separation efficiency with minimized energy demand. The cIDE separator proposed in Chapter 5 shows good agreement between theoretical and experimental size-dependent particle trajectories, but due to device limitations it only open up the possibility of microparticle fractionation. The major problem encountered here, however, is to achieve size-based separation in a system where particles always experience a balance of both negative dielectrophoretic force and gravitational force for levitation in the vertical direction. Since both these forces scale with the cube of the particle radius, it is very difficult indeed to realize moderate distances of particles perpendicular to the flow and hence to discriminate between them when they have fine size differences but the same density and dielectric properties. In addition, the only way to improve the system's throughput is by increasing the flow velocity, since a relatively low height of the separation channel is required to minimize Joule heating interference, on one hand, while keeping an effective DEP working area along the overall height of channel, on the other hand. Particles carried by high velocity flow do not have enough time to respond to the local effective DEP force field, which may reduce the possibility of separation. These limitations make it difficult for the cIDE separator to meet the requirements for DEP scale-up of microparticle fractionation in order to achieve further improvement in the throughput of IDE-DEP systems.

With respect to the cIDE separator, the presence of the gravitational force with direction inversely to the DEP force confines particle's dielectrophoretic levitation. This problem can be solved by adjusting the cIDE arrangement and the directions of both particle and fluid motion relative to the cIDEs.

In this chapter, a conceptual improvement of IDE-DEP systems is thus proposed by introducing a new separator with concentrically assembled cIDEs for continuous size-based fractionation of microparticles with different populations (size range from 1 μm to 45 μm). This new separator is design tailored to eliminate the interference of gravity on the dielectrophoretic motion of particles, in that both the DEP force and the gravitational force are positioned in a right-angle. Improved throughput is expected in this system due to the absence of gravity in competition with DEP, thus providing an expanded coverage range of the DEP force field for

effectively moving particles. To examine the effectiveness of such a design, the distribution of both the electric field and the flow field in the concentric cIDE separator are numerically simulated and motion trajectories of differently sized microparticles are theoretically predicted. A series of numerical studies are also conducted to evaluate the impact of system parameters on fractionation performance. Such numerical simulations are expected to provide useful information for further understanding the behavior of particles in scaled-up dielectrophoretic field-flow systems designed to achieve controllable and accurate microparticle fractionation.

6.1 Design of the concentric cIDE separator

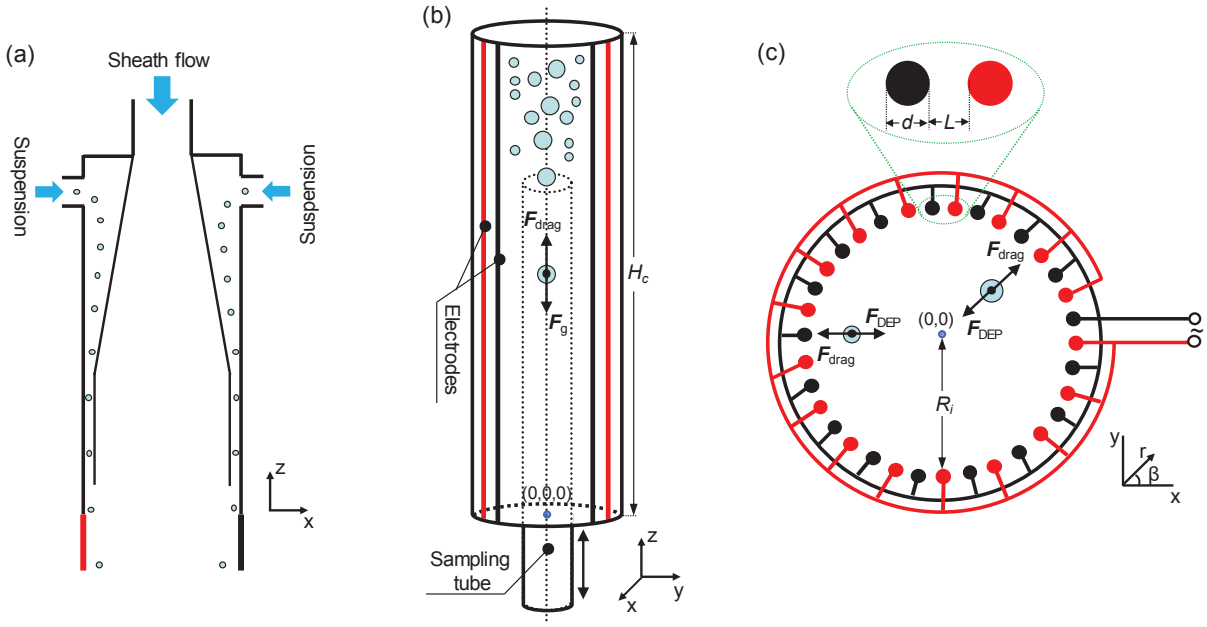

Figure 6.1: (a) Side view (*y, z*) of the particle distributor designed to distribute particle suspensions to a position in the vicinity of the electrodes. **(b)** Three-dimensional (*x, y, z*) schematic diagram of the concentric cIDE separation chamber, with a tunable sampling tube coaxially installed for size-based microparticle fractionation; **(c)** Top view (*x, y*) of the concentric cIDE separator with two groups of cylindrical electrodes (red and black) arranged interdigitatedly and concentrically, and which are connected to the power supply. Polar coordinates (*r, β*) are introduced to describe a particle's radial position. The relations between (*x, y*) and (*r, β*) are $x = r \cos \beta$ and $y = r \sin \beta$.

The proposed concentric cIDE separator is composed of a particle distributor and a separation chamber. The particle distributor comprises a sheath flow inlet channel and a number of suspension inlet channels, which are designed to ensure that the great majority of suspended particles are moved along the annular area around the inner shell of the distributor (Fig. 6.1a). Particles in this area are more likely to acquire a maximum DEP force, as they are positioned

in the vicinity of the electrodes. The separation chamber contains a concentrically arranged cIDE configuration and a movable sampling tube installed along the central axis (Fig. 6.1b). In this configuration, the cIDE is composed of 32 cylindrical electrodes each having a diameter *d* of 2 mm and spaced equidistant from each other by a distance *L* of 1.34 mm. All the cylindrical electrodes are arrayed coaxially with the inner radius R_i of 16 mm (Fig. 6.1c). Typically, the highest electric field generated by such an electrode configuration is close to the cylindrical electrodes, while the lowest electric field is expected at the center. In the case of a negative DEP effect, those particles located in the vicinity of electrodes will therefore be repelled radially toward the central axis (Fig. 6.1c). Since the particle's dielectrophoretic velocity depends quadratically on particle size (Eq. (2.31)), the trajectories of particles will vary accordingly with size, and hence also the residence time before reaching the central axis. The movable sampling tube is expected to collect particles of a certain size fraction at a certain position along the central axis of the separation chamber.

6.2 Model and simulation

In order to predict particle motion trajectories in the concentric cIDE separator, the modified Lagrangian single particle tracking model developed in Chapter 5 will be employed again in this chapter, due to the problem of similarity. The model and the assumptions on which it is based can be found in Chapter 5 (Section 5.2.1).

Simulations were performed using a three-dimensional (3D) geometry (Fig. 6.1b). *OpenFOAM* is used to calculate the distribution of both electric field and flow field, as well as particle motion positions within the separation chamber. In this method, one-way coupling is considered as particles are small compared to the channel dimensions (especially in millimeter DEP systems), which means the presence of particles does not affect the overall electric field and flow field significantly (Jubery et al., 2014; Knoerzer et al., 2016). Laplace's equation is applied here to govern the electric field (Eq. (3.7)). *Dirichlet* boundary conditions is applied for calculating the electric potential: $\phi = \pm U_{rms}$ for each neighboring electrode while $\phi = 0$ for the rest of the computational domain. The fluid flow in the separation chamber is governed by the Navier-Stokes equation and the continuity equation (Eq. (5.2)). Uniform values for velocity at the inlet were specified, while non-slip velocities were assigned to the channel wall and electrodes. *Neumann* boundary conditions ($\frac{\partial \boldsymbol{u}_m}{\partial n} = 0$) were given for the outlet.

6.3 Results

6.3.1 Simulation of the electric field distribution

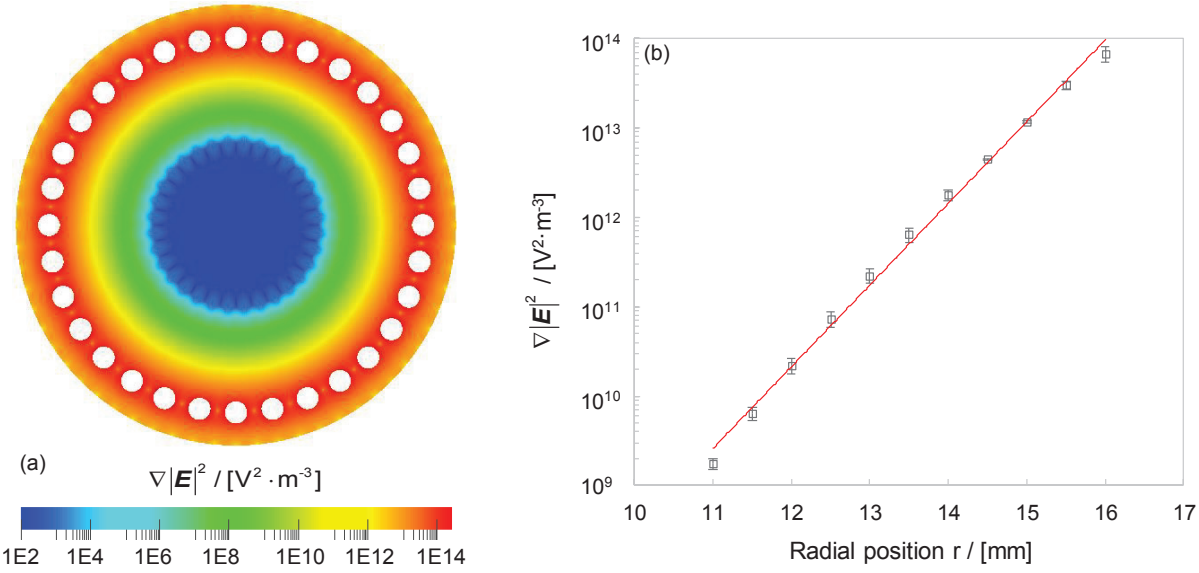

Figure 6.2: (a) Simulation of the gradient of the square of the electric field generated by the concentric cIDE separator with an electrode diameter *d* of 2 mm, a distance *L* of 1.34 mm between electrodes, an inner radius of concentric channel R_i of 16 mm, and powered by an input voltage of 200 V_{eff}; **(b)** Plotted values of $\nabla|\boldsymbol{E}|^2$ against radial position. The non-filled square indicates the calculated mean value of the electric field gradient. The error bar represents standard deviation (n = 5), which was obtained by varying β over a pair of electrodes (from 0 to 22.5 degree). The gray solid line represents the exponential fit of field gradient with R^2 = 0.9958.

Fig. 6.2(a) shows the distribution of $\nabla|\boldsymbol{E}|^2$ at radial cross section (r, β) of the separation chamber. As expected, strong $\nabla|\boldsymbol{E}|^2$ regions are found around the electrodes, with maximum $\nabla|\boldsymbol{E}|^2$ values of 2.7x10^{14} V^2·m^{-3} generated on either side of the cylindrical electrode. Weak $\nabla|\boldsymbol{E}|^2$ regions appear at the center of the radial section, with minimum values approaching zero. The mean value of $\nabla|\boldsymbol{E}|^2$ decays exponentially along the radial direction with distance from the electrode (Fig. 6.2b), which is considered to be similar to the distribution of $\nabla|\boldsymbol{E}|^2$ in the cIDE separator (Fig. 5.2b). However, the dielectrophoretic controllability of the two separators are different. For example, for a minimum $\nabla|\boldsymbol{E}|^2$ value of 1x10^{11} V^2·m^{-3} for effectively moving particles, both separators have similar operating length, i.e., distance of the particle relative to the electrode, of around 3.5 mm, with an identical voltage input of 200 V_{eff}. However, the effective range of the DEP force, which is determined by the effective cross-

sectional area, is enlarged by a factor of 1.8 in the case of the concentric cIDE separator (313 mm^2), as compared to the cIDE separator (175 mm^2). Note that under the $\nabla|\boldsymbol{E}|^2$ value of $1x10^{11}$ $V^2 \cdot m^{-3}$, a 45 µm particle in the concentric cIDE separator still has a net DEP velocity of 6 $\mu m \cdot s^{-1}$ (calculation based on Eq. (2.31)). This velocity is remarkable compared to a zero net DEP velocity when the same $\nabla|\boldsymbol{E}|^2$ level is produced by the cIDE separator. Therefore, even when an identical suspension flow rate is applied, the volume flow and thus the throughput of the concentric cIDE separator can be improved by a factor of at least two.

To assess simulation accuracy, the influence of mesh on the field gradient distribution was examined by varying the mesh resolution (defined by the mesh number in the *x* and *y* direction, respectively) from 5*5 to 100*100 at each *block* (the cross-sectional region (*x, y*) of the separation chamber consists of 570 blocks). The result shows that the variation of electric field gradient with mesh becomes negligibly small at mesh resolutions above 50*50, at which the mesh is considered to be sufficiently fine to enable precise calculation. A threshold mesh resolution of 50*50 (including 142,500 cells) was finally chosen for the $\nabla|\boldsymbol{E}|^2$ calculation (Fig. 6.2a).

6.3.2 Simulation of particle trajectory in separation chamber

Efficient positioning of the sampling tube for collecting the expected size of particle depends on accurately predicting the motion behavior of particles in the concentric cIDE separator. To visualize particle motion, simulations were performed to determine the trajectories of differently sized particles (ranging from 1 to 45 µm) within the separation chamber (Fig. 6.3). The initial position of particles in the simulation was chosen as 1 mm away from the electrode (r = 15 mm), based on the assumption that the great majority of suspended particles are precisely distributed from the inlet channel. A more homogenously distributed $\nabla|\boldsymbol{E}|^2$ at this radial position (Fig. 6.2b) also allows different particles to move under identical conditions. All the simulated particle sizes were assumed to present a strong n-DEP effect at a frequency of 200 kHz, with the specified real part of the Clausius-Mossotti factor $Re[\tilde{K}]$ being -0.48.

It can be seen from Fig. 6.3 below that particles show analogous parabolic trajectory profiles. Due to the extremely high electric field gradients close to the electrode surface, the strongest DEP forces are exerted on particles there, resulting in significant dielectrophoretic responses of particles at the very beginning. More specifically, particles larger than 10 µm respond rapidly to the DEP effect in this simulation by presenting very large motion displacements in the radial direction (Δr) in the first time step (20 s). This could be attributed to the cubic dependence of the DEP force on particle size as described in Eq. (2.17). When particles are pushed away

from the electrode, their dielectrophoretic motion in the radial direction slows down, whereas their axial velocity induced by the fluid flow that drives particle motion through viscous drag increases gradually in the *z* direction. Differently sized particles show different radial displacements at an identical height (*z* direction) in the separation chamber. This difference allows size discrimination of particles. As a consequence, it is expected that the desired particle size can be collected by adjusting the position of the sampling tube in the *z* direction.

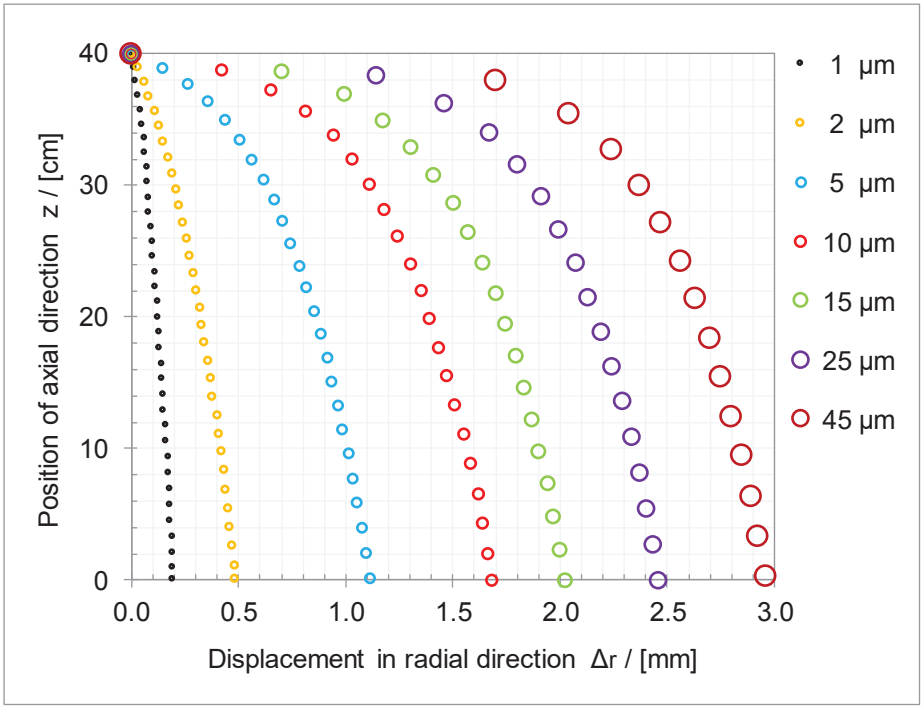

Figure 6.3: Simulated particles' radial displacement Δr along the axial (*z*) direction. A uniform initial flow rate of 1mm·s^{-1} (equivalent to the system volume flow of approximately 60 mL·min^{-1}) was applied in the simulation. The voltage input is 200 V_{eff} at a frequency of 200 kHz. Differently sized particles (ρ_p =1050 kg·m^{-3}) suspended in deionized water (ρ_m = 1000 kg·m^{-3}, μ_m = 1x10^{-3} Pa·s) were initially located at the radial position of r = 15 mm and the axial position of z = 40 cm. The time step between two trajectory dots is 20 s, which is identical for all particle sizes.

In this case, the maximum differences in terms of radial displacements for 45, 25 and 10 µm particles are 0.6 mm and 0.8 mm, respectively. The differences in radial position are considered comparable to the differences in height (0.7 mm and 0.7 mm) produced by the cIDE separator for the same particle sizes. Note that this comparison of dielectrophoretic displacement or dielectrophoretic levitation is based on the same voltage input, but with different flow rates and densities of particles relative to the suspending medium. The system flow rate has a direct influence on the residence time of particles with respect to the local electric field and thus on differences in DEP motion. The concentric cIDE separator has a

system flow rate which is much higher than that of the cIDE separator, which may result in reduced dielectrophoretic motion spaces between particles. Larger particles are more likely to be affected in this case, since they always move at higher velocities in comparison with smaller particles. Another factor, namely particle density, was found to be more sensitive in the case of the cIDE separator, due to the direct impact of gravity on the DEP levitation of particles. For example, to separate heavy particles such as metal minerals in water, the voltage input of the cIDE separator must be increased to produce a stronger DEP force and a greater force coverage range for discriminating particles effectively and compensating for gravity-induced sedimentation. Gravity-induced disturbances caused by local density differences between particles and the suspending medium in the concentric cIDE separator happen only in the axial direction but have little influence on the dielectrophoretic displacement of particles. Hence, those particles having different densities but the same size should basically present the same motion trajectory inside the concentric cDIE separator. It can thus be expected that the concentric cIDE separator provides better dielectrophoretic separation efficiency with minimized gravity-induced disturbance.

6.3.3 Dependence of particle displacement on operating parameters

The radial displacement of particles within the separation chamber, as a result of dielectrophoretic motion, is thought to be a key factor for size-based fractionation. Since differently sized particles have their own paths and therefore radial displacements inside the separator, fractionation can be achieved by exploiting differences in the radial positions of particles. A number of simulations of particle trajectories in a separation chamber were carried out in order to investigate the influence of operating parameters, namely voltage input and system volume flow rate, on the final radial diaplacements of particles at the end of the separation chamber ($z = 0$). It was found that, for certain particle sizes, increasing input voltage causes an increase in dielectrophoretic displacement (Fig. 6.4a). This is because the $\nabla|\boldsymbol{E}|^2$ which determines the DEP force field is proportional to the square of the voltage (Eq. (3.1)). In addition, the variation of displacement with voltage is more sensitive in the case of large particles, as indicated in Fig. 6.4a, where an increase in final displacement of more than 0.6 mm results for a 45 µm particle, compared to an increment of only 0.2 mm for a 1 µm particle when the system voltage is doubled. The volume flow rate dominates the motion of particles in the axial direction primarily, whereas it affects the radial displacement of particles indirectly via the dielectrophoretic response time of particles relative to the electric field. In Fig. 6.4b, the radial displacements of particles apparently decrease with increasing volume flow rate, since

particles do not have enough time to respond to the effective electric field, which in turn causes a reduced DEP effect on particles. In this case, larger particles are more likey to be affected by the volume flow as compared with smaller particles. As a consequense, they are repelled to positions further away from the electrodes, where the flow rates are higher due to the parabolic flow profile. Sensitive analysis of the influence of voltage input and volume flow rate on size-based dielectrophoretic particle displacement provides a thoretical basis for trading-off the operating parameters, enabling more effective separation with high throughput and low energy consumption.

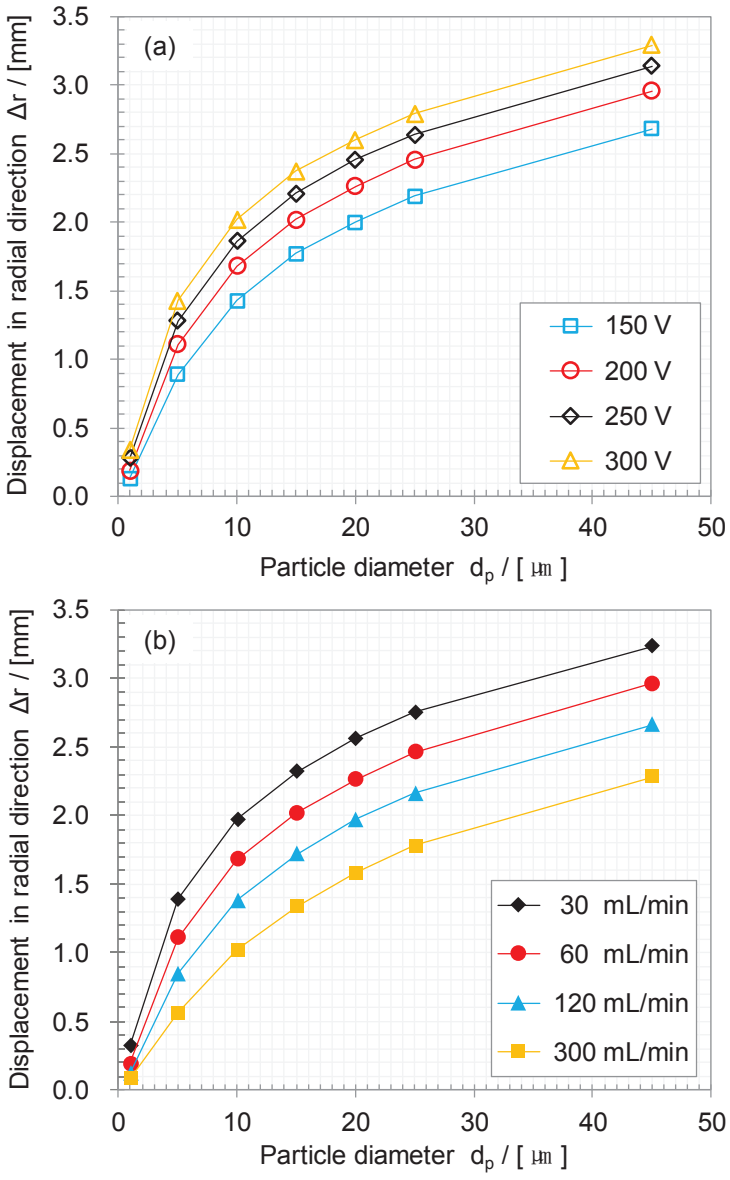

Figure 6.4: (a) Calculated particles' radial displacement at z = 0 as a function of particle diameter for **(a)** different voltages applied while keeping the system volume flow rate constant (60 mL·min^{-1}) and **(b)** different volume flow rates while keeping the applied voltage constant (200 V_{eff}) in simulation.

For those particles smaller than 10 µm in size, the radial displacements presented in Fig. 6.3 are considered indistinctive, offering little chance of being efficiently collected. However, by tailoring the voltage and volume flow rate, it was possible to significantly increase both their radial displacement and their size discrimination (Fig. 6.5). For a 1 µm particle in Fig. 6.5, the radial displacement at the end of the separation chamber was found to be 0.5 mm, which is 2.5 times the amount shown in Fig. 6.3. Meanwhile, for a 5 µm particle under the same conditions, a 0.6 mm increase in final displacement was obtained. These differences in radial position make it possible for even small particles to be easily identified by adjusting the operating parameters accordingly, thus allowing them to be separated.

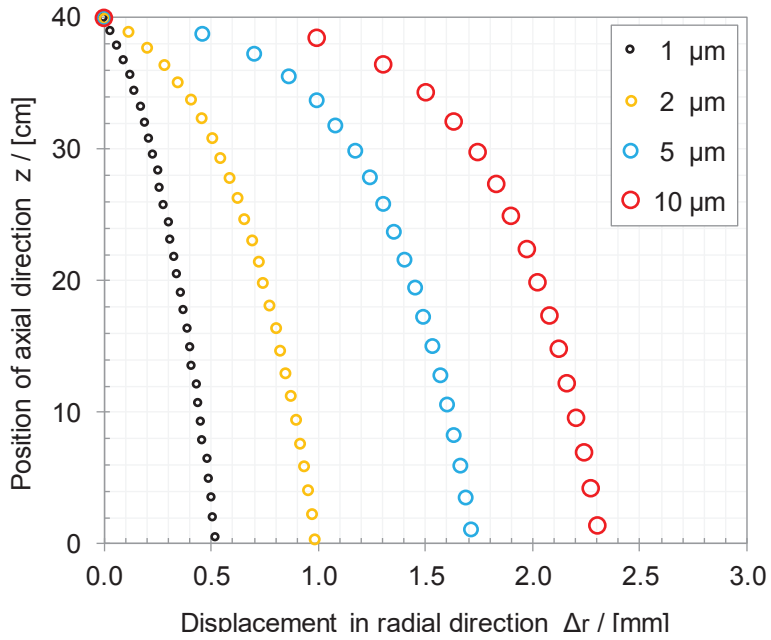

Figure 6.5: Simulated radial displacement of particles along the axial direction. Microparticles with diameters of 1 µm, 2 µm, 5 µm and 10 µm were suspended in distilled water. The voltage input in this case is 300 V_{eff} with a system volume flow rate of 30 mL·min^{-1}. All the other parameters are consistent with Fig. 6.3.

6.3.4 Comparison of the two cIDE separators

To evaluate the performance of the concentric cIDE separator proposed in this chapter, comparisons were made between the cIDE separator and the concentric cIDE separator with regard to several different aspects (Table 6.1). A ten-fold improvement in suspension volume flow rate was achieved in the case of the concentric cIDE compared to the cIDE separator, with almost identical dielectrophoretic discriminating capability, i.e. spatial differences between particles caused by dielectrophoretic levitation/displacement. This improvement of throughput is considered to be an important step forward for DEP separation to reach the final

industrial scale. The influence of Joule heating on particles in both separators can be neglected, as the estimated temperature increase (using Eq. (2.53)) is lower than 1 K. It should be noted that this estimate is based on using a suspending medium with extremely low conductivity in the system, i.e., Milli-Q water. If the conductivity of the suspending medium is higher than 10^{-4} S·m^{-1}, a significant temperature rise may occur and disturb the DEP motion of particles.

The power consumption *P* of the cIDE-DEP system can be described in terms of the applied voltage *U* and the electric resistance of the system R_s as:

$$P = \frac{U^2}{R_s} \tag{6.1}$$

and:

$$R_s = \frac{L}{\sigma_m A} \tag{6.2}$$

where *A* is the cross-sectional area of the system. The calculated energy consumption for two separators using Eqs. (6.1) and (6.2) at an identical voltage input of 200 V_{eff} is 4.1 W and 0.29 W, respectively. This is because the concentric cIDE separator needs to power longer and more numerous electrodes not only to produce a sufficiently high electric field gradient in the vicinity of the electrodes, but also to offer a sustainable DEP force coverage range throughout the separation chamber, so it consumes much more energy than the cIDE separator. One possible solution for reducing the energy demand of the concentric cIDE separator is to use floating electrodes, i.e., electrodes which do not require any connection to the power supply (Golan et al., 2006), in between the cIDE array. The floating electrodes, in combination with cIDEs, are capable of producing the local inhomogenous electric field due to the polarization effect, which is comparable with the excitatory field generated solely by the cIDEs, but require much less energy input since fewer electrodes are connected to the external signal sources. In general, the concept of floating electrode is highly promising, as it provides the opportunity for cIDE-DEP systems to allow continuous separation with reduced energy demand.

Table 6.1: Comparison of cIDE and concentric cIDE separators.

Separator	**cIDE**	**Concentric cIDE**
Number of electrode (-)	26	32
Electrode length (mm)	50	400
Electrode diameter (mm)	2	2
Space between electrodes (mm)	1, 1.5, 2, 2…	1.34

Voltage input (V_{eff})	200	200
Electric field gradient ($V^2 \cdot m^{-3}$)	$1.6x10^{15}$	$2.7x10^{14}$
Suspension flow rate ($mm \cdot s^{-1}$)	0.1	0.53
Suspension volume flow ($mL \cdot min^{-1}$)	0.6	6
System volume flow ($mL \cdot min^{-1}$)	4.7	60
DEP motion difference between 45, 25 and 10 µm particle (mm)	0.7 and 0.7	0.6 and 0.8
Temperature rise induced by Joule heating (K)	0.05	0.04
Power consumption (W)	0.29	4.1

6.4 Discussion

In this chapter, a concept for improving the throughput of the cIDE-DEP system by introducing a novel concentric cIDE separator for continuous size-based fractionation of microparticles was proposed. The concentric cIDE separator was designed using a concentrically arranged interdigitated electrode configuration to produce the inhomogenous electric field. The induced negative DEP force acting on differently sized particles results in different motion trajectories and thereby dielectrophoretic displacements within the separator. The tunable sampling tube was installed along the central axis of the separation chamber to collect size-specific particle fractions depending on their radial positions, and thus enables size-based fractionation.

To assess the feasibility of fractionation with such a design, particle motion trajectories in the separation chamber were numerically analyzed using a simplified Langrangian particle tracking model that includes the effects of both the electric field and the flow field. Depending on the DEP force, which is proportional to particle size, different particles present distinct motion trajectories, and their radial positions in terms of dielectrophoretic displacement when passing through the separation chamber are apparently different. The differences in particles' radial displacements, which are primarily induced by negative DEP force in combination with hydrodynamic flow, provides the opportunity to discriminate among differently sized particles, so that continuous fractionation is possible.

A sensitive analysis of the impact of operating parameters on the dielectrophoretic motion of particles was performed in order to evaluate the potential quality of fractionation. It was found that the radial displacement of particles can apparently be increased, either by raising the voltage input or by reducing the system volume flow rate, or a combination of both. These

numerical predictions are intended as a theoretical foundation for optimal design of the concentric cIDE separator and experimental proof of the fractionation.

The concentric cIDE separator was compared with the cIDE separator developed in Chapter 5. Surprisingly, a 6 $mL \cdot min^{-1}$ suspension volume flow rate was achieved by the concentric cIDE separator with effective dielectrophoretic discriminating capability – much higher than a 0.6 $mL \cdot min^{-1}$ suspension volume flow that was achieved by the cIDE separator under same conditions. This enables continuous microparticle fractionation at a significantly improved throughput of the cIDE-DEP system.

7 Conclusion and outlook

7.1 Conclusion

Dielectrophoretic system scale-up is considered one of the most effective approaches for solving the low-throughput problem of DEP-based microparticle separation devices. In this thesis, a novel electrode configuration with interdigitatedly arranged cylindrical electrodes (cIDE) was suggested, as it offers greater potential to manipulate particles in enlarged DEP systems when compared to conventional electrode configurations. The simulation of electrode field gradient distribution, i.e., the DEP field, and hence particle motion indicates that, compared to orthogonal electrode and plate IDE, cIDE provides more homogeneously distributed field gradients on the electrode surface and more effective DEP force fields at identical particle-electrode distances, thus reducing the voltage required to achieve the same DEP effects. Simulations were verified experimentally by mearing the velocity of resin particle suspended at the subsurface of demineralized water in a DEP cell mounted by cIDEs. Good agreement allows simulation to be performed for reliable predictions of similar cIDE-DEP systems.

The structural parameters of the proposed cIDE, i.e., the aspect ratio, which is defined as the ratio between electrode diameter and the space between electrodes, was found to have an impact on the DEP force field. The smaller the aspect ratio, the lower the intensity of DEP force in the vicinity of electrodes, while the wider the DEP force field with respect to the channel height. A significant increase in the volume of the cIDE-DEP system and therefore in the possible throughput was numerically proved to be achievable by varying the aspect ratio of the electrodes at identical channel widths.

DEP channel scale-up requires high electric potentials in order to maintain the DEP force at the same level as those used in microsystems. The high voltages used in millimeter-scale DEP systems cause a significant electrothermal effect induced by Joule heating, which drives motion of the fluid medium and in turn influences the dielectrophoretic motion of particles. A model was developed to predict the influence of the electrothermal effect on particles by integrating electrothermal motion of the medium into the DEP motion of particles. Experimental proof of the model's feasibility was provided by measuring particle motions in a batch cIDE-DEP system assembled with different aspect ratio electrodes. Good agreement between experimental and model simulation allows numerical prediction of particle motion and quantification of the undesired electrothermal effect. Model calculations show that the height

of the DEP channel is crucial for proper separation and that the critical channel height was therefore defined as the maximum height where dielectrophoretic particle velocities are predominant. The design criteria for millimeter-scale cIDE-DEP systems was then suggested with respect to structure, channel geometries and system parameters, allowing maximum DEP velocities to be achieved with minimized electrothermal disturbance.

For particle motion in continuous dielectrophoretic field-flow systems, a separator with design tailored cIDE configuration is proposed for continuous size-based microparticle fractionation. The tailoring design of cIDEs was achieved by increasing spaces between the first three electrodes while maintain same spaces for the following electrodes. By such a design, both strong DEP force fields and broader DEP working areas can be provided, enabling sustainable and effective DEP particle levitation. Simulations based on single particle tracking were performed to evaluate 45, 25 and 11 μm particle trajectories within the proposed cIDE separator. The simulations of particle trajectory were then verified experimentally with good agreement. Particles of different size were levitated to different dynamic positions due to the negative DEP force which has a cubic dependency on the particle radius. The position differences during the transient ascend of the particles allows for a size-based fractionation of particles at the outlet. Fractionation resolution, which was introduced to quantify the performance of the cIDE separator, was numerically evaluated in relation to collector width, voltage input and the volumetric flow rate of the system. Fractionation resolution decreases with increasing collector width. At a specified collector width, a high resolution can be achieved by increasing voltage input or by reducing the volume flow rate. By trading off these parameters, a theoretical throughput of up to 47 $mL \cdot min^{-1}$ was estimated as being achievable for continuous fractionation of the specified 10 μm particle with an acceptable resolution.

To continue the concept of scaling up the cIDE-DEP separation system, a new dielectrophoretic separator is introduced that allows continuous fractionation of microparticles at even higher throughput. The concentric cIDE separator is designed to enhance the dielectrophoretic controllability while minimizing the gravitational disturbance of a particle's DEP motion by adjusting the electrode arrangement and the flow orientation. The dielectrophoretic motion of particles in the separation chamber was numerically predicted to evaluate the feasibility of fractionation. Different particle sizes show distinct motion trajectories, so discrepancies in radial position due to dielectrophoretic displacement provides the possibility of size-based fractionation. An order of magnitude increase in suspension volume flow was found to be feasible with the concentric cIDE separator in comparison with the cIDE separator under the same conditions. The dependence of dielectrophoretic displacement on

both voltage input and volume flow rate was numerically investigated. From tailoring design of operation parameters, it is expected that microparticles can be effectively fractionated with even smaller size fractions at the expected throughput. All these results are seen as an encouraging step forward to continuous dielectrophoretic particle separation on an industrial scale.

7.2 Outlook on future work

Dielectrophoresis is becoming a widely recognized tool for particle separation, advancing alongside conventional separation techniques such as centrifugation, membrane filtration, electrophoresis and others. However, application in microsystems with extremely low throughput makes it very difficult for dielectrophoretic particle separation to compete with traditional means of separation. This thesis mainly focuses on the development of large DEP separators meeting the need for high-throughput separation. Although great efforts have been made, some issues and challenges still need to be addressed.

Fluid convention induced by Joule heating in large DEP systems interferes with the dielectrophoretic motion of particles. This interference has been successfully described by a theoretical model that predicts electrothermal fluid motion in a specific case, namely in a batch IDE-DEP system. It can be expected that, in continuous systems with imposed fluid flow, the disturbances due to Joule heating are not that significant compared to those in batch separation systems. However, this side-effect should never be underestimated, especially in continuous separation systems where high voltages are applied and high-conductivity media are used. Instead, new theoretical models should be developed for predicting the impact of Joule heating in continuous IDE-DEP systems, and both simulations and experimental studies are required to improve our theoretical understanding of the phenomenon. On this basis, research should then focus on reducing Joule heating interference with particles in enlarged continuous DEP systems, in order to allow better dielectrophoretic manipulation of particles.

Energy efficiency is always a major concern in industrial processes. High voltages have to be applied in DEP systems to produce an electric field of sufficient intensity and hence a DEP force for effectively manipulating particles, which in turn causes high power consumption. The dilemma between separation efficacy and energy consumption becomes more incisive in scaled-up DEP systems, where increased energy input is required to obtain better separation at higher throughput. The objective of continuous separation of microparticles in large cIDE-DEP separators with high efficiency and low energy consumption can be possible either by optimizing the design of electrode configurations as described in this thesis, or by introducing

the concept of floating electrodes. The latter is thought to be more promising due to fewer electrodes being connected to the external signal sources, thus reducing energy input and facilitating the fabrication and operation of DEP devices. More simulation and experimental studies are expected to concentrate on the design and positioning of floating electrodes in DEP devices, and on evaluating the effectiveness of the resulting non-uniform electric field in manipulating particles and thus achieving continuous separation.

For the cIDE separator in Chapter 5, modeling and experimental validation was carried out to characterize the trajectories in the device. More experimental work is required to demonstrate the theoretical evaluation of device performance, i.e., how the defined fractionation resolution can be used as the parameter for assessing particle fractionation and its dependence on particle diameters, collector width, voltage input and flow rate. The concentric cIDE separator proposed in Chapter 6 allows further improvements in the throughput of cIDE-DEP systems. Both separator design and microparticle motion trajectories have been numerically analyzed. Experimental studies should be conducted in order to demonstrate the theoretical fractionation and throughput.

Bibliography

Ahn, K., Kerbage, C., Hunt, T.P., Westervelt, R., Link, D.R., Weitz, D., 2006. Dielectrophoretic manipulation of drops for high-speed microfluidic sorting devices. Applied Physics Letters, 88(2): 24104-24104.

Al-Jarro, A., Paul, J., Thomas, D., Crowe, J., Sawyer, N., Rose, F., Shakesheff, K., 2007. Direct calculation of Maxwell stress tensor for accurate trajectory prediction during DEP for 2D and 3D structures. Journal of Physics D: Applied Physics, 40(1): 71.

Arnold, W., Chapman, B., 2000. The Lev-vection particle concentrator: some operational characteristics, Electrical Insulation and Dielectric Phenomena, 2000 Annual Report Conference on. IEEE, pp. 752-755.

Arnold, W.M., 2001. Positioning and levitation media for the separation of biological cells. Industry Applications, IEEE Transactions on, 37(5): 1468-1475.

Auroux, P.-A., Iossifidis, D., Reyes, D.R., Manz, A., 2002. Micro total analysis systems. 2. Analytical standard operations and applications. Analytical chemistry, 74(12): 2637-2652.

Baune, M., Du, F., Thöming, J., 2008. Dielectrophoresis—bridging the scale in modeling and application. Vernetzte Wissenschaften. Logos Verlag Berlin GmbH, Berlin: 47-64.

Beebe, D.J., Mensing, G.A., Walker, G.M., 2002. Physics and applications of microfluidics in biology. Annual review of biomedical engineering, 4(1): 261-286.

Bettelheim, F., Brown, W., Campbell, M., Farrell, S., Torres, O., 2012. Introduction to general, organic and biochemistry. Cengage Learning.

Bhagat, A.A.S., Hou, H.W., Li, L.D., Lim, C.T., Han, J., 2011. Pinched flow coupled shear-modulated inertial microfluidics for high-throughput rare blood cell separation. Lab on a Chip, 11(11): 1870-1878.

Bisceglia, E., Cubizolles, M., Trainito, C.I., Berthier, J., Pudda, C., Français, O., Mallard, F., Le Pioufle, B., 2015. A generic and label free method based on dielectrophoresis for the continuous separation of microorganism from whole blood samples. Sensors and Actuators B: Chemical, 212: 335-343.

Boussinesq, J., 1903. Théorie analytique de la chaleur: mise en harmonie avec la thermodynamique et avec la théorie mécanique de la lumière, 2. Gauthier-Villars.

Cao, J., Cheng, P., Hong, F., 2008. A numerical analysis of forces imposed on particles in conventional dielectrophoresis in microchannels with interdigitated electrodes. Journal of Electrostatics, 66(11): 620-626.

Carlo, D.D., Edd, J.F., Irimia, D., Tompkins, R.G., Toner, M., 2008. Equilibrium separation and filtration

of particles using differential inertial focusing. Analytical chemistry, 80(6): 2204-2211.

Castellanos, A., Perez, A., 1998. Electrohydrodynamics. CISM courses and lectures No 380, International Centre for Mechanical Sciences. Springer–Verlag Wien New York.

Castellanos, A., Ramos, A., Gonzalez, A., Green, N.G., Morgan, H., 2003. Electrohydrodynamics and dielectrophoresis in microsystems: scaling laws. Journal of Physics D: Applied Physics, 36(20): 2584.

Čemažar, J., Douglas, T.A., Schmelz, E.M., Davalos, R.V., 2016. Enhanced contactless dielectrophoresis enrichment and isolation platform via cell-scale microstructures. Biomicrofluidics, 10(1): 014109.

Çetin, B., Kang, Y., Wu, Z., Li, D., 2009. Continuous particle separation by size via AC-dielectrophoresis using a lab-on-a-chip device with 3-D electrodes. Electrophoresis, 30(5): 766-772.

Çetin, B., Li, D., 2011. Dielectrophoresis in microfluidics technology. Electrophoresis, 32(18): 2410-2427.

Chen, D., Du, H., 2010. A microfluidic device for rapid concentration of particles in continuous flow by DC dielectrophoresis. Microfluidics and Nanofluidics, 9(2-3): 281-291.

Cheng, I.-F., Froude, V.E., Zhu, Y., Chang, H.-C., Chang, H.-C., 2009. A continuous high-throughput bioparticle sorter based on 3D traveling-wave dielectrophoresis. Lab on a Chip, 9(22): 3193-3201.

Choi, S., Park, J.-K., 2007. Continuous hydrophoretic separation and sizing of microparticles using slanted obstacles in a microchannel. Lab on a Chip, 7(7): 890-897.

Chuang, H.-S., Chung, T.-Y., Li, Y., 2014. Compact and tunable size-based dielectrophoretic flow fractionation. Journal of Micromechanics and Microengineering, 24(12): 125016.

Clip, R., Grace, J., Weber, M., 1978. Bubbles, Drops, and Particles.

Crane, J.S., Pohl, H.A., 1968. A study of living and dead yeast cells using dielectrophoresis. Journal of the Electrochemical Society, 115(6): 584-586.

Crews, N., Darabi, J., Voglewede, P., Guo, F., Bayoumi, A., 2007. An analysis of interdigitated electrode geometry for dielectrophoretic particle transport in micro-fluidics. Sensors and Actuators B: Chemical, 125(2): 672-679.

Crowe, C.T., Schwarzkopf, J.D., Sommerfeld, M., Tsuji, Y., 2011. Multiphase flows with droplets and particles. CRC press.

Cui, H.-H., Voldman, J., He, X.-F., Lim, K.-M., 2009. Separation of particles by pulsed dielectrophoresis. Lab on a Chip, 9(16): 2306-2312.

Cummings, E.B., Singh, A.K., 2003. Dielectrophoresis in microchips containing arrays of insulating posts: theoretical and experimental results. Analytical chemistry, 75(18): 4724-4731.

Das, D., Biswas, K., Das, S., 2014. A microfluidic device for continuous manipulation of biological cells

using dielectrophoresis. Medical engineering & physics, 36(6): 726-731.

Doh, I., Cho, Y.-H., 2005. A continuous cell separation chip using hydrodynamic dielectrophoresis (DEP) process. Sensors and Actuators A: Physical, 121(1): 59-65.

Drews, A., 2010. Membrane fouling in membrane bioreactors—characterisation, contradictions, cause and cures. Journal of Membrane Science, 363(1): 1-28.

Du, F., Baune, M., Kück, A., Thöming, J., 2008. Dielectrophoretic gold particle separation. Separation Science and Technology, 43(15): 3842-3855.

Du, F., Baune, M., Thöming, J., 2007. Insulator-based dielectrophoresis in viscous media—simulation of particle and droplet velocity. Journal of electrostatics, 65(7): 452-458.

Du, F., Ciaciuch, P., Bohlen, S., Wang, Y., Baune, M., Thöming, J., 2013. Intensification of cross-flow membrane filtration using dielectrophoresis with a novel electrode configuration. Journal of Membrane Science, 448: 256-261.

Du, F., Hawari, A., Baune, M., Thöming, J., 2009. Dielectrophoretically intensified cross-flow membrane filtration. Journal of Membrane Science, 336(1): 71-78.

Dukhin, S.S., Deriaguine, B.V., 1974. Surface and Colloid Science: Electrokinetic Phenomena: Translated from the Russian by A. Mistetsky and M. Zimmerman. Plenum Press.

Einstein, A., 1956. Investigations on the Theory of the Brownian Movement. Courier Corporation.

Ermolina, I., Morgan, H., 2005. The electrokinetic properties of latex particles: comparison of electrophoresis and dielectrophoresis. Journal of colloid and interface science, 285(1): 419-428.

Fatoyinbo, H.O., Kamchis, D., Whattingham, R., Ogin, S.L., Hughes, M.P., 2005. A high-throughput 3-D composite dielectrophoretic separator. Biomedical Engineering, IEEE Transactions on, 52(7): 1347-1349.

Fedotov, P.S., Vanifatova, N.G., Shkinev, V.M., Spivakov, B.Y., 2011. Fractionation and characterization of nano-and microparticles in liquid media. Analytical and bioanalytical chemistry, 400(6): 1787-1804.

Flagan, R.C., 1999. On differential mobility analyzer resolution. Aerosol Science & Technology, 30(6): 556-570.

Gadish, N., Voldman, J., 2006. High-throughput positive-dielectrophoretic bioparticle microconcentrator. Analytical chemistry, 78(22): 7870-7876.

Giddings, J.C., 1966. A new separation concept based on a coupling of concentration and flow nonuniformities. Separation Science, 1(1): 123-125.

Giddings, J.C., 1993. Field-flow fractionation: analysis of macromolecular, colloidal, and particulate materials. Science, 260(5113): 1456-1465.

Gimbert, L.J., Haygarth, P.M., Beckett, R., Worsfold, P.J., 2005. Comparison of centrifugation and

filtration techniques for the size fractionation of colloidal material in soil suspensions using sedimentation field-flow fractionation. Environmental science & technology, 39(6): 1731-1735.

Glynn, J., Belongia, B., Arnold, R., Ogden, K., Baygents, J., 1998. Capillary electrophoresis measurements of electrophoretic mobility for colloidal particles of biological interest. Applied and environmental microbiology, 64(7): 2572-2577.

Golan, S., Elata, D., Orenstein, M., Dinnar, U., 2006. Floating electrode dielectrophoresis. Electrophoresis, 27(24): 4919-4926.

Gossett, D.R., Weaver, W.M., Mach, A.J., Hur, S.C., Tse, H.T.K., Lee, W., Amini, H., Di Carlo, D., 2010. Label-free cell separation and sorting in microfluidic systems. Analytical and bioanalytical chemistry, 397(8): 3249-3267.

Green, N.G., Jones, T.B., 2006. Numerical determination of the effective moments of non-spherical particles. Journal of Physics D: Applied Physics, 40(1): 78.

Green, N.G., Ramos, A., Morgan, H., 2002. Numerical solution of the dielectrophoretic and travelling wave forces for interdigitated electrode arrays using the finite element method. Journal of Electrostatics, 56(2): 235-254.

Griffiths, D.J., College, R., 1999. Introduction to electrodynamics, 3. prentice Hall Upper Saddle River, NJ.

Guo, W., Ngo, H.-H., Li, J., 2012. A mini-review on membrane fouling. Bioresource technology, 122: 27-34.

Han, C., Sun, J., Liu, J., Cheng, H., Wang, Y., 2015. A pressure-driven capillary electrophoretic system with injection valve sampling. Analyst, 140(1): 162-173.

Han, K.-H., Han, S.-I., Frazier, A.B., 2009. Lateral displacement as a function of particle size using a piecewise curved planar interdigitated electrode array. Lab on a Chip, 9(20): 2958-2964.

Heida, T., 2012. Electric field-induced effects on neuronal cell biology accompanying dielectrophoretic trapping, 173. Springer Science & Business Media.

Henry, D., 1931. The cataphoresis of suspended particles. Part I. The equation of cataphoresis, Proceedings of the Royal Society of London A: Mathematical, Physical and Engineering Sciences. The Royal Society, pp. 106-129.

HeonáLee, K., BokáKim, S., SooáLee, K., JináSung, H., 2011. Enhancement by optical force of separation in pinched flow fractionation. Lab on a Chip, 11(2): 354-357.

Huang, Y., Ewalt, K.L., Tirado, M., Haigis, R., Forster, A., Ackley, D., Heller, M.J., O'Connel, J.P., Krihak, M., 2001. Electric manipulation of bioparticles and macromolecules on microfabricated electrodes. Analytical Chemistry, 73(7): 1549-1559.

Huang, Y., Wang, X.-B., Becker, F.F., Gascoyne, P., 1997. Introducing dielectrophoresis as a new force

field for field-flow fractionation. Biophysical journal, 73(2): 1118-1129.

Hughes, M.P., 2002. Strategies for dielectrophoretic separation in laboratory-on-a-chip systems. Electrophoresis, 23(16): 2569-2582.

Hunter, R.J., 2003. The significance of stagnant layer conduction in electrokinetics. Advances in colloid and interface science, 100: 153-167.

Jin, C., McFaul, S.M., Duffy, S.P., Deng, X., Tavassoli, P., Black, P.C., Ma, H., 2014. Technologies for label-free separation of circulating tumor cells: from historical foundations to recent developments. Lab on a Chip, 14(1): 32-44.

Jones, T., 1995. Electromechanics of particles. 1995. Cambridge, Cambridge.

Jones, T., Washizu, M., 1996. Multipolar dielectrophoretic and electrorotation theory. Journal of Electrostatics, 37(1): 121-134.

Jubery, T.Z., Srivastava, S.K., Dutta, P., 2014. Dielectrophoretic separation of bioparticles in microdevices: A review. Electrophoresis, 35(5): 691-713.

Kang, K.H., Kang, Y., Xuan, X., Li, D., 2006. Continuous separation of microparticles by size with Direct current-dielectrophoresis. Electrophoresis, 27(3): 694-702.

Kang, Y., Cetin, B., Wu, Z., Li, D., 2009. Continuous particle separation with localized AC-dielectrophoresis using embedded electrodes and an insulating hurdle. Electrochimica Acta, 54(6): 1715-1720.

Kang, Y., Li, D., 2009. Electrokinetic motion of particles and cells in microchannels. Microfluidics and nanofluidics, 6(4): 431-460.

Katasonova, O., Fedotov, P., 2009. Methods for continuous flow fractionation of microparticles: outlooks and fields of application. Journal of Analytical Chemistry, 64(3): 212-225.

Kersaudy-Kerhoas, M., Dhariwal, R., Desmulliez, M., 2008. Recent advances in microparticle continuous separation. Nanobiotechnology, IET, 2(1): 1-13.

Khashei, H., Latifi, H., Seresht, M.J., Ghasemi, A.H.B., 2015. Microparticles manipulation and enhancement of their separation in pinched flow fractionation by insulator-based dielectrophoresis. Electrophoresis.

Kim, U., Qian, J., Kenrick, S.A., Daugherty, P.S., Soh, H.T., 2008. Multitarget dielectrophoresis activated cell sorter. Analytical chemistry, 80(22): 8656-8661.

Kissa, E., 1999. Dispersions: characterization, testing, and measurement, 84. CRC Press.

Knoerzer, M., Szydzik, C., Tovar-Lopez, F.J., Tang, X., Mitchell, A., Khoshmanesh, K., 2016. Dynamic drag force based on iterative density mapping: A new numerical tool for three-dimensional analysis of particle trajectories in a dielectrophoretic system. Electrophoresis.

Kralj, J.G., Lis, M.T., Schmidt, M.A., Jensen, K.F., 2006. Continuous dielectrophoretic size-based

particle sorting. Analytical chemistry, 78(14): 5019-5025.

Kumar, A., Williams, S.J., Wereley, S.T., 2009. Experiments on opto-electrically generated microfluidic vortices. Microfluidics and Nanofluidics, 6(5): 637-646.

Kuntaegowdanahalli, S.S., Bhagat, A.A.S., Kumar, G., Papautsky, I., 2009. Inertial microfluidics for continuous particle separation in spiral microchannels. Lab on a Chip, 9(20): 2973-2980.

Leal, L.G., 2007. Advanced transport phenomena: fluid mechanics and convective transport processes. Cambridge University Press.

Lenshof, A., Laurell, T., 2010. Continuous separation of cells and particles in microfluidic systems. Chemical Society Reviews, 39(3): 1203-1217.

Leu, T.-S., Weng, C.-Y., 2009. Studies of particle levitation in a dielectrophoretic field-flow fraction–based microsorter. Journal of Micro/Nanolithography, MEMS, and MOEMS, 8(2): 021106-021106-5.

Lewpiriyawong, N., Yang, C., Lam, Y.C., 2010. Continuous sorting and separation of microparticles by size using AC dielectrophoresis in a PDMS microfluidic device with 3-D conducting PDMS composite electrodes. Electrophoresis, 31(15): 2622-2631.

Li, S., Qian, D., 2013. Multiscale simulations and mechanics of biological materials. John Wiley & Sons.

Li, X., Chin, E., Sun, H., Kurup, P., Gu, Z., 2010. Fabrication and integration of metal oxide nanowire sensors using dielectrophoretic assembly and improved post-assembly processing. Sensors and Actuators B: Chemical, 148(2): 404-412.

Li, Y., Dalton, C., Crabtree, H.J., Nilsson, G., Kaler, K.V., 2007. Continuous dielectrophoretic cell separation microfluidic device. Lab on a Chip, 7(2): 239-248.

Ling, S.H., Lam, Y.C., Chian, K.S., 2012. Continuous cell separation using dielectrophoresis through asymmetric and periodic microelectrode array. Analytical chemistry, 84(15): 6463-6470.

Lorrain, P., Corson, D.R., Lorrain, F., 2001. Fundamentals of electromagnetic phenomena, 1.

Lyklema, J., 2005. Fundamentals of interface and colloid science: soft colloids, 5. Academic press.

Lyklema, J., Minor, M., 1998. On surface conduction and its role in electrokinetics. Colloids and Surfaces A: Physicochemical and Engineering Aspects, 140(1): 33-41.

Markx, G.H., Pethig, R., 1995. Dielectrophoretic separation of cells: continuous separation. Biotechnology and bioengineering, 45(4): 337-343.

Markx, G.H., Pethig, R., Rousselet, J., 1997. The dielectrophoretic levitation of latex beads, with reference to field-flow fractionation. Journal of Physics D: Applied Physics, 30(17): 2470.

Markx, G.H., Talary, M.S., Pethig, R., 1994. Separation of viable and non-viable yeast using dielectrophoresis. Journal of Biotechnology, 32(1): 29-37.

Mason, B., Townsley, P., 1971. Dielectrophoretic separation of living cells. Canadian journal of

microbiology, 17(7): 879-888.

Mathew, B., Alazzam, A., Abutayeh, M., Gawanmeh, A., Khashan, S., 2015. Modeling the trajectory of microparticles subjected to dielectrophoresis in a microfluidic device for field flow fractionation. Chemical Engineering Science, 138: 266-280.

Mernier, G., Piacentini, N., Braschler, T., Demierre, N., Renaud, P., 2010. Continuous-flow electrical lysis device with integrated control by dielectrophoretic cell sorting. Lab on a Chip, 10(16): 2077-2082.

Messaud, F.A., Sanderson, R.D., Runyon, J.R., Otte, T., Pasch, H., Williams, S.K.R., 2009. An overview on field-flow fractionation techniques and their applications in the separation and characterization of polymers. Progress in Polymer Science, 34(4): 351-368.

Moon, H.-S., Kwon, K., Kim, S.-I., Han, H., Sohn, J., Lee, S., Jung, H.-I., 2011. Continuous separation of breast cancer cells from blood samples using multi-orifice flow fractionation (MOFF) and dielectrophoresis (DEP). Lab on a Chip, 11(6): 1118-1125.

Morgan, H., Green, N.G., 2003. AC electrokinetics: colloids and nanoparticles. Research Studies Press.

Morganti, E., Collini, C., Cunaccia, R., Gianfelice, A., Odorizzi, L., Adami, A., Lorenzelli, L., Jacchetti, E., Podesta, A., Lenardi, C., 2011. A dielectrophoresis-based microdevice coated with nanostructured TiO2 for separation of particles and cells. Microfluidics and Nanofluidics, 10(6): 1211-1221.

Moschallski, M., Hausmann, M., Posch, A., Paulus, A., Kunz, N., Duong, T.T., Angres, B., Fuchsberger, K., Steuer, H., Stoll, D., 2010. MicroPrep: Chip-based dielectrophoretic purification of mitochondria. Electrophoresis, 31(15): 2655-2663.

Müller, T., Gradl, G., Howitz, S., Shirley, S., Schnelle, T., Fuhr, G., 1999. A 3-D microelectrode system for handling and caging single cells and particles. Biosensors and Bioelectronics, 14(3): 247-256.

Neculae, A., Biris, C.G., Bunoiu, M., Lungu, M., 2012. Numerical analysis of nanoparticle behavior in a microfluidic channel under dielectrophoresis. Journal of Nanoparticle Research, 14(10): 1-12.

Nili, H., Sun, T., Green, N., 2011. Higher order dielectrophoretic force characterisation of non-spherical particles, Journal of Physics: Conference Series. IOP Publishing, pp. 012061.

O'Konski, C.T., 1960. Electric properties of macromolecules. V. Theory of ionic polarization in polyelectrolytes. The Journal of Physical Chemistry, 64(5): 605-619.

Ohshima, H., 2001. Approximate analytic expression for the electrophoretic mobility of a spherical colloidal particle. Journal of colloid and interface science, 239(2): 587-590.

Pamme, N., 2007. Continuous flow separations in microfluidic devices. Lab on a Chip, 7(12): 1644-1659.

Pamme, N., Wilhelm, C., 2006. Continuous sorting of magnetic cells via on-chip free-flow magnetophoresis. Lab on a Chip, 6(8): 974-980.

Park, B.Y., Madou, M., 2005. 3-D electrode designs for flow-through dielectrophoretic systems.

Park, J.-S., Jung, H.-I., 2009. Multiorifice flow fractionation: Continuous size-based separation of microspheres using a series of contraction/expansion microchannels. Analytical chemistry, 81(20): 8280-8288.

Pesch, G.R., Du, F., Schwientek, U., Gehrmeyer, C., Maurer, A., Thöming, J., Baune, M., 2014. Recovery of submicron particles using high-throughput dielectrophoretically switchable filtration. Separation and Purification Technology, 132: 728-735.

Pesch, G.R., Kiewidt, L., Du, F., Baune, M., Thöming, J., 2015. Electrodeless Dielectrophoresis: Impact of geometry and material on obstacle polarization. Electrophoresis.

Pethig, R., 1996. Dielectrophoresis: using inhomogeneous AC electrical fields to separate and manipulate cells. Critical Reviews in Biotechnology, 16(4): 331-348.

Pethig, R., 2010. Review article—dielectrophoresis: status of the theory, technology, and applications. Biomicrofluidics, 4(2): 022811.

Pethig, R., 2013. Dielectrophoresis: An assessment of its potential to aid the research and practice of drug discovery and delivery. Advanced drug delivery reviews, 65(11): 1589-1599.

Pethig, R., Markx, G.H., 1997. Applications of dielectrophoresis in biotechnology. Trends in biotechnology, 15(10): 426-432.

Pohl, H.A., 1951. The motion and precipitation of suspensoids in divergent electric fields. Journal of Applied Physics, 22(7): 869-871.

Pohl, H.A., 1958. Some effects of nonuniform fields on dielectrics. Journal of Applied Physics, 29(8): 1182-1188.

Pohl, H.A., 1978. Dielectrophoresis: the behavior of neutral matter in nonuniform electric fields, 80. Cambridge university press Cambridge.

Pohl, H.A., Plymale, C.E., 1960. Continuous separations of suspensions by nonuniform electric fields in liquid dielectrics. Journal of The Electrochemical Society, 107(5): 390-396.

Pommer, M.S., Zhang, Y., Keerthi, N., Chen, D., Thomson, J.A., Meinhart, C.D., Soh, H.T., 2008. Dielectrophoretic separation of platelets from diluted whole blood in microfluidic channels. Electrophoresis, 29(6): 1213-1218.

Probstein, R.F., 2005. Physicochemical hydrodynamics: an introduction. John Wiley & Sons.

Qian, C., Huang, H., Chen, L., Li, X., Ge, Z., Chen, T., Yang, Z., Sun, L., 2014. Dielectrophoresis for bioparticle manipulation. International journal of molecular sciences, 15(10): 18281-18309.

Radko, S.P., Chrambach, A., 1999. Capillary electrophoresis of subcellular-sized particles. Journal of

Chromatography B: Biomedical Sciences and Applications, 722(1): 1-10.

Radko, S.P., Chrambach, A., 2002. Separation and characterization of sub-μm-and μm-sized particles by capillary zone electrophoresis. Electrophoresis, 23(13): 1957-1972.

Ramos, A., Morgan, H., Green, N.G., Castellanos, A., 1998. Ac electrokinetics: a review of forces in microelectrode structures. Journal of Physics D: Applied Physics, 31(18): 2338.

Ratier, C., Hoyos, M., 2010. Acoustic programming in step-split-flow lateral-transport thin fractionation. Analytical chemistry, 82(4): 1318-1325.

Reyes, D.R., Iossifidis, D., Auroux, P.-A., Manz, A., 2002. Micro total analysis systems. 1. Introduction, theory, and technology. Analytical chemistry, 74(12): 2623-2636.

Sano, N., Matsukura, B., Ikeyama, Y., Tamon, H., 2012. Dielectrophoretic particle separator using mesh stacked electrodes and simplified model for multistage separation. Chemical Engineering Science, 84: 345-350.

Seminario, L., Rozas, R., Bórquez, R., Toledo, P.G., 2002. Pore blocking and permeability reduction in cross-flow microfiltration. Journal of membrane Science, 209(1): 121-142.

Shafiee, H., Caldwell, J.L., Sano, M.B., Davalos, R.V., 2009. Contactless dielectrophoresis: a new technique for cell manipulation. Biomedical microdevices, 11(5): 997-1006.

Srivastava, S.K., Baylon-Cardiel, J.L., Lapizco-Encinas, B.H., Minerick, A.R., 2011. A continuous DC-insulator dielectrophoretic sorter of microparticles. Journal of Chromatography A, 1218(13): 1780-1789.

Takagi, J., Yamada, M., Yasuda, M., Seki, M., 2005. Continuous particle separation in a microchannel having asymmetrically arranged multiple branches. Lab on a Chip, 5(7): 778-784.

Thoeming, J., Du, F., Baune, M., 2006. Dielectrophoretic separation of oil-water-solid dispersions-selectivity and particle velocity. Fresenius Environmental Bulletin, 15(7): 687-691.

Tsukahara, S., Yamanaka, K., Watarai, H., 2001. Flow fractionation of microparticles under a dielectrophoretic field in a quadrupole electrode capillary. Analytical chemistry, 73(23): 5661-5668.

Vahey, M.D., Voldman, J., 2008. An equilibrium method for continuous-flow cell sorting using dielectrophoresis. Analytical chemistry, 80(9): 3135-3143.

Visser, D., Houkema, M., Siccama, N., Komen, E., 2012. Validation of a FLUENT CFD model for hydrogen distribution in a containment. Nuclear Engineering and Design, 245: 161-171.

Voldman, J., 2006. Electrical forces for microscale cell manipulation. Annu. Rev. Biomed. Eng., 8: 425-454.

Wang, X.-B., Vykoukal, J., Becker, F.F., Gascoyne, P.R., 1998. Separation of polystyrene microbeads using dielectrophoretic/gravitational field-flow-fractionation. Biophysical Journal, 74(5): 2689-

2701.

Wang, X., Wang, X.-B., Becker, F., Gascoyne, P.R., 1996. A theoretical method of electrical field analysis for dielectrophoretic electrode arrays using Green's theorem. Journal of Physics D: Applied Physics, 29(6): 1649.

Wang, X., Wang, X.-B., Gascoyne, P.R., 1997. General expressions for dielectrophoretic force and electrorotational torque derived using the Maxwell stress tensor method. Journal of electrostatics, 39(4): 277-295.

Wang, Y., Du, F., Baune, M., Thöming, J., 2014. Dielectrophoresis in aqueous suspension: impact of electrode configuration. Microfluidics and nanofluidics, 17(3): 499-507.

Wang, Y., Du, F., Baune, M., Thöming, J., 2015. Predicting and eliminating Joule heating constraints in large dielectrophoretic IDE separators. Chemical Engineering Science, 137: 235-242.

Wang, Y., Du, F., Pesch, G.R., Köser, J., Baune, M., Thöming, J., 2016. Micropaticle trajectories in a high-throughput channel for contact-free fractionation by dielectrophoresis. Chemical Engineering Science, 153: 34-44.

Weiss, B., Hilber, W., Gittler, P., Jakoby, B., 2009. Particle separation in alternating-current electro-osmotic micropumps using field-flow fractionation. Microfluidics and nanofluidics, 7(2): 191-203.

Wood, N.R., Wolsiefer, A.I., Cohn, R.W., Williams, S.J., 2013. Dielectrophoretic trapping of nanoparticles with an electrokinetic nanoprobe. Electrophoresis, 34(13): 1922-1930.

Xie, Y., Zheng, D., Li, Q., Chen, Y., Lei, H., Pu, L.L., 2010. The effect of centrifugation on viability of fat grafts: an evaluation with the glucose transport test. Journal of Plastic, Reconstructive & Aesthetic Surgery, 63(3): 482-487.

Xu, R., 2001. Particle characterization: light scattering methods, 13. Springer Science & Business Media.

Yamada, M., Nakashima, M., Seki, M., 2004. Pinched flow fractionation: continuous size separation of particles utilizing a laminar flow profile in a pinched microchannel. Analytical chemistry, 76(18): 5465-5471.

Yan, S., Zhang, J., Li, M., Alici, G., Du, H., Sluyter, R., Li, W., 2014. On-chip high-throughput manipulation of particles in a dielectrophoresis-active hydrophoretic focuser. Scientific reports, 4.

Yang, J., Huang, Y., Wang, X.-B., Becker, F.F., Gascoyne, P.R., 2000. Differential analysis of human leukocytes by dielectrophoretic field-flow-fractionation. Biophysical Journal, 78(5): 2680-2689.

Zellner, P., Agah, M., 2012. Silicon insulator-based dielectrophoresis devices for minimized heating effects. Electrophoresis, 33(16): 2498-2507.

Zhang, J., Yan, S., Sluyter, R., Li, W., Alici, G., Nguyen, N.-T., 2014. Inertial particle separation by differential equilibrium positions in a symmetrical serpentine micro-channel. Scientific reports,

4.

Appendix A

The appendix A contains all experimental data utilized in this thesis.

Table A.1: Experimental obtained velocities of resin particle suspended in the subsurface of the demineralized water in a cIDE-DEP test channel with different aspect ratio electrode arrangement (*d:L*) as **(a)** *d:L*= 2:1, **(b)** *d:L*= 1:1, **(c)** *d:L*= 1:2 and **(d)** *d:L*= 1:4, respectively. Ten trials of particle velocity were recorded (from #1 to #10) at each height. Treated experimental data can be found in Figure 4.5.

(a) *d:L* = 2:1

Height *h* (mm)		2	2.5	3	5	7
Velocity u_x (µm·s^{-1})	#1	969.449	384.456	164.339	64.339	82.730
	#2	1574.948	657.356	739.525	93.513	90.280
	#3	856.465	1535.053	328.678	219.256	48.191
	#4	977.095	411.572	410.847	62.862	65.461
	#5	2183.128	579.354	246.508	165.461	59.658
	#6	3218.880	826.845	657.356	96.633	41.365
	#7	2038.362	532.681	204.678	134.863	63.006
	#8	1079.563	877.362	397.391	78.735	75.276
	#9	921.231	1302.743	242.971	87.763	43.437
	#10	2504.991	361.538	682.232	168.633	78.964

(b) *d:L* = 1:1

Height *h* (mm)		2	2.5	3	5	7
Velocity u_x (µm·s^{-1})	#1	1017.345	821.695	703.864	289.556	82.955
	#2	1626.467	410.847	589.241	297.529	124.096
	#3	1228.378	1807.729	321.034	263.414	165.461
	#4	1661.775	1232.542	338.678	110.684	206.826
	#5	1821.695	1067.587	575.186	248.191	321.695
	#6	1330.664	2300.746	692.069	267.886	206.826
	#7	2867.726	1643.390	648.967	236.581	106.514
	#8	7669.984	1356.419	421.336	145.661	91.647

	#9	1317.277	1653.768	711.902	297.562	140.572
	#10	1889.898	1023.994	387.367	255.397	265.883

(c) *d:L* = 1:2

Height *h* (mm)		2	2.5	3	5	7
Velocity u_x (μm·s^{-1})	#1	3131.593	1178.025	1786.351	498.079	82.169
	#2	1310.127	2779.977	1337.622	308.758	379.113
	#3	3327.244	2755.064	2156.851	835.817	494.511
	#4	1868.945	3647.324	1188.568	715.460	627.304
	#5	2522.050	1595.454	3238.145	413.652	413.652
	#6	2957.179	2076.870	1285.881	724.076	579.113
	#7	6763.815	1214.917	1317.232	803.337	243.710
	#8	4784.936	2582.024	1396.555	487.871	396.382
	#9	4093.384	2737.974	1459.635	704.596	243.485
	#10	2577.483	1696.196	2418.284	313.375	558.023

(d) *d:L* = 1:4

Height *h* (mm)		2	2.5	3	5	7
Velocity u_x (μm·s^{-1})	#1	4946.573	2107.515	2978.990	1653.766	479.099
	#2	3811.814	2770.088	1038.371	1012.851	631.843
	#3	2192.596	3793.492	2215.408	991.563	503.229
	#4	4509.119	3096.278	1199.637	824.447	496.382
	#5	4242.598	3931.436	2322.136	415.960	413.652
	#6	2835.089	2702.864	1438.371	1411.233	430.921
	#7	4711.931	3865.168	1099.637	330.922	544.573
	#8	3359.416	2391.531	2875.408	1103.766	641.843
	#9	3880.073	3173.808	1722.470	1391.563	531.755
	#10	4920.745	3557.724	2441.163	714.411	421.454

Table A.2: Experimental time dependent **(a)** 45 µm, **(b)** 25 µm and **(c)** 11 µm PS particle trajectory positions (*x, h*) at entrance zone of the DEP separation channel as indicated in Figure 5.4. Trajectories of ten individual particles of each particle size were recorded (from #1 to #10). The calculated particle mean positions and position bars at each time step is shown in Figure 5.6. Units of values are as follows: time *t* in (s); position *x* and *h* in (mm).

(a) 45 µm

t	Position	#1	#2	#3	#4	#5	#6	#7	#8	#9	#10
0	*x*	0.421	0.451	0.395	0.472	0.480	0.487	0.475	0.411	0.434	0.484
	h	1.322	1.278	1.388	1.414	1.300	1.306	1.312	1.388	1.344	1.296
0.5	*x*	0.542	0.539	0.634	0.514	0.678	0.658	0.569	0.627	0.656	0.526
	h	1.379	1.321	1.405	1.429	1.463	1.354	1.363	1.349	1.436	1.421
1	*x*	0.718	0.700	0.827	0.755	0.877	0.811	0.724	0.866	0.835	0.735
	h	1.529	1.588	1.563	1.558	1.555	1.511	1.511	1.464	1.514	1.518
1.5	*x*	1.053	0.981	1.060	1.111	0.964	0.903	0.957	0.980	0.983	1.114
	h	1.686	1.763	1.692	1.732	1.873	1.799	1.615	1.774	1.848	1.899
2	*x*	1.507	1.582	1.358	1.581	1.595	1.606	1.490	1.756	1.552	1.572
	h	2.163	2.021	2.023	1.939	2.036	1.904	2.123	2.086	2.090	2.040
2.5	*x*	1.872	1.862	1.781	2.052	1.869	1.987	1.870	1.852	1.884	2.014
	h	2.336	2.204	2.279	2.276	2.203	2.323	2.321	2.328	2.447	2.408
3	*x*	2.493	2.347	2.325	2.374	2.522	2.401	2.267	2.365	2.478	2.323
	h	2.584	2.776	2.676	2.578	2.569	2.766	2.588	2.654	2.690	2.608
3.5	*x*	2.731	2.742	2.750	2.748	2.613	2.888	2.811	2.657	2.911	2.935
	h	2.789	2.784	2.926	3.061	2.941	3.030	2.958	3.093	3.023	3.080
4	*x*	3.283	3.197	3.271	3.230	3.232	3.379	3.120	3.236	3.336	3.255
	h	3.122	3.240	3.185	3.189	3.051	3.109	3.102	3.301	3.166	3.229

(b) 25 µm

t	Position	#1	#2	#3	#4	#5	#6	#7	#8	#9	#10
0	*x*	0.465	0.318	0.216	0.300	0.347	0.367	0.469	0.411	0.341	0.312
	h	1.429	1.505	1.399	1.277	1.451	1.472	1.411	1.438	1.483	1.515
	x	0.679	0.701	0.765	0.895	0.873	0.655	0.758	0.676	0.788	0.822

0.5	*h*	1.449	1.430	1.414	1.520	1.566	1.536	1.494	1.530	1.418	1.507
1	*x*	0.998	1.277	1.061	1.246	1.297	1.211	1.047	1.053	1.475	1.326
	h	1.642	1.697	1.562	1.615	1.599	1.578	1.590	1.690	1.676	1.612
1.5	*x*	1.712	1.677	1.792	1.673	1.484	1.786	1.646	1.773	1.732	1.617
	h	1.896	1.782	1.879	1.746	1.701	1.794	1.748	1.785	1.757	1.831
2	*x*	2.368	2.113	2.317	2.441	1.995	2.027	2.252	2.330	2.214	2.120
	h	1.958	1.924	2.094	2.061	1.901	2.023	2.084	1.903	2.085	2.024
2.5	*x*	2.841	2.704	2.643	2.639	2.755	2.899	2.838	2.800	2.519	2.536
	h	2.123	2.284	2.287	2.226	2.321	2.178	2.342	2.163	2.330	2.259
3	*x*	3.113	3.257	2.954	3.034	3.015	3.242	3.117	3.350	3.377	3.159
	h	2.434	2.418	2.480	2.501	2.424	2.472	2.546	2.461	2.363	2.524

(c) 11 μm

t	Position	#1	#2	#3	#4	#5	#6	#7	#8	#9	#10
0	*x*	0.306	0.357	0.459	0.504	0.477	0.516	0.542	0.423	0.522	0.399
	h	1.418	1.520	1.385	1.414	1.474	1.388	1.399	1.402	1.439	1.371
0.5	*x*	1.094	0.875	0.847	0.922	0.945	0.902	0.909	1.017	0.906	0.859
	h	1.470	1.633	1.543	1.426	1.435	1.394	1.439	1.390	1.520	1.450
1	*x*	1.439	1.388	1.358	1.528	1.326	1.369	1.419	1.399	1.350	1.435
	h	1.501	1.700	1.496	1.526	1.568	1.595	1.558	1.454	1.588	1.571
1.5	*x*	1.902	2.030	1.971	1.918	2.009	1.986	1.978	2.010	1.935	1.959
	h	1.536	1.559	1.700	1.579	1.712	1.666	1.677	1.533	1.669	1.675
2	*x*	2.547	2.521	2.510	2.524	2.359	2.339	2.465	2.389	2.425	2.482
	h	1.576	1.709	1.796	1.808	1.621	1.725	1.773	1.687	1.739	1.724
2.5	*x*	3.146	3.191	3.089	3.203	3.253	3.087	2.971	2.851	3.082	3.031
	h	1.903	1.724	1.754	1.847	1.835	1.957	1.856	1.747	1.734	1.876

Table A.3: Experimentally measured 11 μm particle velocities at x = 0 and different height h (ranging from 1 to 3 mm). Velocities of 27 individual particle data are recorded as shown in Figure 5.5.

h (mm)	u_p (mm·s^{-1})	h (mm)	u_p (mm·s^{-1})	h (mm)	u_p (mm·s^{-1})
2.0873	1.5619	2.1962	1.5434	1.5119	1.0838
1.9665	1.5253	2.3182	1.5682	1.3289	0.8318
2.2372	1.3966	1.7741	1.5089	2.3798	1.5620
1.9041	1.4954	2.0573	1.7176	2.0909	1.6178
2.5782	1.0964	1.7389	1.4391	2.3346	1.3606
1.5465	1.2592	1.7129	1.5604	2.4508	1.3333
1.6565	1.2918	1.7432	1.4708	2.5055	1.1685
2.6759	0.7888	1.3287	0.9426	1.6260	1.3770
1.9463	1.6899	1.4560	1.1840	2.0037	1.6556

Appendix B

The appendix B (CD Appendix) composes of a list of *OpenFOAM* relevant files utilized in this thesis, which includes:

1. Source code of the modified *OpenFOAM* solvers used for electric field and flow field ("*simpleMhdFoam"*) as well as particle trajectory ("*simpleMhdParcelFoam"*) calculations.
2. *OpenFOAM* cases including the test IDE-DEP channel with four different aspect ratio (*d:L*) electrodes (2:1, 1:1, 1:2 and 1:4) presented in Chapter 4, the cIDE separator presented in Chapter 5 and the concentric cIDE separator presented in Chapter 6, respectively.

In addition, a digital version of the PhD thesis has been included in the Appendix B.